

Alma Mater Studiorum - Università di Bologna

DOTTORATO DI RICERCA IN  
MECCANICA E SCIENZE AVANZATE DELL'INGEGNERIA

Ciclo 34

**Settore Concorsuale:** 09/A2 - MECCANICA APPLICATA ALLE MACCHINE

**Settore Scientifico Disciplinare:** ING-IND/13 - MECCANICA APPLICATA ALLE MACCHINE

MANUFACTURING AND EXPERIMENTAL CHARACTERIZATION OF ELECTRO  
ADHESIVE DEVICES

**Presentata da:** Nicolò Berdozzi

**Coordinatore Dottorato**

Marco Carricato

**Supervisore**

Rocco Vertechy

**Esame finale anno 2022**



# Abstract

Electro Adhesive Devices (EADs) are innovative actuators deployable for many applications, such as robotic grippers, locomotion systems for climbing and crawling robots, haptic devices, and gadgets for space applications. The most relevant advantageous features of EADs are the low energy consumptions and the lightweight and compact embodiment. Moreover, the EAD applicability extends to different environmental conditions like air, vacuum, and fluids on various adhering materials, like electrical conductors, insulators, and porous media.

An EAD always includes an electrode couple and one or more dielectric layers, which host and insulate the electrodes. The working principle is based on the electrostatic attraction that takes place between the device and the object once the electrodes are connected to a voltage source, propagating an electric field. Due to the high dependency of the phenomenon on a huge number of physical variables, an analytical approach for estimating EAD performance is always complex. Therefore, an experimental approach leading to the definition of empirical models seems to be the most effective way for the evaluation of the performances and to address the design and fabrication process of EADs.

This thesis proposes the Drop on Demand (DoD) Inkjet printing as the manufacturing method for the electrodes. By jetting a silver nanoparticle dispersed ink, it was possible to pattern the electrode geometry through a digitally controlled, maskless, contact-free process, leading to high resolution, flexible, and fast produced patches. A statistical systematic methodology based on Design of Experiment and ANOVA validates DoD Inkjet for the specific application by correlating the printing parameters to the geometry quality.

An experimental characterization is carried out on EAD of two different types, one having PEEK and another having Polyimide (PI) thin films as the adhering surface, which also act as the electrode printing substrate. For PI-based EADs, an explanatory gripper prototype was developed. The characterization process assesses the Electro Adhesive Shear Stress (ESS) performance of such devices on different adhering materials, along with their consumptions and time responses during the gripping tests.

Due to its high ESS results, PI-based EADs have been subjected to a manufacturing optimization process aiming to further increase adhesive force performances and dielectric strength.



# Summary

<b>Chapter 1. Introduction .....</b>	<b>1</b>
1.1 Electro-Adhesion (EA) applications .....	1
1.2 Motivation.....	2
<b>Chapter 2. Introduction on Electro-Adhesive Devices (EADs) .....</b>	<b>5</b>
2.1 General working principle of EADs .....	5
2.2 EAD composition and manufacturing .....	11
2.3 ESS performances of EADs.....	15
2.4 EAD applications .....	16
<b>Chapter 3. DoD inkjet printing for printed electronics .....</b>	<b>22</b>
3.1 Introduction.....	22
3.2 Droplet formation for DoD Piezo inkjet printers .....	27
3.3 Machine Description .....	35
3.4 Droplet formation examples with Microfab Jetlab® 4xl.....	41
3.5 Droplet deposition examples with Microfab Jetlab® 4xl .....	44
<b>Chapter 4. Assessing the relationships between interdigital geometry quality and inkjet printing parameters .....</b>	<b>53</b>
4.1 Introduction.....	53
4.2 Geometry design and manufacturing .....	55
4.3 Experimental procedure .....	56
4.4 Measurements and analysis.....	58
4.5 Results and discussions.....	62
4.6 Conclusions.....	66
<b>Chapter 5. PEEK based EADs: manufacturing and characterization .....</b>	<b>69</b>
5.1 Introduction.....	69

5.2	EAD specimen preparation .....	70
5.3	Testing set-up and procedure .....	72
5.4	Experimental results.....	74
5.5	Conclusions.....	77
<b>Chapter 6. PI based EADs: manufacturing, characterization, and application .....</b>		<b>79</b>
6.1	Introduction.....	79
6.2	Design and Fabrication .....	80
6.3	Experimental setup and test procedure .....	83
6.4	Results.....	85
6.5	Gripper Application .....	88
6.6	Conclusions.....	90
<b>Chapter 7. PI based EADs: Manufacturing optimization and performance improvement .....</b>		<b>93</b>
7.1	Introduction.....	93
7.2	Design and manufacturing .....	95
7.3	EAD testing.....	100
7.4	Experimental results and discussions.....	105
7.5	Conclusions.....	112
<b>Chapter 8. Conclusions.....</b>		<b>115</b>

# List of figures

Figure 1 - Schematic of one possible arrangement of an EAD adhering to an object.....	8
Figure 2 - Electrostatic force generation in the case of: (a) conductive object, and (b) dielectric object. ....	9
Figure 3 - Force equilibrium schematic of an EAD adhering to an object.....	10
Figure 4 – EAD configurations: (a) Spaced coplanar electrodes (denoted in black color) attached to a dielectric substrate (denoted in a gray color). (b) Spaced coplanar electrodes embedded in a dielectric. (c) Spaced coplanar electrodes embedded in two dielectrics (one denoted in gray and one denoted in orange). ....	12
Figure 5 – (a) One-sided spaced coplanar electrodes, (b) (c) (d) double-sided spaced electrodes.....	12
Figure 6 - EAD electrodes geometry patterns: (a) concentric, (b) spiral, (c), two-electrode, (d) comb-shape.....	13
Figure 8 - Workflow of an additive manufacturing process.....	13
Figure 9 - Workflow of a subtractive manufacturing process.....	14
Figure 10 - Workflow of an additive-subtractive manufacturing process.....	14
Figure 11 - Schematic of two possible setup configurations for ESS measurement: (a) the EAD is pulled while the object is fixed, (b) the EAD is kept fixed while the object is pulled away from it .....	15
Figure 12 - EA grippers from the literature: Rigid EA grippers (a) [4] (b) [48] (c) and (d) [45], Flexible EA grippers (e) [4] (f) [44] (g) [20] (h) [49], Stretchable EA grippers (i) [8] (j) [43] (k) [11].....	18
Figure 13 - EA haptic devices: (a) capacitive touchscreen [50], (b) eShiver EA artificial finger [51], (c) EA tactile display [52], (d) EA 2.5D tactile shape display [53].....	19
Figure 14 - EA crawling and climbing robots: (a) double tracks robot, (b) 1-D legged robot, (c) 2-D legged robot .....	19
Figure 15 - EAD for space applications: (a) and (b) EA docking systems [39], [57], (c) EA pad for orbital debris retrieving [58], (d) EA climbing robots used in NASA zero gravity airplane [59], (e) EAD for material handling in space applications [59].....	21
Figure 16 - CIJ (left) and DoD (right) schematization .....	23
Figure 17 - Gravity compensation by the Backpressure of the printing channel .....	23

Figure 18 - Schematic of a Drop on Demand printing system .....	24
Figure 19 - Inkjet printed (a) Electro-Adhesive device, (b) Piezoelectric cantilever, (c) Infrared sensor.....	25
Figure 20– Water drops on the surfaces of non-porous HA pellets before (A) and after (B) 5 minutes of Plasma treatment .....	26
Figure 21-Schematic representation of contact angle between a deposited droplet and a substrate.....	26
Figure 22- Wetting quality depending on contact angle value.....	27
Figure 23 - Schematic of nozzle tip jetting a fluid having Z lower than lower bound: no droplet is formed .....	29
Figure 24- Schematic of nozzle tip jetting a fluid having Z over the upper bound, generating satellites droplet.....	29
Figure 25 - Different waveform for driving voltage in DoD inkjet printing.....	31
Figure 26 - Wave phases in the single pulse and bipolar case .....	31
Figure 27 - Waveform design parameters for a bipolar wave .....	32
Figure 28 - Drop speed and volume relation with pulse width and pulse duration for single pulse waveform, while printing Butyl Carbitol at 2kHz with rise time of 7 $\mu$ s and fall time of 12.5 $\mu$ s.....	33
Figure 29 - Time sequence of droplet formation in response to one pulse ( $V_d = 29$ V).....	34
Figure 30- Jetting process of printhead divided in 10 $\mu$ s time slice, with $V_d = 25$ V and jetting frequency $f = 33$ kHz. The startup stage contains the 1st and 2nd pulses, and the process becomes repeatable from 3rd pulse on.....	34
Figure 31 - Microfab Jetlab® 4xl layout system.....	35
Figure 32 - Schematic of Microfab Jetlab® 4xl with main components.....	35
Figure 33 - Microfab Jetlab® 4xl moving platen (PL-HV-4XL), equipped with a vacuum bed and heating system .....	36
Figure 34 - Microfab Jetlab® 4xl printhead (PH-46-SM4-AT-ST2-H), hosting four printing channels and the jetting device heating system.....	37
Figure 35 - Jetlab® 4 xl pressure control panel for jetting channel n°2.....	38
Figure 36- Jetlab® 4 xl control panel of the heating system.....	38
Figure 37- Schematic of drop observation camera layout.....	39
Figure 38- Droplet observation frames delayed by 10 $\mu$ s while printing Isopropanol (IPA) with a 40 $\mu$ m nozzle using a W-shape waveform .....	40



Figure 39- Top-view of a conductive ink (Anapro DGP 40LT-15C) printing (black) onto polyimide substrate (Caplinq PIT1N/210) .....	40
Figure 40- Proper droplet formation of Isopropyl alcohol with single pulse waveform at 250 Hz .....	41
Figure 41 - Tail occurrence during droplet formation of Isopropyl alcohol with single pulse waveform at 250 Hz .....	42
Figure 42 - Satellites droplet during droplet formation of Isopropyl alcohol with single pulse waveform at 250 Hz .....	42
Figure 43 - Generation of smaller droplet of Isopropyl alcohol with W-shape waveform at 250 Hz .....	43
Figure 44 - Anapro DGP-40LT-15C on Caplinq Polyimide: (a) distinct droplet spaced by 0.3 mm and (b) part of an interdigitated geometry with droplet spaced by 0.17 mm along x and 0.2 mm along y directions .....	45
Figure 45 - Anapro DGP-40LT-15C on PEEK film: (a) distinct droplets spaced by 0.3 mm, (b) parallel arrays two droplet rows thick with 0.2 mm of spacing along x and y directions between droplets, (c) part of a 1mm by 1mm filled square with droplet spaced by 0.16 mm along x and 0.15 mm along y .....	45
Figure 46 - Anapro DGP-40LT-15C on Mylar film: (a) distinct droplets spaced by 0.3 mm, (b) array four droplet rows thick with droplet spaced by 0.17 mm along x and 0.18 mm along y, (c) parallel arrays two droplet rows thick with droplet spaced by 0.17 mm along x and y directions .....	46
Figure 47 - Anapro DGP-40LT-15C on PET film: (a) distinct droplets spaced by 0.3 mm, (b) array two droplet rows thick with droplet spaced by 0.09 mm along x and 0.11 mm along y, (c) part of a 1mm by 1mm filled square with droplet spaced by 0.17 mm along x and y directions .....	46
Figure 48 - Anapro DGP-40LT-15C on PVDF-MDO film: (a) distinct droplets spaced by 0.3 mm, (b) array two droplet rows thick with droplets spaced by 0.15 mm along x and y directions, (c) part of a 1mm by 1mm filled square with droplet spaced 0.15 mm along x and y directions .....	47
Figure 49 - Anapro DGP-40LT-15C on PEN film: (a) distinct droplets spaced by 0.3 mm, (b) array two droplet rows thick with droplets spaced by 0.19 mm along x and 0.18 mm along y, (c) parallel arrays two droplet rows thick with 0.18 mm of spacing between droplets along x and y directions, (d) part of a 1mm by 1mm filled square with droplets spaced by 0.16 mm along x and y directions .....	48

Figure 50 - Genes Ink Smart Ink CS01130 on BOPP film before plasma treatment: (a) distinct droplets spaced by 0.3 mm, (b) array three droplet rows thick with droplets spaced by 0.1 mm along x and y directions .....	49
Figure 51 - Genes Ink Smart Ink CS01130 on BOPP film after plasma treatment: (a) line of droplets spaced by 0.1 mm, (b) part of a 1mm by 1mm filled square with droplets spaced by 0.08 mm along x and y directions .....	49
Figure 52 - Genes Ink Smart Ink CS01130 on Wacker Elastosil film before plasma treatment: distinct droplets spaced by 0.3 mm .....	50
Figure 53 - Genes Ink Smart Ink CS01130 on Wacker Elastosil film after plasma treatment: (a) distinct droplets spaced by 0.3 mm, (b) line of droplets spaced by 0.1 mm, (c) part of a 1mm by 1mm filled square with droplets spaced by 0.1 mm along x and y directions .....	50
Figure 54 - Interdigital geometry with nominal dimensions and relevant parameters .....	55
Figure 55 - a) Microfab Jetlab 4xl, b) control panel for droplet formation parameter settings .....	56
Figure 56 - Example image of a sample acquired with Zeiss Stereo Discovery V20 optical microscope .....	59
Figure 57 - Original image acquired by Zeiss Stereo Discovery V20 optical microscope of test 21 .....	60
Figure 58 - Processed image of test number 21, having $\Delta x = 140 \mu\text{m}$ $\Delta y = 170 \mu\text{m}$ $v_p = 10 \text{ mm/s}$ $T_n = 35 \text{ }^\circ\text{C}$ , the red cross locates the minimum gap .....	60
Figure 59 - Original image acquired by Zeiss Stereo Discovery V20 optical microscope of test 14 .....	60
Figure 60 - Processed image of test number 14, having $\Delta x = 140 \mu\text{m}$ $\Delta y = 170 \mu\text{m}$ $v_p = 10 \text{ mm/s}$ $T_n = 40 \text{ }^\circ\text{C}$ , the red cross locates the minimum gap .....	60
Figure 61 - Interval plot of the mean value and standard deviation of the gap against drop spacing along the x-axis .....	63
Figure 62- Interval plot of the mean value and standard deviation of the gap against drop spacing along the y-axis .....	63
Figure 63 - Interval plot of the mean value and standard deviation of the gap against the printing speed .....	64
Figure 64 - Interval plot of the mean value and standard deviation of the gap against the nozzle temperature .....	64
Figure 65 - Example of printed sample with interconnected arrays ( $\Delta x = 80 \mu\text{m}$ , $\Delta y = 110 \mu\text{m}$ , $v_p = 10 \text{ mm/s}$ , $T_n = 40^\circ\text{C}$ ) .....	65

Figure 66 - Individual value plot of the minimum value of the gap.....	65
Figure 67 - Individual value plot of gap length.....	66
Figure 68 - a) Example of disconnection at the array beginning ( $\Delta x = 140$ mm, $\Delta y = 170$ mm, $v_p = 30$ mm/s, $T_n = 35^\circ\text{C}$ ); b) Example of intermediate disconnection ( $\Delta x = 110$ mm, $\Delta y = 140$ mm, $v_p = 20$ mm/s, $T_n = 40^\circ\text{C}$ ) .....	66
Figure 69 - Schematic of an Electro-adhesive device (EAD) with interdigitated electrode pattern: (a) cross-section and (b) a partial top view. ....	70
Figure 70 - Top view of the manufactured EAD with a detail of the printed electrodes ....	71
Figure 71 - Schematic of the test arrangement for ESS measurement .....	73
Figure 72 - A real picture showing the top-view of the test arrangement for ESS measurement .....	74
Figure 73 - ESS vs. applied voltage for Sample 1 and Sample 2, tested on aluminized PI film from 0V till specimen breakdown. ....	76
Figure 74 - Electro-mechanical response of one of the manufactured EAD specimens (Sample 1) during one cycle activation at 7kV for the grasping of the 25 $\mu\text{m}$ aluminized PI film. (a) voltage and current evolution, with a zoomed view of the transient; (b) power and energy evolution, estimated based on the voltage and current signals; (c) measured shear force. ....	77
Figure 75 - Electro-Adhesive Device (EAD) cross-section (a) and electrode strip array partial front-view (b) .....	80
Figure 76 - EAD manufactured via ink-jet printing and blade coating: full device (on the left); detail of the inkjet printed electrode traces (on the right) .....	81
Figure 77 - Schematic of the test-bench employed for ASS measurement .....	84
Figure 78 - Picture of the test-bench employed for ASS measurement .....	84
Figure 79 - Measured adhesion shear stress (ASS): mean (column) and standard deviation (error bar) values evaluated for seven nominally identical manufactured EAD specimens. (a) ASS vs EAD activation voltage for different film samples. (b) zoom for the case with .....	87
Figure 80 - Adhesion shear stress (ASS) vs applied voltage for coated PET and aluminized PI till EAD specimen breakdown.....	87
Figure 81 - Status of EAD during one cycle of charging and discharging: (a) voltage and current history from power supply monitoring signals; (b) estimated power and energy history; (c) force history from loadcell signal. ....	88
Figure 82 - Simple robotic gripper made with two opposite hanging EADs and its use for the grasping of a glass bottle: (a) gripper embodiment; (b) gripper open under no voltage, lateral	

view; (c) gripper open under no voltage, axial view; (d) gripper closed after electrical activation, lateral view; (e) gripper closed after electrical activation, axial view. ....	89
Figure 83 - Simple robotic gripper made with two opposite hanging EADs while handling different objects: (a) a water-filled glass bottle lying horizontal; (b) a water-filled glass bottle lying vertical; (c) a carbon fiber tube; (d) a cardboard box; (e) a box with with PP envelop; (f) a propanol-filled plastic bottle.....	90
Figure 84 - Schematic of the EAD design with significant geometrical parameters .....	95
Figure 85 - Manufacturing step constituting the production process adopted .....	98
Figure 86 - Example of a produced sample showing an electrode detail acquired by Jetlab® 4xl optical system (left), and geometry measurements acquired with Dino Lite USB Microscope (right).....	100
Figure 87 - (a) real arrangement of the mechanical part of the experimental setup. (b) CAD side-view of the test bench .....	101
Figure 88 - Electrical scheme of the voltage divider interfacing with the IPC input module EL3104.....	102
Figure 89 - Electrical scheme of the current monitor interfacing with the IPC input module EL3104.....	103
Figure 90 - Schematic of the interconnection between the electrical and the mechanical part of the test bench.....	103
Figure 91 - Breakdown voltage results obtained by reference geometries differing by the number of electrode strips connected to the high voltage .....	106
Figure 92 - ESS results obtained at 0 kV, 1kV, 2kV, and 3kV for all the six different manufacturing procedures .....	108
Figure 93 - Breakdown voltages mean values and standard deviations obtained by the six manufacturing procedures .....	109
Figure 94 - ESS results comparisons between M1 and M4 samples with applied voltage rising till breakdown occurrence .....	110
Figure 95 - Three different sized of the produced EADs tested for the scalability analysis .....	111
Figure 96 - ESS results comparisons of the three different size EADs for the scalability analysis .....	112

# List of tables

Table 1 - Shear stress values at corresponding applied voltage with constitutive parameters of interest obtained from literature .....	16
Table 2 - Z number of successfully inkjet printed solvents and inks .....	30
Table 3 - Experimental design summary .....	57
Table 4 - Complete experimental campaign conducted following the Run Order .....	58
Table 5 - Measurements performed by the Matlab code for test 21, having $\Delta x = 140 \mu\text{m}$ $\Delta y = 170 \mu\text{m}$ $v_p = 10 \text{ mm/s}$ $T_n = 35 \text{ }^\circ\text{C}$ .....	60
Table 6 - Measurements performed by the Matlab code for test 14, having $\Delta x = 140 \mu\text{m}$ $\Delta y = 170 \mu\text{m}$ $v_p = 10 \text{ mm/s}$ $T_n = 40 \text{ }^\circ\text{C}$ .....	61
Table 7 - ANOVA p-values (bold = significant factor, confidence level $\alpha = 5\%$ ) for the analysis on the mean value and standard deviation of the gap .....	62
Table 8 - Measured capacitance values of the two tested samples when in free air and in contact with the aluminized PI film .....	75
Table 9 - Measured Capacitance Of The Manufactured EAD Specimens: Mean And Standard Deviation (SD) Values Evaluated For Neven Nominally Identical EAD Specimens. ....	85
Table 10 - Definition of the six manufacturing procedures identified by surface treatment sequences .....	100
Table 11 - Capacitance mean value and standard deviation calculated by the measured capacitance on all samples belonging to the six different manufacturing procedures .....	107
Table 12 - Mean value calculated from the energy consumed and the power absorbed by all samples, during on test, belonging to the six different manufacturing procedures .....	108



# List of Acronyms

<b>EA</b>	Electro Adhesion
<b>EAD</b>	Electro Adhesive Device
<b>MA</b>	Magnetic Adhesion
<b>VS</b>	Vacuum Suction
<b>ESS</b>	Electro Adhesive Shear Stress
<b>IPA</b>	Isopropyl Alcohol
<b>PI</b>	Polyimide
<b>PET</b>	Polyethylene Terephthalate
<b>PEEK</b>	Polyetheretherketone
<b>PP</b>	Polypropylene
<b>DoD</b>	Drop on Demand
<b>CIJ</b>	Continuous Ink Jet
<b>CA</b>	Contact Angle
<b>WPU</b>	Waterborne Polyurethane
<b>DOE</b>	Design Of Experiment
<b>ANOVA</b>	Analysis Of Variance





# Chapter 1. Introduction

## 1.1 Electro-Adhesion (EA) applications

Electro-adhesion (EA) represents a valuable solution in applications where fragile, compliant, or variable shape objects need to be grabbed [1]. In such applications, retention action is typically preferred to a compression force. Technologies for generating retention actions between two mating surfaces can be also based on vacuum suction (VS) and magneto-adhesion (MA), which are nowadays considered as the standards, especially in high-reliability demand fields.

Conventionally used in the heavy industry for metal parts handling, but also studied for wall-climbing devices in the last decades [2], [3], MA has the cons of being effective only on electrical conductors and usually requires high currents or necessitates magnetic materials, which are becoming more expensive and harder to retrieve.

VS is nowadays the most common solution for handling almost any kind of flat object. This technology is widely deployed in the packaging industry, and it is getting more and more popular in the soft robotic field. Bio-inspired grippers are indeed appearing on the market, as demonstrated by FESTO TentacleGripper, overcoming the limitation of grasping just flat objects. Independently from the gripper design, an airtight contact between the object and the gripper, which is not achievable in porous or variable shape objects grasping, is mandatory to exert vacuum adhesive forces. Moreover, bulky compressors are always involved.

Still considered as a research topic for the last sixty years, EA was investigated in the nineteen-sixties as bonding systems for aerospace applications [4] and as fixtures for part machining [5], as well as thirty years later for the handling of cloths, fabrics, and optical micro-components [1], [6], [7]. Over the last decade, EA is receiving increasing interest in the fields of robotics, especially for the development of grippers [8]–[11] and climbing robots [12]–[15]. Comparing to MA and VS, EA carries the following advantages [1], [6]:

- Electrical activation with low energy consumption, since a device exploiting EA typically behave as a capacitor.
- Minimal effect to the adhered objects, as the electro-adhesive actions vanish very quickly away from the mating surfaces.
- Applicability to a wide range of solid materials that include dielectrics, electrical conductors, and porous media.
- Retention performances are almost independent of device size.
- Operation in a variety of settings such as in air, liquids, and vacuo.
- No complex hardware requirements, since an EA device can be represented just by two conductive plates connected to a voltage source.

## **1.2 Motivation**

Despite the advantages listed in the previous section, EA is still considered a premature and unreliable solution compared to MA and VS for practical applications such as industrial ones. EA indeed requires controlled environmental conditions for a much more effective adhesion, having the surfaces of the Electro Adhesive Device (EAD) and the object mating as ideally as possible. Non-idealities of the contact (i.e. air gaps, asperities, dust, small particles) or external unpredictable factors may cause dramatic EA forces reduction or even gripping failures.

As irregular airgaps are always present between the mating surfaces and since no ideal dielectric or electrical conductor really exists in nature, the exact fundamental principles governing the practical response of EADs are not easy to identify, and only coarse models with limited accuracy are available for estimating the prehension actions produced by them [1], [4], [16], [17]. Moreover, there is still a lack of experimental data validating existing models or defining empirical ones [1], [17]–[20]. For this reason, an analytical approach to the EA phenomenon as well as finite element analysis are not always helpful for a prior EAD design, aiming to reduce production costs and material wastes. To some extent, an experimental approach for better clarifying the EA phenomenon is more appropriate and can be the key to a proper EAD performance evaluation, addressing the EAD design and fabrication process, helping with the definition of empirical models [21].

With the rise of innovative manufacturing techniques producing flexible electronic devices, EADs can now reduce the aforementioned technical issues by a compliant contact, maximizing the adhering surface. However, low payloads usually characterize this class of actuators

compared to conventional gripping solutions, and this represents another factor that limited EADs to the purely academic world.

Nevertheless, EA grippers start appearing on the market thanks to Omnigrasp from EPFL and Grabit™ from Harvard University. The former proposed silicone-based EADs with high adhesive pressures capability but requiring additional mechanical actuation to disengage the object after accomplishing the gripping action due to silicone intrinsic high adhesive properties. The latter consists of object handling devices and conveyors for the lean productions, however featuring flat and rigid adhering surfaces.

This thesis proposes thin-film embodied lightweight Electro-Adhesive-Devices (EADs) capable of the highest EA force found in the literature, despite being characterized by a low friction coefficient in the contact surface with the object. Moreover, low power consumption and fast system time responses along with the automatic object release after switching off the EAD are some of the promising features characterizing the proposed EADs.

The inkjet printing technique for producing conductive electrodes is adopted, allowing the manufacturing of EADs as printed electronic devices, introducing high design freedom, low production times, and reasonable costs.

A characterization methodology will assess EADs's performances from the mechanical and electrical points of view. Being the EA shear force much more significant performance index compared to normal or peeling forces [8], [23], the mechanical characterization will focus on the Electro-Adhesive-Shear-Stress (ESS), following existing standard [22]. Moreover, EADs's capacitance, power and energy consumptions, time responses, and the dielectric strength of the EADs, assessed by a standard-inspired procedure [24], designates the electrical characterization. Achieved ESS values together with EADs dielectric strength will be further increased by a manufacturing optimization.

The proposed experimental characterization procedure represents a valuable method for assessing the performances of EADs for gripping applications. Even if the results reported in this thesis are related to the specific manufacturing process, deployed materials, and grasped materials, the testing procedure is extendable to other types of EADs. Indeed, the objective of this research is not only consisting of proposing a very well-performing EAD type. It additionally aims to provide validation methods for helping the introduction of such a new class of actuators in the high-reliability demand fields.



# Chapter 2. Introduction on Electro-Adhesive Devices (EADs)

Electro-Adhesive-Devices (EADs) represent a class of actuators exerting a retention pressure deployable for gripping or braking applications. As device design, morphology, configuration, and constitutive materials properties may change from one case to another, the physical principle causing such adhesive pressure is always the same.

This chapter outlines the basic physical principles governing the EA phenomenon, providing a rudimental but straightforward analytical model (2.1 ).

A review of EAD conventional architectures, manufacturing procedures, their performances, and applications will be presented in 2.3 and 2.4 respectively.

## 2.1 General working principle of EADs

An EAD exploits the electrostatic attraction occurring when charges of opposite signs are close to each other. Coulomb's law expresses in the simplest way such a phenomenon, which in the electrostatic case is defined by equation ( 1).

$$\bar{F}_{EA} = Q \bar{E} \quad (1)$$

$\bar{F}_{EA}$  is a 3x1 vector whose component represents the x, y, and z component of the electrostatic force,  $Q$  is the test charge,  $E$  is the electric field and is defined as:

$$\bar{E} (r) = \frac{1}{4\pi\epsilon_0} \int_V \frac{\rho(r')}{r^2} \hat{r} d\tau \quad (2)$$

Equation ( 2) express the Electric field  $E$  as the volume integral of the charge density  $\rho$  divided by the square of the distance from the source charge, while  $\epsilon_0$  is the vacuum permittivity and is equal to  $\epsilon_0 = 8.85 \times 10^{-12} \frac{C^2}{N \cdot m^2}$ .

From ( 2) it can be understood that the electric field distribution is a function not only of the considered volume, but it also depends on how the charge distributes in the space, hence from the geometrical configuration of the conductors where the source charges are settled. Therefore, the electric field calculation is not an easy task when the source charges distribute over fancy-shaped conductors, as it is for many practical applications.

With this in mind, a more generic discussion on the Coulomb force is more appropriate, since the EA force expression reported in ( 1) can be meaningless for modeling and simulations of real cases.

Considering a generic volume containing some stationary charges in vacuum, equation ( 1) can be replaced by the volume integral reported in equation ( 3).

$$\bar{F}_{EA} = \int_V \rho \bar{E} d\tau \quad (3)$$

The force per unit of volume is defined by the force density vector and corresponds to:

$$\bar{f} = \rho \bar{E} \quad (4)$$

Now considering the well know Maxwell first equation:

$$\nabla \cdot \bar{E} = \frac{\rho}{\epsilon_0} \quad (5)$$

And by substituting ( 5) in ( 4) we obtain:

$$\bar{f} = \epsilon_0 (\nabla \cdot \bar{E}) \bar{E} \quad (6)$$

Now we must introduce the Maxwell Stress Tensor, defined as a 3 by 3 matrix whose components are:

$$T_{ij} \equiv \epsilon_0 [E_j E_i - \frac{1}{2} \delta_{ij} E^2] \quad (7)$$

Where  $i$  and  $j$  are the x, y, and z coordinates, while  $\delta_{ij}$  is the Kronecker delta, therefore equal to 1 when  $i = j$  and equal to 0 otherwise. Thus:

$$T_{xx} \equiv \epsilon_0 \frac{1}{2} [E_{xx}^2 - E_{yy}^2 - E_{zz}^2] \quad (8)$$

$$T_{xy} \equiv \epsilon_0 [E_x E_y] \quad (9)$$

And so on  $\forall i, j = x, y, z$ .

The total 3x3 matrix is usually represented by the symbol  $\vec{T}$  and can be also written as follows:

$$\vec{T} \equiv \varepsilon_0 \bar{E} \otimes \bar{E} - \varepsilon_0 \frac{1}{2} (\bar{E} \cdot \bar{E}) \quad (10)$$

It is worth to extend all the considerations done so far to the case in which the field, generated by stationary charges, propagates in matter.

Changing ( 4) into

$$\bar{f} = \rho_f \bar{E} \quad (11)$$

Where  $\rho_f$  is the free charge density, is straight forward to obtain equation ( 12)

$$\bar{f} = (\nabla \cdot \bar{D}) \bar{E} \quad (12)$$

Where  $D$  is the electric displacement field, which for linear, isotropic, and homogeneous dielectric materials is defined as:

$$\bar{D} = \varepsilon_0 \varepsilon_r \bar{E} \quad (13)$$

With  $\varepsilon_r$  called dielectric constant. By analogy to what was done previously, the Maxwell Stress tensor now is defined as:

$$\vec{T} \equiv \bar{D} \otimes \bar{E} - \frac{1}{2} \bar{E} \cdot \bar{D} \quad (14)$$

Concluding, it turns out that the divergence of ( 10) is exactly equal to what was obtained in ( 6), and the same holds for the divergence of ( 14) and equation ( 12).

Therefore, ( 6) and ( 12) can be rewritten as:

$$\bar{f} = \nabla \cdot \vec{T} \quad (15)$$

Consequently, substituting ( 15) in ( 3) the electro-adhesive force can be written as:

$$\bar{F}_{EA} = \int_V \nabla \cdot \vec{T} d\tau \quad (16)$$

Which, thanks to Gauss theorem becomes:

$$\bar{F}_{EA} = \int_S \vec{T} \cdot \hat{n} d\sigma \quad (17)$$

$\vec{T}$  is an electrostatic stress tensor (electrodinamic stress tensor in the most general case [25]), and represents the force per unit of area acting on the surface S.  $T_{ij}$  elements are the force per

unit of area oriented in the  $i^{th}$  direction acting on an element of surface oriented in the  $j^{th}$  direction. Diagonal terms of  $\vec{T}$  (i.e.  $T_{xx}, T_{yy}, T_{zz}$ ) represents pressures while off-diagonal terms (i.e.  $T_{xy}, T_{xz}$  etc.) are the shear stresses [25].

With that said, it is now evident that if we want to compute the EA force generated by an EAD while is adhering to an object, we must surely know how  $\vec{E}$  and  $\vec{D}$  are distributed over the considered surface. Although the discussion carried out until now relies on oversimplified assumptions, like the charge stationarity and the ideal dielectric behavior, the calculation of the real electro-adhesive force is still a complex and challenging task. Unfortunately, even with a proper numerical simulation setup, implementing the geometrical model of the EAD, having specified all the material properties and the boundaries conditions, it is ambitious to obtain a simulated value of  $\vec{F}_{EA}$  fitting experimental results.

In conclusion, and in general, it is always valid that high EA forces are obtainable by producing high electric fields, by applying high voltages, and by choosing materials with high dielectric constants in the EAD design. Since high dielectric strength and excellent insulating properties usually turn into a high cost of the materials, the maximum EA force is limited.

Despite the complexity of the physics governing EA, the architecture of the devices exploiting such physical principles can be very trivial, like two conductive plates connected to a voltage source. Let's now consider a practical example of an EAD that is approaching an object. In the EAD, independently of its design, configuration, or constitutive materials, there is always an electrode couple connected to a voltage source, which will force charges to distribute over the electrodes, as schematically shown in Figure 1.

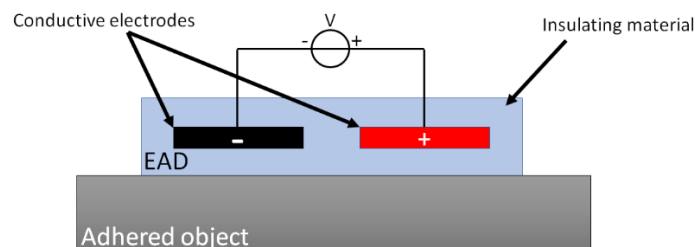


Figure 1 - Schematic of one possible arrangement of an EAD adhering to an object



Figure 1 shows one of the many possible EAD configurations, which is now useful to understand how the introduced theory can be applied to such practical example. Other existing EAD arrangements are described in the next section (2.2.1 ). For clarity, since the device architecture shown in Figure 1 corresponds to the one adopted in this research, thus having coplanar electrodes encapsulated by a dielectric, the following discussions will take this arrangement as reference.

The EA force generation takes place in two possible ways when an EAD adhere to an object, which can be conductive or an insulator. Although the analytical expression of such force can always be reconducted to equation ( 17), what really happen inside the matter can be substantially different. More precisely, adhered object can build up an image charge distribution over the adhering surface, or experience a volume polarization leading to a surface charge distribution. A simplified schematization of the electrostatic force generation is shown in Figure 2a and Figure 2b in the case of conductive and dielectric adhered object respectively, with an EAD featuring the arrangement pictured in Figure 1.

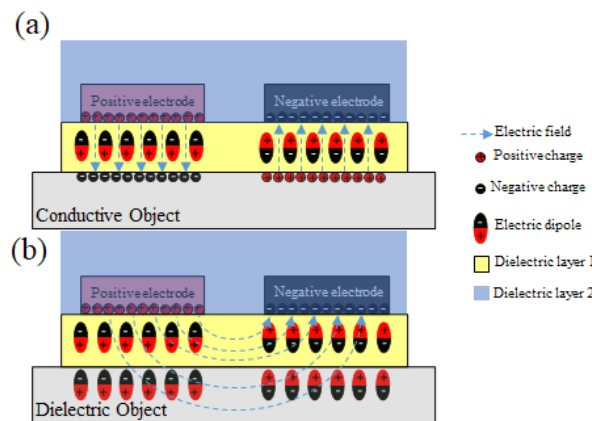


Figure 2 - Electrostatic force generation in the case of: (a) conductive object, and (b) dielectric object.

After introducing the electrostatic aspect of the EA force, it is now time to provide a rudimental but effective model of the practical adhesive force perceived when pulling an EAD away from an object, in particular, with the pulling direction aligned with the contact plane between the EAD and the adhered object.

Considering the schematic of Figure 1, we make the following assumptions:

- The EAD is powered;
- The EAD and the object are considered as rigid bodies;
- On the EAD is applied a pre-load ( $\overline{F}_N$ ), which can be its own weight as well as an additional loading force;
- The static friction coefficient between the two surfaces is  $\mu$ ;

Now, assuming that we are trying to pull the EAD parallelly to the contact plane, the resulting force diagram will be the one depicted in Figure 3, where  $\overline{F}_{EA}$  is the electro adhesive force defined in ( 17), and  $\overline{F}_S$  represents all the surface adhesion forces deriving from other physical principles, like vacuum effects or chemical attractions. The summation of these two components provides the total adhesive force, denoted as  $\overline{F}_{AD}$ .

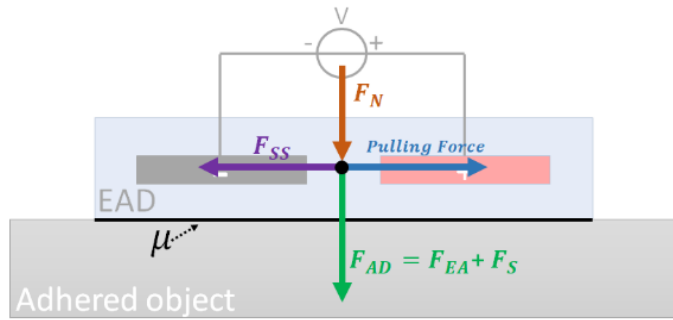


Figure 3 - Force equilibrium schematic of an EAD adhering to an object

The maximum force resisting to the pulling action is represented by  $\overline{F}_{SS}$  , and is defined as:

$$\overline{F}_{SS} = (\overline{F}_{AD} + \overline{F}_N)\mu \quad (18)$$

$\overline{F}_{SS}$  is the characterization index for the adhesive performance assessment provided by this research, and represents the maximum take-off force measured when the EAD is detached from the object by applying a pulling force. More precisely, this work refers to the Electro Adhesive Shear Stress (ESS), in order to remove EAD size dependency, and is defined as:

$$ESS = \frac{\overline{F}_{SS}}{Area_{EAD}} \quad (19)$$

### 2.1.1 Discussions

Equation ( 18) provides a simple model of what is practically happening in EAD application. However, in we consider a more realistic case, like considering matter compliancy, there are additional considerations to do, which, unfortunately, make things even more complicated:

- $\bar{F}_{EA}$  and  $\bar{F}_S$  are not independent from each other, since both affects and are affected by the effective contact area between the EAD and the object;
- Same holds for the total adhesive force  $\bar{F}_{AD}$  which is dependent on the loading force  $\bar{F}_N$ , which can also vary the contact area;

Although what was just said is unavoidable in real cases, it is still possible to experimentally evaluate the adhesive force as an almost independent variable by increasing the loading force up to the saturation point of the effective contact area. The same cannot be asserted on  $\bar{F}_{EA}$  and  $\bar{F}_S$ , which couples in a more hard-to-define manner. The proposed method, however, still represents an approximative method for real EA force assessment.

Due to varying environmental conditions, surface properties, and dynamic material responses induced by high-voltage-based polarization/depolarization effects [26], analytical models are ineffective on EAD performance prediction. Therefore, empirical modeling based on experimental data can be the key to a proper EAD performance evaluation, addressing the EAD design and fabrication process [21].

## 2.2 EAD composition and manufacturing

The EAD design and the specific process adopted for device production severely influence the attainable prehension performances. As mentioned in 2.1 , the EAD performances are affected by a considerable number of multi-domain variables, like the electrical and mechanical properties of the device. The manufacturing method, as well as the employable materials, hence directly control EAD's possible application and its performances.

This section emphasizes the relevancy of the EAD architecture and manufacturing process. All the recurring arrangements regarding EAD electrodes and dielectric layers are presented in 2.2.1 . Moreover, all the usual manufacturing techniques adopted for producing EADs will be described in 2.2.2 .

### 2.2.1 EAD design and structure

As mentioned in 2.1 , EADs always contains a couple of electrical conductors called electrodes. Besides them, the device composition can feature one or more dielectric materials, which hosts, and in some cases also insulates, the electrode couple. Three main designs can be identified, classifying the possible EAD structures by the presence of one single dielectric material, ore two dielectric materials, as show in Figure 4 [21].



Figure 4 – EAD configurations: (a) Spaced coplanar electrodes (denoted in black color) attached to a dielectric substrate (denoted in a gray color). (b) Spaced coplanar electrodes embedded in a dielectric. (c) Spaced coplanar electrodes embedded in two dielectrics (one denoted in gray and one denoted in orange). [21]

EAD electrodes can feature many different arrangements, i.e. coplanar and double-sided disposition. The classical design having coplanar electrode of alternate polarity exhibited better force performance compared to other designs [27]. On the other hand, disposing the electrodes of different polarity on opposite sides of the dielectric provides higher dielectric strength [21]. Figure 5 shows some of the possible electrode configurations for the EAD.

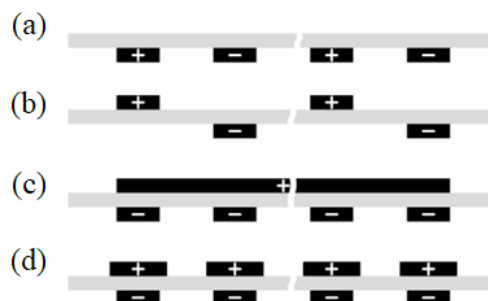


Figure 5 – (a) One-sided spaced coplanar electrodes, (b) (c) (d) double-sided spaced electrodes. [21]

Regarding electrodes geometry, two main categories can be identified: symmetrical and nonsymmetrical [21]. The most representative symmetrical patterns are the concentric [13], [23], [28], [29] (Figure 6a) and spiral [28] (Figure 6b) designs, and they are usually characterized by a more uniform EA force, comparing to nonsymmetrical electrode designs. Two-electrode [30] (Figure 6c) and interdigital or comb [8], [9], [11], [14], [15], [31]–[35] (Figure 6d) designs are the usual nonsymmetrical design. The comb-like geometry, in particular, is one of the most commonly used, due to its ease of fabrication and its good performances on grasping dielectric and conductive objects [21].

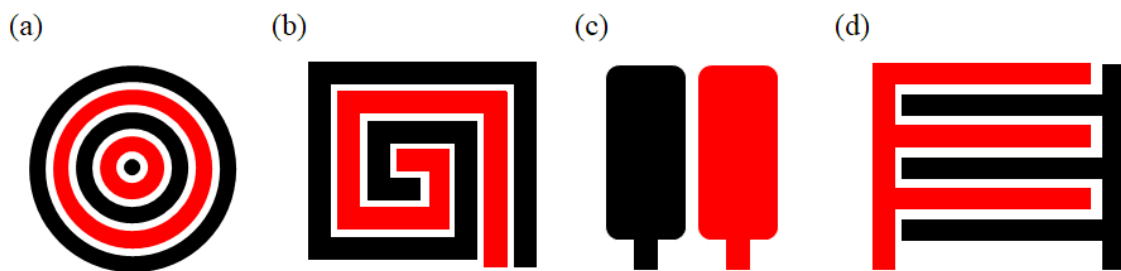


Figure 6 - EAD electrodes geometry patterns: (a) concentric, (b) spiral, (c) two-electrode, (d) comb-shape

### 2.2.2 EAD manufacturing techniques

The manufacturing process for producing EADs can be classified in additive, subtractive, and additive-subtractive [21], and they are respectively described as follows:

- Additive processes consist in three main steps, as shown in Figure 7 [21].

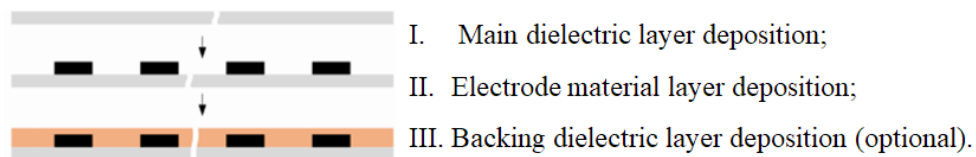


Figure 7 - Workflow of an additive manufacturing process. [21]

- Subtractive processes consist in two main steps, as shown in Figure 8 [21].

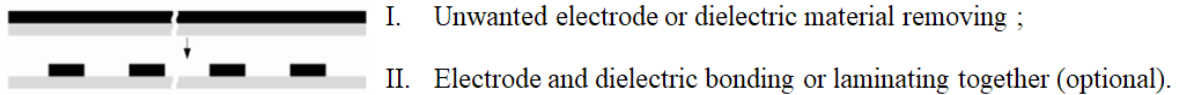


Figure 8 - Workflow of a subtractive manufacturing process. [21]

- Additive-Subtractive processes consist in three main steps, as shown in Figure 9 [21].

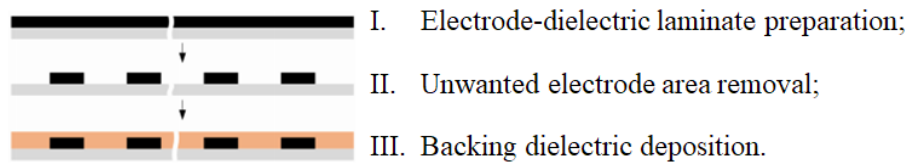


Figure 9 - Workflow of an additive-subtractive manufacturing process. [21]

For the patterning of electrodes onto the dielectric layer, and the deposition of the backing encapsulation layer, several methods have been proposed in the literature: inkjet-printing and blade coating [32], [33]; blade or laser cutting and transferring [8], [9], [11]; blade cutting and lamination [12], [38], [39]; blade coating, laser ablation and plasma bonding [8]; blade coating and blade cutting [14]; chemical etching and spin or roll coating [27], [36], [40]; photolithography and dip coating [20]. In these processes: nano-particle silver ink, copper, aluminum and conducting silicone rubber have been mostly used for the electrodes; polypropylene (PP), polyimide (PI), silicone elastomer, waterborne polyurethane (WPU) and cellulose acetate have been mostly used for the dielectric layers.

EADs can be conceived to be stiff [36], [37] or flexible [32]–[34] and, in some cases, even stretchable [8], [15]. Since prehension forces are strongly affected by the contact area between the EAD and the object, as mentioned in 2.1, the choice is driven by application requirements, which also include device resiliency. While for flat items (such as plates or plies) a planar and stiff EAD might work, in case the adhering objects have a variable shape or rough surfaces, a flexible or stretchable device is likely to be a better option, as the EAD to adapt its shape to the item surface, thereby reducing the presence of air gaps and increasing the contact area. The use of flexible and stretchable devices however complicates the fabrication, as this requires the

handling of thin flexible or stretchable films, which is more difficult than manipulating stiff wafers. The arising number of technologies for the fabrication of thin-film multilayered structures have allowed researchers to pursue different approaches for the realization of dielectric layers and electrode pairs. An EAD can thus feature a thin-film embodiment that is very compact and lightweight, enabling to be conformed to almost any shape and size.

## 2.3 ESS performances of EADs

Regarding performance, the major key index to be used for quantifying the efficacy of an EAD is the electro-adhesive shear stress (ESS), which indicates the limiting tangential force per unit of active prehension area that can be applied to the adhered object before the occurrence of sliding. Indeed, EADs show far larger resistance to shearing actions rather than to normal and peeling forces [8], [23].

ESS measurements is generally performed by using a force sensor connected to the pulled component, which can be the EAD or the object. The two possible setups arrangements are schematically shown in Figure 10. The choice of the setup configuration depends on hardware capabilities since, in the case of Figure 10a, the moving part must be connected to the powering system, which can be unfeasible in some cases. On the other hand, with the Figure 10b arrangement, the EAD is subjected to shear stress since it is constrained on the bottom side. In this case, if the exerted ESS is of the same order of magnitude as the adhesive force between EAD layers, which keeps the device integrity, the EAD might be damaged during the test.

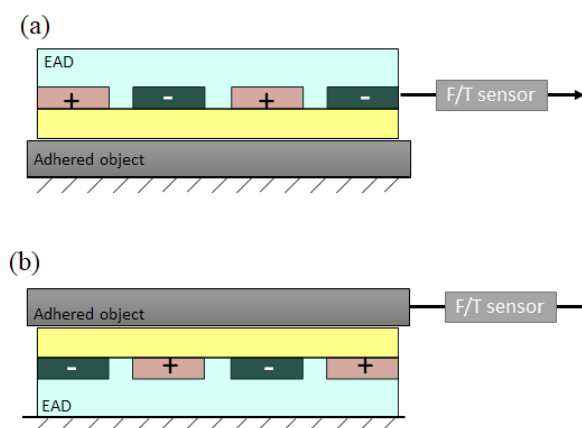


Figure 10 - Schematic of two possible setup configurations for ESS measurement: (a) the EAD is pulled while the object is fixed, (b) the EAD is kept fixed while the object is pulled away from it

ESS values reported in the literature typically range between 1 kPa and 10 kPa, and only a few works have reached 50 kPa and above. As mentioned in previous sections, ESS values are highly dependent on the geometrical, mechanical, and electrical properties of both EAD and adhering objects. For this reason, a general comparison among EAD is usually not indicative for better or worse performing devices assessment. However, exemplary results attained in previous works by EADs made with different materials and grabbing various substrates are summarized in Table 1 for a quantitative overview of ESS attainable values.

References	ESS (kPa)	Voltage (kV)	Tested Material	Main dielectric thickness ( $\mu\text{m}$ )	Electrode gap ( $\mu\text{m}$ )	EAD materials (Dielectric/Electrode)
Tellez et al. [41]	3.2	4	Steel	1000	7000	PP/Aluminum
Savioli et al. [36]	2	3	Steel	80	2000	PI/Copper
Shea et al. [8]	35	5	Paper	50	500	Silicone / Silicone + Carbon Black
Ruffatto et al. [36]	62.5	5	Glass	150	600	Silicone / Copper
Guo et al. [11]	1.4	4.8	Acrylic plate	200	3000	Silicone / Conductive Silicone
Koh et al. [17]	2.2	10	Glass	90	1200	Cellulose Acetate / Aluminum
Mahmoudzadeh et al. [27]	7.5	5	MDF	60	400	Silicone / Copper
Dadkhah et al. [40]	1.6	5	Drywall	25	400	PI / Copper
Gu et al. [12]	1.12	5	Release paper	20	-	PI / Copper
Ritter et al [39]	1.35	3.5	Aluminized PET	25	-	PI / Aluminum
Choi et al. [20]	15	1	Metal	20	1000	WPU / Copper

Table 1 - Shear stress values at corresponding applied voltage with constitutive parameters of interest obtained from literature

## 2.4 EAD applications

Thanks to the possible thin film embodiment, the high ratio between device weight and EA force, the low complexity of the required hardware, and the portability of such devices, EADs represents a versatile and promising class of actuator in a variety of application fields.

In the following sections, all the most relevant EAD applications will be reported with specific interest on EA grippers. In particular: section 2.4.1 reports all the findings in the literature concerning EA robot grippers; 2.4.2 shows haptic devices based on EA physical principle; 2.4.3 regards EA crawling and climbing robots; 2.4.4 demonstrates EAD deployed for space applications.



### **2.4.1 EA robotic grippers**

EA grippers belong to the adhesive gripper category [4], [8], [11], [42]–[49], which also includes vacuum grippers, and magnetic grippers. Adhesive grippers generate a shear holding force proportional to the normal adhesive pressure. If the gripper is characterized by a large friction coefficient, high shear forces can be achieved by a low adhesive pressure. A high ratio between shear force and adhesive closing force allows to deploy lightweight and portable grippers, suitable for handling objects that are fragile or compliant [35]. Moreover, thanks to recent innovative manufacturing techniques, EA grippers can now be manufactured in many ways, which allows the production of rigid, flexible, or even stretchable devices [21].

Rigid EA grippers usually have large area for picking up flat and heavy objects, as demonstrated in [4], [45], [48]. However, this design is not suitable for the handling of porous, non-flat, and variable shape objects. Findings in the literature of this class of EA grippers are shown in Figure 11a, Figure 11b, Figure 11c, Figure 11d.

Flexible EA grippers increase the gripper portability, since they are generally constituted by a multi-layered thin structure. Such grippers better adapt to object surfaces, comparing to rigid EA grippers, widening the gripper capability for lifting variable shape objects, without penalizing the gripper payload [4], [20], [44], [49]. Figure 11e, Figure 11f, Figure 11g, Figure 11h shows some examples of flexible EA grippers.

Stretchable EA are usually fabricated with elastomeric materials, like PDMS or rubber, and some examples are reported in Figure 11i, Figure 11j, Figure 11k. This class of material is characterized by high friction coefficients with consequent enhancement of adhesion properties of the gripper. Stretchable EA grippers morphologically adapt their shape to the adhered object, increasing also the EA action by maximizing the contact surface. However, stretchable grippers usually require additional mechanical actuation for disengaging the object after the grabbing action is performed. Moreover, elastomeric materials do not represent the best choice for the lifting of heavy objects [8], [11], [43].

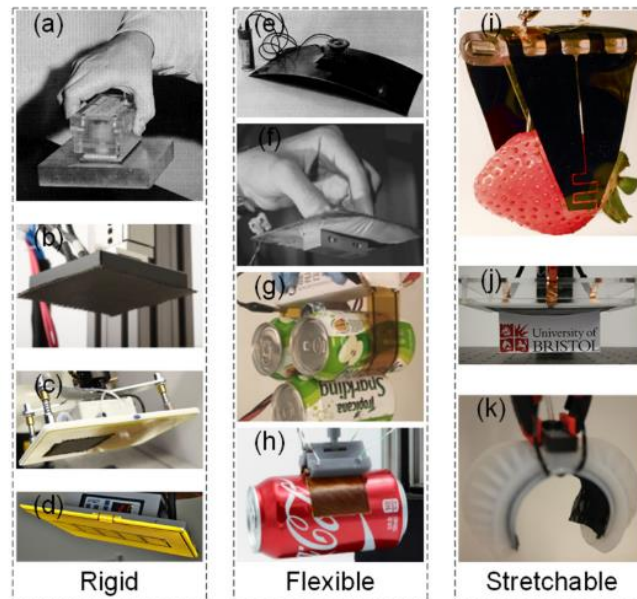


Figure 11 - EA grippers from the literature: Rigid EA grippers (a) [4] (b) [48] (c) and (d) [45], Flexible EA grippers (e) [4] (f) [44] (g) [20] (h) [49], Stretchable EA grippers (i) [8] (j) [43] (k) [11]

## 2.4.2 EA haptic devices

EA action can also be exploited for generating haptic feedback, which consists on the artificial stimulation of the touch mechanoreceptors in human skin [21]. There exist two methods for generating haptic feedback by an EA action, i.e. the mechanical vibration induced by an AC voltage signal, and the Electroadhesion generated by a DC voltage signal. In practice, the tactile sensation is generated by modulating the friction between the device and the user finger. Some representative haptic EA devices are capacitive touchscreens [50] (Figure 12a), artificial fingers [51] (Figure 12b), tactile displays [52] (Figure 12c) and shape displays [53] (Figure 12d).

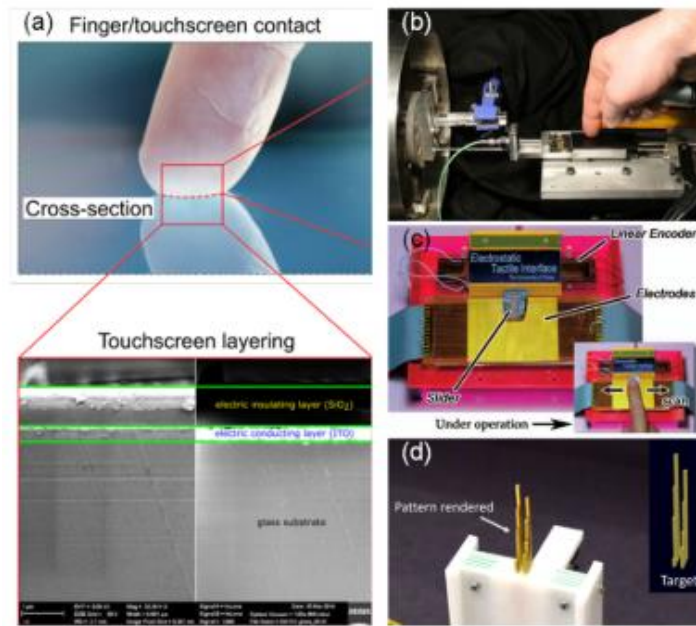


Figure 12 - EA haptic devices: (a) capacitive touchscreen [50], (b) eShiver EA artificial finger [51], (c) EA tactile display [52], (d) EA 2.5D tactile shape display [53]

### 2.4.3 EA crawling and climbing robots

Crawling and climbing robots deploy EA pads over their locomotion system. Such mobile robots can conduct given tasks in risky and hazardous environments, avoiding human operation [21]. Climbing robots can be of three different types: tracked, with single or double tracks enabling turning, legged 1-D, and legged 2-D, respectively shown in Figure 13a, Figure 13b, and Figure 13c.

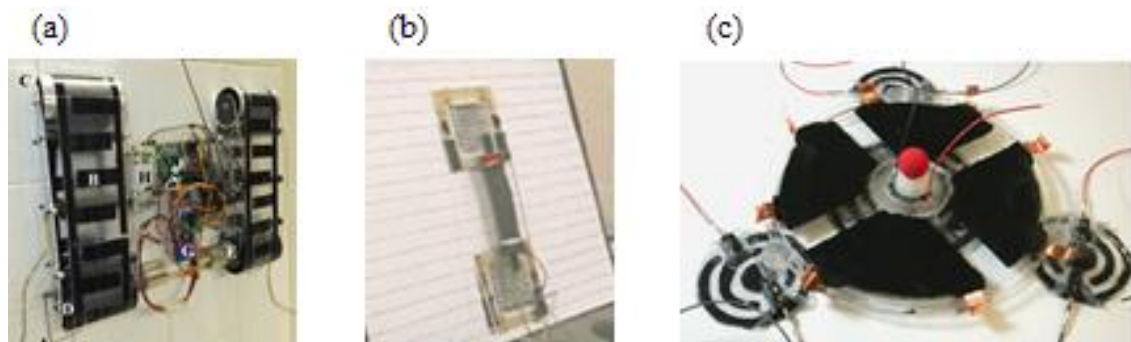


Figure 13 - EA crawling and climbing robots: (a) double tracks robot [14], (b) 1-D legged robot [55], (c) 2-D legged robot [56]

Tracked climbing robots have an EA pad which allows motion by rolling, like a tank or a tractor, while keeps the motor stucked to the ground/wall with the EA action. This kind of robots cannot avoid obstacles easily but allows the fastest moving speed among all the climbing and crawling robots. [14], [15], [54]

Legged 1-D robots normally move on plane by sliding two or more EAD connected by a linear actuator, which resembles to an artificial muscle. This robot type is characterized by a lower moving speed if compared to tracked robots. [15], [55]

Legged 2-D robots are still slow as 1-D legged ones, but they have the enhanced capability of avoiding obstacles like gaps or cracks. Two or more EADs are usually connected with actuators allowing motion out of the adhered plane. [12], [56]

#### **2.4.4 EADs for space applications**

As mentioned in 2.1 , EA gets weaker due to the earth's realistic environmental conditions, which unavoidably introduce air gaps, small particles, or humidity in the EA system, comprehending the EAD and the adhered object.

However, EA is a very effective solution in space applications where the environment is characterized by zero gravity and high vacuum. The former overcomes the EA issue of low payload if compared to MA, VS, or conventional mechanical gripping solutions. The latter allows reaching high electric fields, consequently high forces, with no air ionization.

EAD in space have been deployed for docking [39], [57], orbital debris removal [58], surface crawling and climbing [59], and material handling [59].

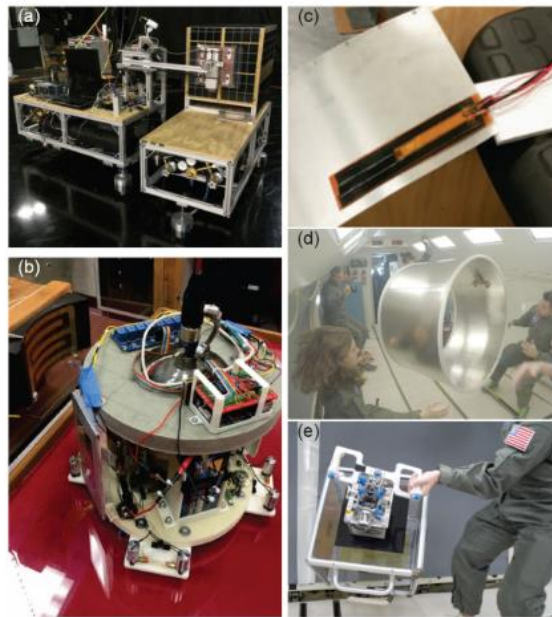


Figure 14 - EAD for space applications: (a) and (b) EA docking systems [39], [57], (c) EA pad for orbital debris retrieving [58], (d) EA climbing robots used in NASA zero gravity airplane [59], (e) EAD for material handling in space applications [59]

# **Chapter 3. DoD inkjet printing for printed electronics**

## **3.1 Introduction**

Additive manufacturing techniques are the best candidates for producing high-complexity, high-customization, and high-precision products/prototypes, reducing material waste and being cost-effective for small volume products concerning conventional or subtractive manufacturing techniques [60].

Inkjet printing is an innovative additive manufacturing technology consisting of the deposition of ink, which can be conductive or dielectric, onto a printing substrate. Inkjet printing comprises two subcategories: continuous inkjet (CIJ) and drop-on-demand (DoD) [61][62], respectively schematized in Figure 15.

In CIJ, a continuous pressurized fluid stream is electrically charged and broken into droplets by the charged deflectors driven by the printing control signal. This technique allows a high-speed printing process, jetting droplets of around 0.5  $\mu\text{L}$  at a printing frequency between 80 kHz–100 kHz. The fluid excesses are recycled from a gutter and re-entered in the printing process[62]–[64].

On the other hand, in DoD printing, a single drop is ejected from the nozzle by an electrically controlled piezoelectric actuator that squeezes the printing channel and expelling fluid drop at the jetting device orifice. This technology allows smaller drop size generation (2–500 pL) concerning CIJ but at a lower printing frequency (up to 30 kHz). Consequently, DoD is characterized by higher placement accuracy with low ink waste, having a simpler machine architecture if compared to CIJ printers [62], [63], [65].

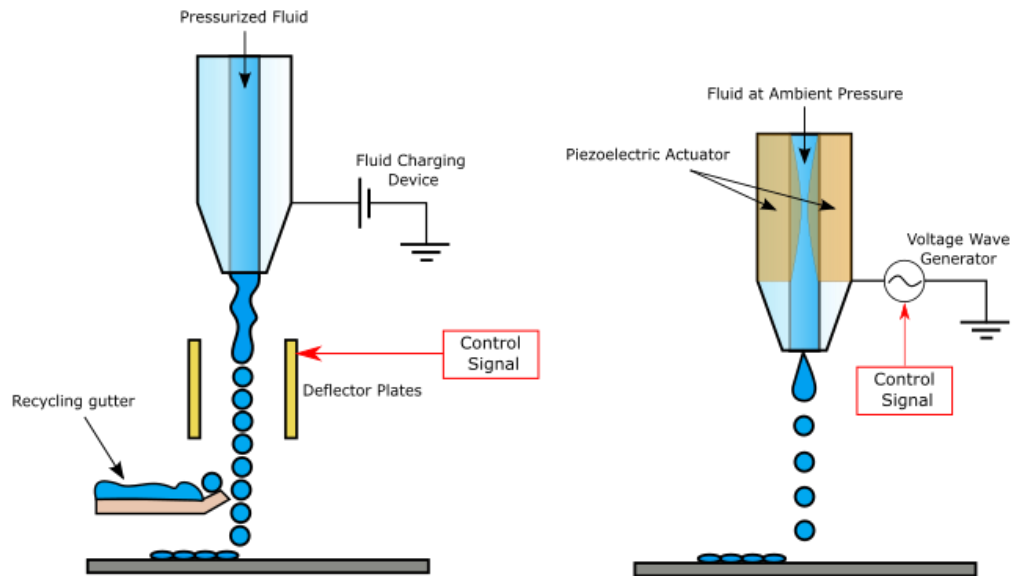


Figure 15 - CIJ (left) and DoD (right) schematization

In DoD printing, the pivotal factors when attempting to obtain a stable droplet formation and high printing quality are the following:

- The voltage waveform that causes the piezoelectric vibration.
- The back pressure of the printing channel, necessary to compensate the gravity hence obtaining a flat meniscus on the nozzle tip as shown in Figure 16.
- The temperature of the printing channel that modulates fluid viscosity.
- The ink-substrate interaction, which can be optimized by modifying surface conditions. Using specific treatments or by controlling the surface temperature.
- The fluid rheological properties that determine fluid printability, as explained in the following section.

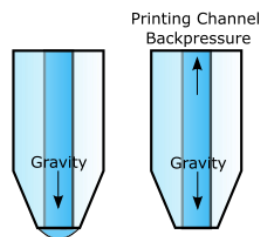


Figure 16 - Gravity compensation by the Backpressure of the printing channel

A schematic representation of a DoD inkjet printer system is shown in Figure 17.

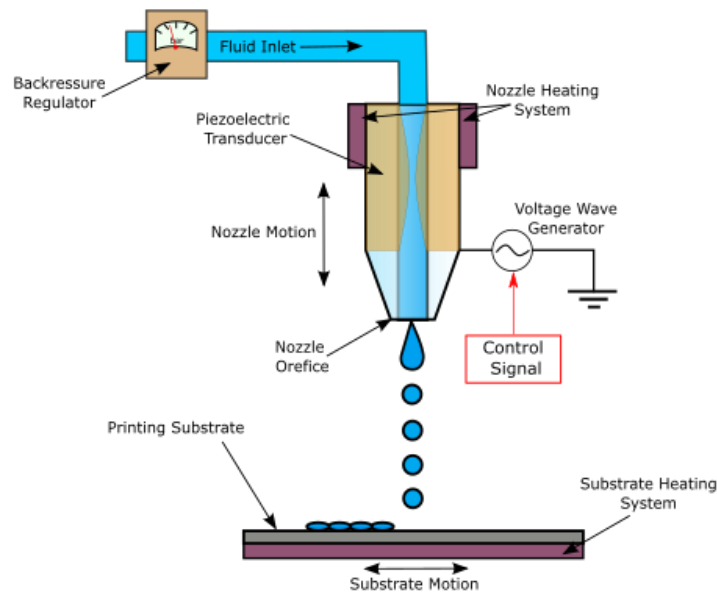


Figure 17 - Schematic of a Drop on Demand printing system

Although other printing, coating, and casting processes such as screen printing, spin-coating, or blade casting are commonly used as they offer low-cost and large covered area results [66], they involve contact with the sample and often require the use of masks. DoD inkjet printing takes advantage of its contact-free, maskless, digitally controlled operating mode to design micrometer-scaled devices.

The possibility to create flexible electronics through the DoD printing process gives access to vast employment in applications such as microelectromechanical systems [62], [63], dielectric elastomer transducers [67], and electro-adhesive devices [32]. Some examples are shown in Figure 18. All these applications need a high precision technology that works at the micrometer scale and free geometry feasibility with short fabrication time.



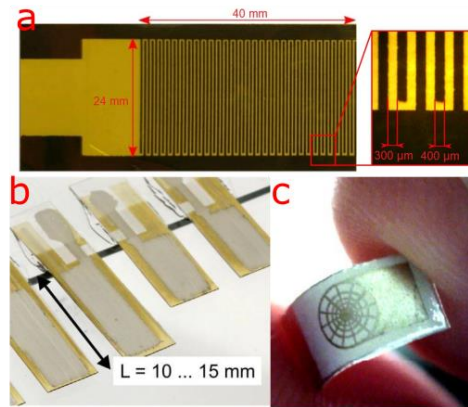


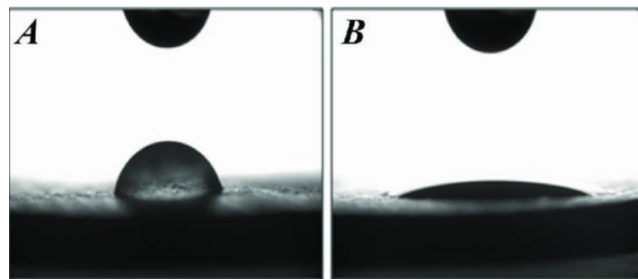
Figure 18 - Inkjet printed (a) Electro-Adhesive device [32], (b) Piezoelectric cantilever [63], (c) Infrared sensor [63]

The inkjet printing process involves two principal components that are the ink and the printing substrate. These will determine whether the final device will be a conductive patch printed on a dielectric film/wafer [32], [63], an insulating layer printed onto a circuitry [68], or a flexible polymeric structure completely printed by the inkjet printer. Therefore, the choice of the materials directly affects the final device employment. Users can exploit the versatility of the technology that allows the printing of conductive or dielectric inks indifferently.

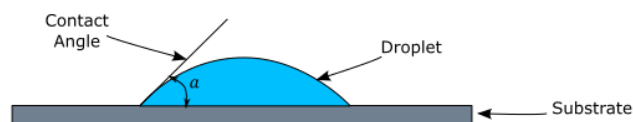
The quality of the printing strongly depends on the interaction between ink and substrate. Surface treatments aiming to optimize surface wettability (e.g. corona treatment, plasma treatment) can modify ink-substrate interaction [69]–[71] for a better printing result. Figure 19 shows the effect of 5 minutes of plasma treatment on water drops on the surfaces of non-porous HA pellets. Substrate surface wettability determines how the ink will spread after drop deposition. The contact angle (CA) of a drop on a substrate is usually used as an index to assess wettability [72], [73]. CA determines the surface energy, establishing if the surface wettability is poor or favourable [74]. Figure 20 shows how it is determined, while Figure 21 assesses angle ranges that define whether a wetting is incomplete or complete. However, measurement of the CA requires the acquisition of high-definition images profiling the deposited drop, requiring dedicated facilities. In addition, an accurate fitting model determining the profile line is necessary [75]. Finally, no standards exist for determining a procedure involving surface treatments leading to optimal CA values for any ink-substrate couple. Therefore, an experimental approach is obligatory to obtain an optimal surface condition. When CA measurement is impossible, we cannot talk about optimal wetting anymore. Indeed, we must reduce to an advantageous wetting condition determined when the ink looks stable on the

substrate, allowing homogeneous fluid distribution, filling inner areas, and maintaining defined edges of the printed shape. Too high wettability leads to uncontrolled ink spreading, while poor wettability prevents the ink from homogeneously distributing onto the surface.

Regarding the variety of printable ink, the jetting method may dramatically change depending on the ink properties. In particular, industrial inks usually allow a stable droplet formation without special precautions, making machine setting fast and consistent for long and uninterrupted printing sessions [32], [76], [77]. On the other hand, custom-made inks, like highly solvent-diluted elastomer-based solutions, require specific machine settings, making the printing procedure more problematic, requiring a periodical check of the droplet formation [67].



*Figure 19– [71] Water drops on the surfaces of non-porous HA pellets before (A) and after (B) 5 minutes of Plasma treatment*



*Figure 20-Schematic representation of contact angle between a deposited droplet and a substrate*

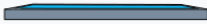



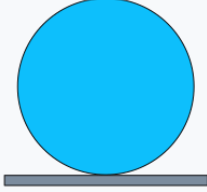
$\alpha = 0^\circ$		Spreading
$\alpha < 90^\circ$		Complete Wetting
$\alpha = 90^\circ$		Partial Wetting
$\alpha > 90^\circ$		Incomplete Wetting
$\alpha > 180^\circ$		Non-Wetting

Figure 21- Wetting quality depending on contact angle value

This chapter describes all the most important factors to consider when printing with a DoD inkjet printer. The following section describes ink rheological properties and driving voltage waveform affection on the droplet formation. The inkjet printer deployed in this context will be described with all its functionalities afterward. Finally, a section dedicated to practical examples of prints is present: firstly, reporting droplet generation with various waveforms while jetting Isopropanol, and lastly, showing and commenting droplet depositions examples on different substrates while printing conductive inks.

### 3.2 Droplet formation for DoD Piezo inkjet printers

With DoD inkjet printers, users must take care of two core factors: droplet formation and ink-substrate interaction.

Droplet formation must be stable, repeatable, and of the proper volume for high printing quality. Unrepeatable or unstable droplets are subjected to random trajectories during the flight, while a too high volume expelled from the nozzle can cause tail or satellite droplet formations. These factors will reduce droplet placement accuracy.

Ink-substrate interaction affects the printing quality after drop deposition and depends on the material involved and surface conditions. Wettability assessment through contact angle

measurement gives a quantitative analysis of ink-substrate interaction. However, an empirical approach can be enough to determine whether a wetting condition is favorable or not for high printing quality, checking top-view images of the printed geometries in micrometric scale, as it is in this thesis work. Section 3.5 will describe some examples.

Neglecting the interaction between the printing substrate and the printed fluid for one moment, the user should take care of ink printability as the first step. Droplet formation must be of prime concern for obvious reasons.

### **3.2.1 Ink printability determined by rheological properties**

Rheological properties determine fluid dynamic behavior, but fortunately, when using an inkjet printer, it is not required to be an expert of fluid dynamics, even if an idea of the basic physical principles of the phenomena is of common sense.

The piezoelectric transducer generates a pressure wave that will travel in the printing channel with a certain velocity until it reaches the nozzle orifice. Considering a defined deformation of the piezoelectric actuator squeezing the printing channel, which means fixing the driving voltage, the dynamic response of the fluid will be different depending on fluid properties like density, viscosity, and surface tension. These rheological parameters will affect the whole drop formation mechanism, determining whether the fluid will be or will not be expelled from the orifice, or if it will or will not form a long and durable drop tail, or generating satellites droplets. An empirical method to assess ink printability, based on an approximate solution of Navier-Stokes equations for the case of droplet ejection [78], is represented by a dimensionless number [79]–[81], called "Z number" and is defined by ( 20).

$$Z = \frac{\sqrt{(a\rho\gamma)}}{\eta} \quad (20)$$

Where  $\rho$  is the density ( $\text{g/mm}^3$ ),  $a$  is the orifice diameter ( $\mu\text{m}$ ),  $\gamma$  is the surface tension of the fluid ( $\text{dyn/cm}$ ),  $\eta$  is the viscosity ( $\text{cP}$ ). Depending on the combination of the printhead and ink used, past works set the printable range to be  $1 < Z < 10$  [82] or  $4 < Z < 14$  [81]. For values of  $Z$  below the lower bound, viscous forces prevent the droplet formation by dissipating the pressure pulse (Figure 22). Conversely,  $Z$  values above the upper limit cause the formation of long and long-lived tails caused by expelled volume exceedance, which turns into satellites droplets, as shown in Figure 23.

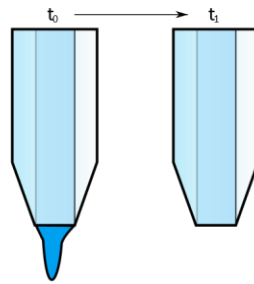


Figure 22 - Schematic of nozzle tip jetting a fluid having  $Z$  lower than lower bound: no droplet is formed

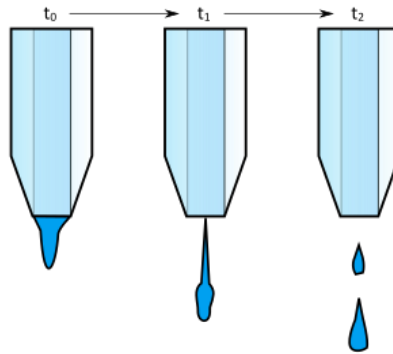


Figure 23- Schematic of nozzle tip jetting a fluid having  $Z$  over the upper bound, generating satellites droplet

Note that the  $Z$  number does not depend on fluid speed, pressure, temperature, or printer brand. Therefore, the computation of this index can be done from measurable parameters or provided by datasheets, being a quick and offline feasibility check. Table 2 shows  $Z$  numbers of various inks or solvents that have been inkjet printed.

Name	Density (g/mm <sup>3</sup> )	Surface Tension (dyn/cm)	Dynamic Viscosity (cP)	Z number (Orifice 50µm)	Z number (Orifice 40µm)
IPA (Isopropyl alcohol)	0,79	23,00	2,30	13,07	11,69
Nano Ink AX JP-60n	0,97	35,00	6,50	6,34	5,67
Orgacon IJ-1005	1,00	32,50	9,50	4,24	3,80
Anapro DGH 55LT-25C	1,40	29,00	10,50	4,29	3,84
Anapro DGP 40TE-20C	1,50	36,50	13,50	3,88	3,47
Anapro DGP 40LT-15C	1,50	37,50	14,00	3,79	3,39
Genes Ink Smart Ink CS01130	1,00	29,00	13,00	2,93	2,62
Orgacon SI-J20x	1,30	40,00	15,00	3,40	3,04

Table 2 - Z number of successfully inkjet printed solvents and inks

Reminding that all these considerations are done fixing the voltage driving waveform is substantial. The next section deeply investigates how the voltage waveform setting affects droplet formation. Printability assessment by checking the Z number is a preliminary as well as mandatory step to do. However, an improper voltage waveform setting can still lead to satellites generation or no droplet formation, even for printable fluids.

### 3.2.2 Drive voltage waveform

The driving waveform is responsible for the piezoelectric actuation generating the pressure wave, which is the cause of the droplet formation [83], [84]. A proper design of the voltage signal is indispensable for a stable droplet formation, which allows high placement accuracy hence a high printing quality. Waveforms can be single pulse or with multiple pulses. The latter can have an M- or W- shape, or in some cases being a bipolar waveform. Figure 24 schematizes all these waveforms.

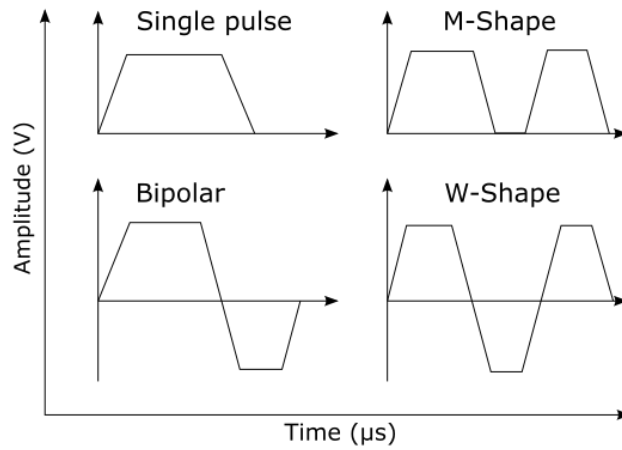


Figure 24 - Different waveform for driving voltage in DoD inkjet printing

Switching from different voltage values with a specific transition time characterize the physical solicitation the fluid is subjected to. Figure 25 simplifies how each wave phase corresponds to a specific fluid physical solicitation in the monopolar and bipolar waveform cases.

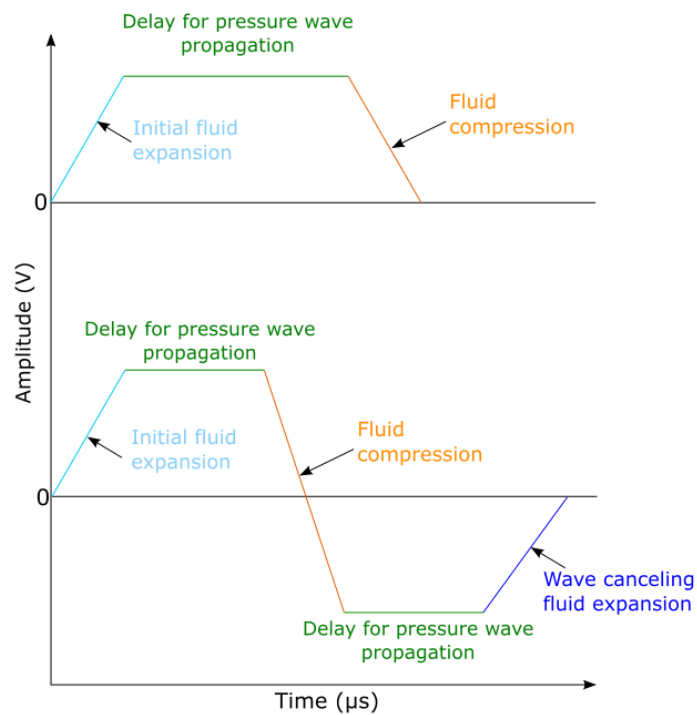


Figure 25 - Wave phases in the single pulse and bipolar case

The canonical design parameters defining the voltage waveform are depicted in Figure 26.

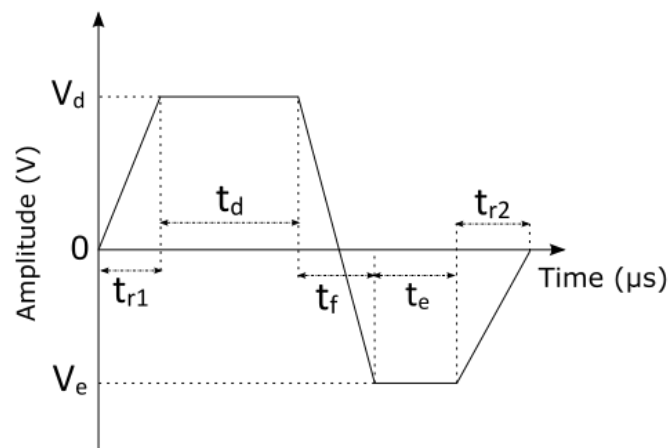


Figure 26 - Waveform design parameters for a bipolar wave

In detail:  $V_d$  is the dwell voltage;  $t_d$  is the dwell time;  $t_r$  and  $t_f$  are the rising and falling time;  $V_e$  is the echo voltage, and  $t_e$  is the echo time. For a single pulse waveform,  $V_e$  and  $t_e$  are set equal to zero. For multiple pulse profiles, like -M and -W shapes, a sub-index to the corresponding time/voltage are added, as well as for rising and falling times. Once the waveform profile has been chosen, users must tune waveform parameters to achieve an optimal parameter set. When printing fluid whose Z number is within the printable range, a single pulse waveform is usually sufficient to obtain a stable and repeatable droplet.

The optimal waveform means stably jets a droplet having adequate volume and traveling at a sufficiently high speed. Speed is necessary to preserve drop stability for the entire drop fly, from the early droplet formation until its deposition. Most often, a droplet speed between 2 - 3 m/s is optimal. Nevertheless, the optimal volume is defined by the printing accuracy constraints. If the printing accuracy must be very refined, it is worth exploring much more complex waveforms reducing droplet volume furthermore. However, if the droplet volume obtained with a single pulse wave is satisfactory, the signal tuning will be more straightforward.

For a single pulse waveform, drop speed and volume mainly depend on the pulse width and amplitude. Past works obtained the relation between speed/volume and pulse width/amplitude fixing rising and fall time, as illustrated in Figure 27 [85], [86].



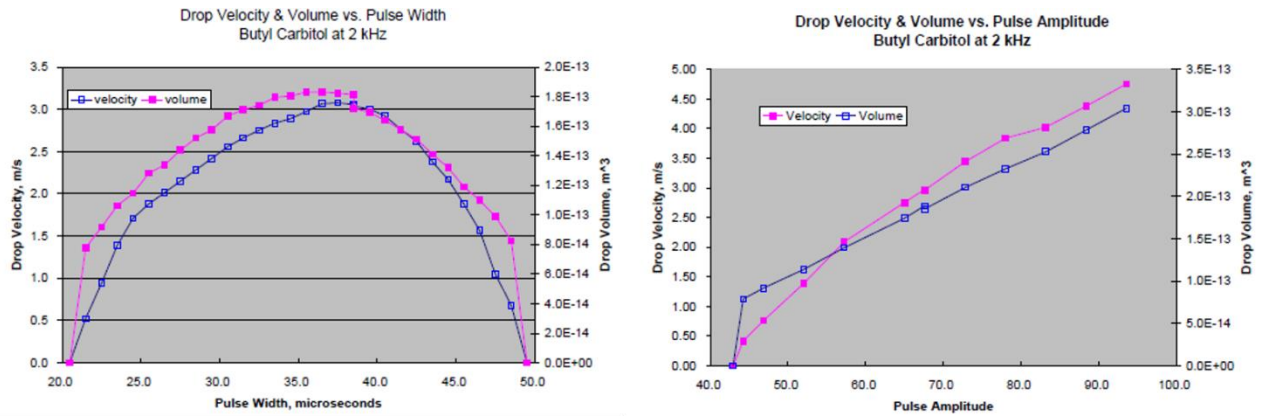


Figure 27 - Drop speed and volume relation with pulse width and pulse duration for single pulse waveform, while printing Butyl Carbitol at 2kHz with rise time of  $7\mu\text{s}$  and fall time of  $12.5\mu\text{s}$  [85], [86]

Waveform design must also consider fluid properties. In general, for printable fluids having Newtonian or near-Newtonian properties, a single pulse waveform is suitable [85]. Non-Newtonian fluids usually require more complex waveforms, having the M- or W- shape [86].

Bipolar waveforms can be used to reduce droplet volume since the opposite polarity pulse reduces fluid oscillations, especially for Newtonian fluids [85], [87]. Moreover, this waveform design demonstrated to avoid satellite droplets arising from long tails when printing high-Z-value fluids [83].

Printing speed is related to the waveform periodicity. In particular, a high printing speed means an increase of the jetting frequency, which affects the periodic response of the fluid, perturbed by the piezoelectric actuation [88]. At low ejection frequency (single pulse), the meniscus has time to relax before the next pulse is applied. Therefore, a stable and repeatable droplet generation is usually easy to achieve (Figure 28 [89]).

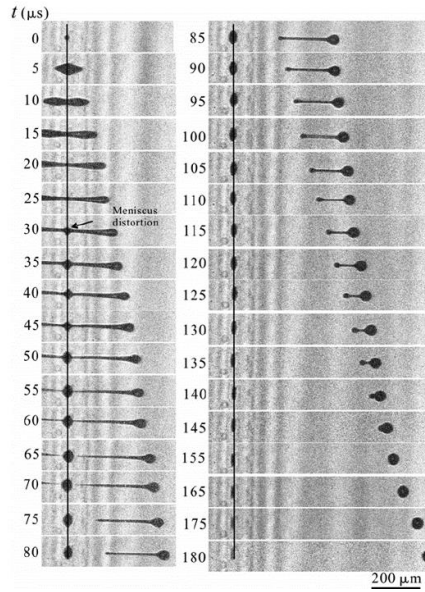


Figure 28 - Time sequence of droplet formation in response to one pulse ( $V_d = 29$  V) [89].

In contrast, at high ejection frequency (up to 30 kHz) repeatable droplet generation stage is preceded by an undesired startup stage where random droplet generation arises (Figure 29 [89]).

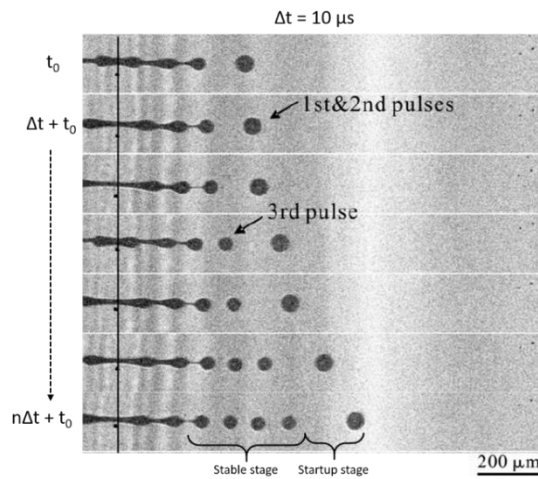


Figure 29- Jetting process of printhead divided in  $10\mu\text{s}$  time slice, with  $V_d = 25$  V and jetting frequency  $f = 33$  kHz. The startup stage contains the 1st and 2nd pulses, and the process becomes repeatable from 3rd pulse on [89].

### 3.3 Machine Description

This section describes the deployed inkjet printer: Microfab Jetlab® 4xl. Figure 30 and Figure 31 respectively depict an overview of the machine and a schematic, indicating all the main components. The following subsections provide a detailed description of machine components together with their functionalities.



Figure 30 - Microfab Jetlab® 4xl layout system

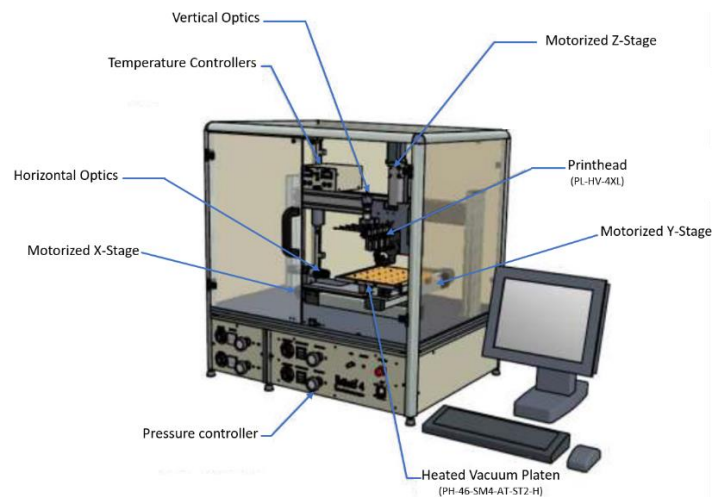


Figure 31 - Schematic of Microfab Jetlab® 4xl with main components

### 3.3.1 X-Y-Z Moving stages

The printing reference system is defined as follows:

- The x-y plane is defined by a motorized platen (PL-HV-4XL) (Figure 32), equipped with a vacuum bed and heating system (up to 120 °C) having a size of 210mm (along x-direction) and 260mm (along y-direction).
- The z-axis coincides with the vertical motion direction of the printhead (PH-46-SM4-AT-ST2-H) (Figure 33), hosting four printing channels and the jetting device heating system (up to 50°C).

Motion along 3-axes can be simultaneous, with curvilinear printing, or just along x-y axes with Print-on-the-Fly and Point-to-Point printing modes. With curvilinear printing, ink can be deposited on convex surfaces or for building 3-D microstructures. Print-on-the-Fly and Point-to-Point are planar printing techniques. Print-on-the-Fly mode speed up the printing session since x-y motion is simultaneous with droplet ejection. On the other hand, the Point-to-Point printing mode is effective for very high precision droplet placement, slowing down the printing procedure. Jetlab® 4 xl placement accuracy lies in the following range:  $\pm 30 \mu\text{m}$  for positional accuracy,  $\pm 20 \mu\text{m}$  for positional repeatability.

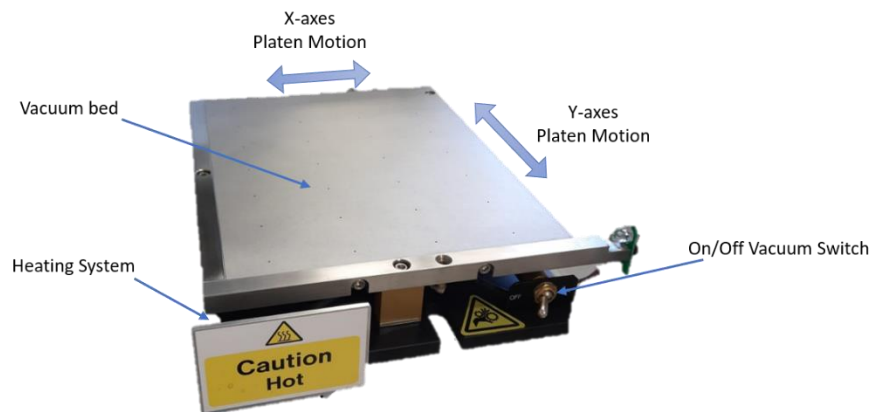


Figure 32 - Microfab Jetlab® 4xl moving platen (PL-HV-4XL), equipped with a vacuum bed and heating system

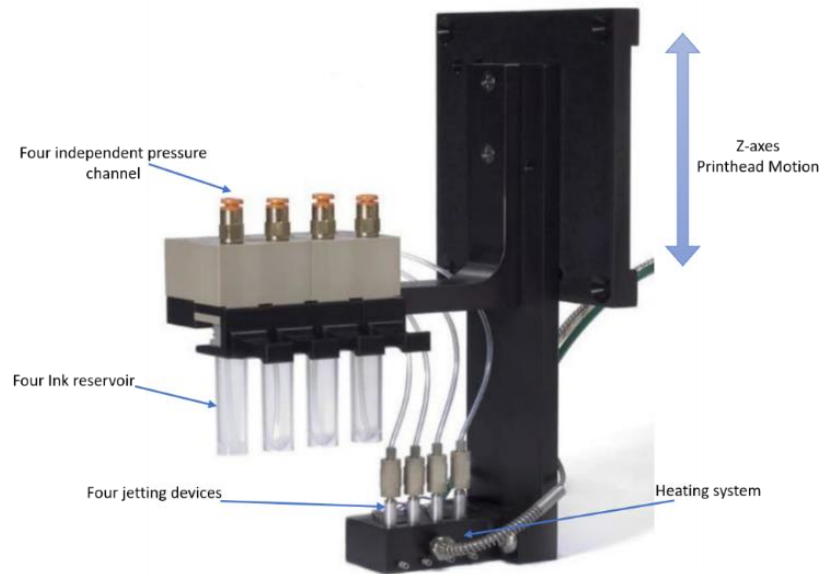


Figure 33 - Microfab Jetlab® 4xl printhead (PH-46-SM4-AT-ST2-H), hosting four printing channels and the jetting device heating system

### 3.3.2 Pressure system

Jetlab® 4 xl provides four printing channels, as illustrated in Figure 33, whose pressure can be controlled independently. As mentioned in 3.1 and Figure 16, adjusting the pressure of the printing channel is necessary to compensate for gravity force, obtaining a flat meniscus, which is essential for droplet formation. The bottom front panel of the machine hosts the pressure controller of the jetting system. Figure 34 shows the control panel of one printing channel. By the four-state knob, the printing channel can switch from "Positive" to "Negative", "Control" and "Idle" states:

- In the "Positive" state (blue in Figure 34), the printing channel is subjected to maximum positive pressure. Useful for flushing out solvents from the nozzle during cleaning sessions.
- In the "Negative" state (yellow in Figure 34), the printing channel is subjected to maximum negative pressure. Useful for back-flushing solvents from the nozzle in particular circumstances.
- In the "Control" state (green in Figure 34), the channel pressure is set by the manual pressure regulator and displayed on the control panel, also indicated in Figure 34. The "Control" state is the pressure state used during the printing sessions.
- In the "Idle" state (grey in Figure 34), the backpressure controller is Off, so the fluid is at ambient pressure.

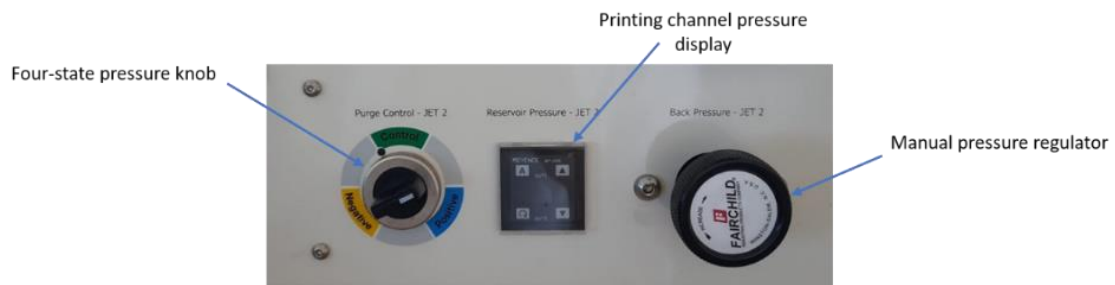


Figure 34 - Jetlab® 4 xl pressure control panel for jetting channel n°2

### 3.3.3 Heating system

As indicated in Figure 32 and Figure 33, both the printhead and the platen are equipped with a heating system having different purposes:

- The printhead temperature controls the ink temperature (usually 30°C, depending on the ink) hence reducing sensitivity from the environment. Setting the nozzle temperature allows consistent and repeatable printing sessions, and in some cases, can be used to alter ink viscosity, which, in some cases, can facilitate droplet formation.
- The platen temperature affects ink-substrate interaction. For some inks, even the printable ones, it is necessary to increase the platen temperature (usually between 40°C to 60°C) to accelerate solvent evaporation. This method increases ink stability after drop deposition, preventing undesired free movement of the ink on the substrate.

Figure 35 shows the temperature controller for the two heating systems.

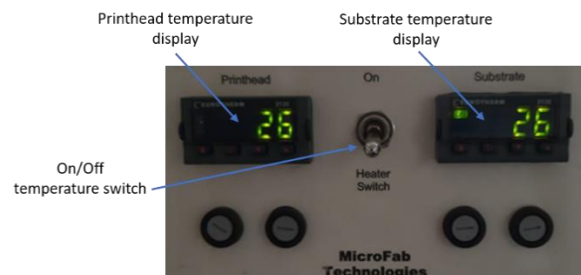


Figure 35- Jetlab® 4 xl control panel of the heating system

### 3.3.4 Vertical and Horizontal optics

Jetlab® 4 xl provides two optical systems, one for drop observation and another for printing inspection indicated respectively as horizontal and vertical optics in Figure 30.

#### 3.3.4.1 Drop observation camera

The drop observation camera is necessary to check droplet formation when the nozzle is jetting in a specific position called Maintenance Position. In the Maintenance Position, ink is not deposited onto a substrate but collected in a waste sink. This step is done preliminarily to the print and represents a standard procedure for droplet formation quality check. Stroboscopic light is synchronous with the jetting frequency, capturing a static drop image at each period. A trackbar selects a delay from the time step zero that corresponds to the instant the voltage pulse is generated, making it possible to observe the entire droplet flight. Through this acquisition method, instabilities of droplet formation are identified by non-static/vibrating droplet images, meaning that consecutive droplets have different speeds hence located in different positions after the same delay from voltage pulse generation. Figure 36 shows the layout of the drop observation optical system, while Figure 37 reports ten frames acquired from Jetlab® 4 xl observation optical system every 10  $\mu$ s while printing Isopropanol with a nozzle having 40  $\mu$ m orifice diameter.

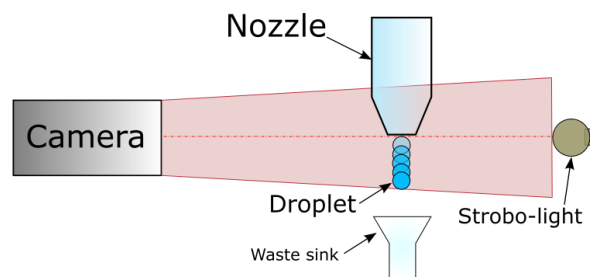


Figure 36- Schematic of drop observation camera layout



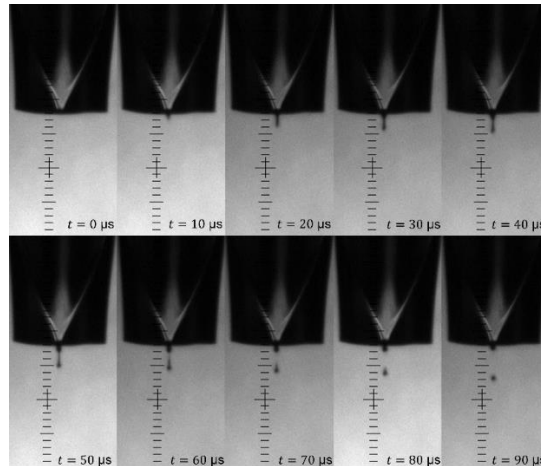


Figure 37- Droplet observation frames delayed by 10  $\mu\text{s}$  while printing Isopropanol (IPA) with a 40  $\mu\text{m}$  nozzle using a W-shape waveform

### 3.3.4.2 Print inspection camera

Printing inspection allows a quality check of drop deposition, and it can be done exclusively when the printing has finished. Even though the contact angle of deposited ink is impossible to measure with machine facilities, a top-view of the printed geometry still represents a valuable method for quality assessment. Moreover, this vertical optical system allows defining the printing starting point hence the printing reference system on the printing plate. Figure 38 illustrates a top-view detail of a conductive ink printing on a polyimide film acquired by the print inspection camera of Jetlab® 4 xl.

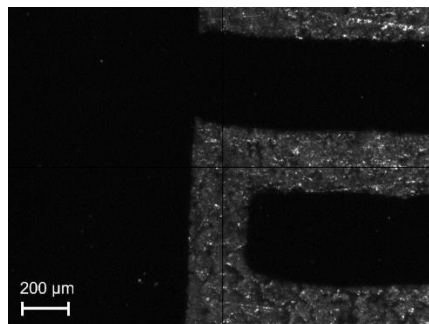


Figure 38- Top-view of a conductive ink (Anapro DGP 40LT-15C) printing (black) onto polyimide substrate (Capling PIT1N/210)



## 3.4 Droplet formation examples with Microfab Jetlab® 4xl

This section provides practical examples for droplet formation while printing Isopropyl alcohol with a jetting device having 40  $\mu\text{m}$  orifice diameter. The jetting frequency is set to 250 Hz while the printing channel backpressure is -10 mmHg. As mentioned in 3.2 , different droplet formation cases will be presented, showing outcomes of different waveform settings. For each case, waveform parameters, defined in 3.2.2 , are reported, as well as measured drop speed. Droplet observation frames from pulse generation to droplet formation will demonstrate whether tails or satellites will take place. Moreover, an example showing the effectiveness of a multiple pulse waveform on changing droplet volume is presented.

### 3.4.1 Proper formation droplet formation with single pulse waveform

Voltage waveform settings are:

- Rise and fall times fixed to 5  $\mu\text{s}$
- Dwell time of 21  $\mu\text{s}$
- Dwell voltage equal to 38 V

Figure 39 shows ten frames delayed by 30  $\mu\text{s}$  acquired by the observation optical system as described in 3.3.4.1. Measured droplet speed results to be 1.92 m/s.

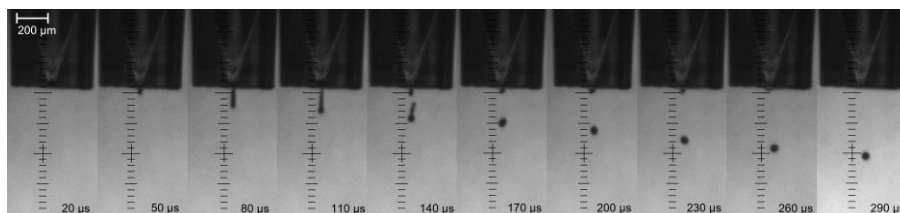


Figure 39- Proper droplet formation of Isopropyl alcohol with single pulse waveform at 250 Hz

### 3.4.2 Tail formation with single pulse waveform

Voltage waveform settings are:

- Rise and fall times fixed to 5  $\mu\text{s}$
- Dwell time of 23  $\mu\text{s}$
- Dwell voltage equal to 38 V

Figure 40 shows ten frames delayed by 30  $\mu\text{s}$  acquired by the observation optical system as described in 3.3.4.1. Measured droplet speed results to be 2.27 m/s.

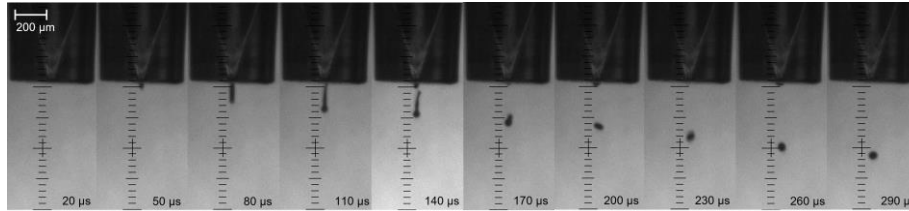


Figure 40 - Tail occurrence during droplet formation of Isopropyl alcohol with single pulse waveform at 250 Hz

### 3.4.3 Satellite droplet formation with single pulse waveform

Voltage waveform settings are:

- Rise and fall times fixed to 5  $\mu\text{s}$
- Dwell time of 43  $\mu\text{s}$
- Dwell voltage equal to 38 V

Figure 41 shows ten frames delayed by 30  $\mu\text{s}$  acquired by the observation optical system as described in 3.3.4.1. Measured droplet speed results to be 3.33 m/s.

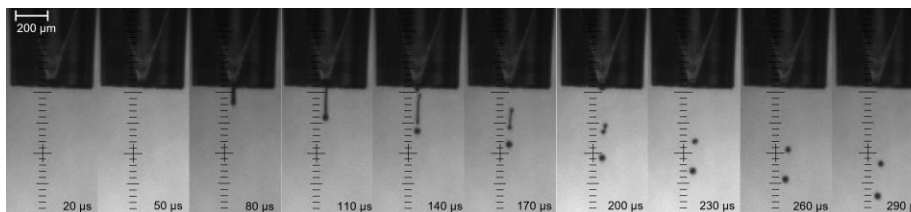


Figure 41 - Satellites droplet during droplet formation of Isopropyl alcohol with single pulse waveform at 250 Hz

### 3.4.4 Smaller volume droplet with W-shape waveform

Voltage waveform settings are:

- Rise and fall times fixed to 3  $\mu\text{s}$
- First dwell time of 20  $\mu\text{s}$
- First dwell voltage equal to 35 V
- Echo time of 3  $\mu\text{s}$

- Echo voltage of -33 V
- Second dwell time equal to 3  $\mu\text{s}$
- Second dwell voltage equal to 33 V (Figure 26).

Figure 42 shows fifteen frames delayed by 5  $\mu\text{s}$  acquired by the observation optical system as described in 3.3.4.1. Measured droplet speed results to be 4 m/s.

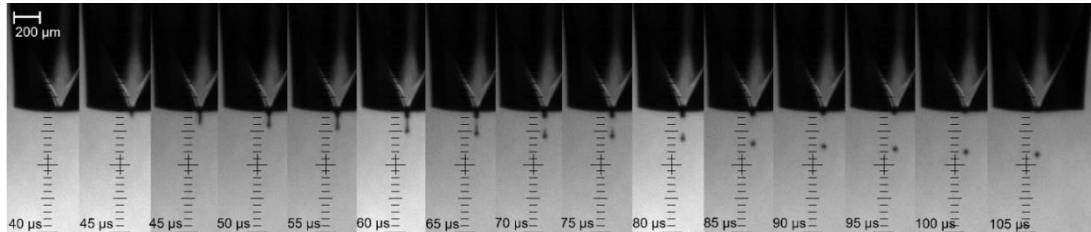


Figure 42 - Generation of smaller droplet of Isopropyl alcohol with W-shape waveform at 250 Hz

### 3.4.5 Discussions

As emerged from droplet formations reported in 3.4.1 3.4.2 , and 3.4.3 , pulse width increase led to droplet speed increase and an incrementation of the volume of the jetted fluid, as introduced in Figure 27. In this case, volume increase brings to tails formation whose length increments, as in 3.4.2 , up to the point where a satellite droplet is formed in 3.4.3 . Moreover, tail formation seems to affect droplet stability indeed, in Figure 40, at 200  $\mu\text{s}$  and 230  $\mu\text{s}$ , the droplet is deformed and blurred (3.3.4.1). In 3.4.1 , a stable droplet is obtained with a single pulse waveform, having a diameter of approximately 70  $\mu\text{m}$ . Meanwhile, in 3.4.4 , 40  $\mu\text{m}$  diameter stable droplet is obtained with a W-shape jetting waveform. In this case, fluid exceedances are retracted in the nozzle by the canceling waves propagated by successive pulses (Figure 25).

## **3.5 Droplet deposition examples with Microfab Jetlab® 4xl**

This section analyzes different droplet deposition cases while printing silver nanoparticle dispersed conductive inks onto various substrates, using a jetting device having 50  $\mu\text{m}$  diameter. The printing channel backpressure was -12 mmHg and the printing speed is set to 10 mm/s. The platen temperature was set to 50 °C while nozzle temperature was 35 °C. All the reported examples are obtained from a stable droplet formation using a single pulse waveform, whose parameters are listed in each paragraph. The analysis of the images acquired from the vertical optical system, as mentioned in 3.3.4.2, provides empirical quality assessment since contact angle measurement is impossible. Droplet deposition inspection is mandatory for determining whether the “couple” ink-substrate is favorable for devices production or not. Sections 3.5.1 3.5.2 describe favorable and adverse wetting conditions, while 3.5.3 reports two examples for wetting condition optimization through surface plasma treatment. Results will be discussed in 3.5.4 .

### **3.5.1 Favorable wetting condition examples**

A favorable wetting condition is determined whenever the following conditions are satisfied:

- Droplet having around 50  $\mu\text{m}$  diameter on flight results in a 200  $\mu\text{m} \pm 20 \mu\text{m}$  circle after deposition
- Edges of the printed shape must be straight and well defined, with no ink exceedance flowing out from the boundaries.
- The filled area must present homogeneously distributed ink in the inner regions, with no disconnected spots or sporadic ink aggregations.

#### ***3.5.1.1 Anapro silver nanoparticle ink (DGP 40LT-15C) on Polyimide film by Caplinq (PIT1N/210)***

Voltage waveform settings are:

- Rise and fall times fixed to 3  $\mu\text{s}$
- Dwell time of 33  $\mu\text{s}$
- Dwell voltage equal to 38 V

Experimental results of this ink deposition test are shown in Figure 43.

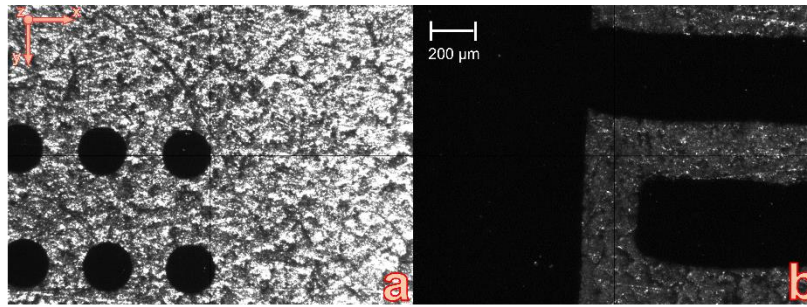


Figure 43 - Anapro DGP-40LT-15C on Caplinq Polyimide: (a) distinct droplet spaced by 0.3 mm and (b) part of an interdigitated geometry with droplet spaced by 0.17 mm along x and 0.2 mm along y directions

### 3.5.1.2 Anapro silver nanoparticle ink (DGP 40LT-15C) on PEEK film by RS Pro (764-8719)

Voltage waveform settings are:

- Rise and fall times fixed to 3  $\mu$ s
- Dwell time of 33  $\mu$ s
- Dwell voltage equal to 38 V

Substrate thickness: 25  $\mu$ m.

Experimental results of this ink deposition test are shown in Figure 44.

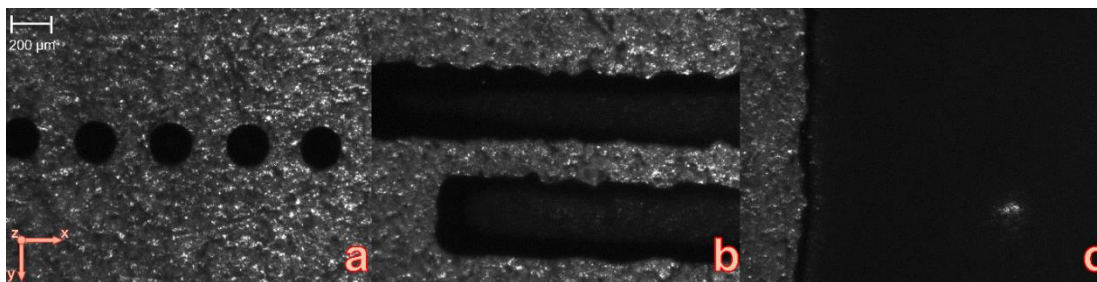


Figure 44 - Anapro DGP-40LT-15C on PEEK film: (a) distinct droplets spaced by 0.3 mm, (b) parallel arrays two droplet rows thick with 0.2 mm of spacing along x and y directions between droplets, (c) part of a 1mm by 1mm filled square with droplet spaced by 0.16 mm along x and 0.15 mm along y

### 3.5.1.3 Anapro silver nanoparticle ink (DGP 40LT-15C) on Mylar film by RS Pro (785-0795)

Voltage waveform settings are:

- Rise and fall times fixed to 3  $\mu$ s

- Dwell time of 33  $\mu\text{s}$
- Dwell voltage equal to 38 V

Substrate thickness: 25  $\mu\text{m}$ .

Experimental results of this ink deposition test are shown in Figure 45.

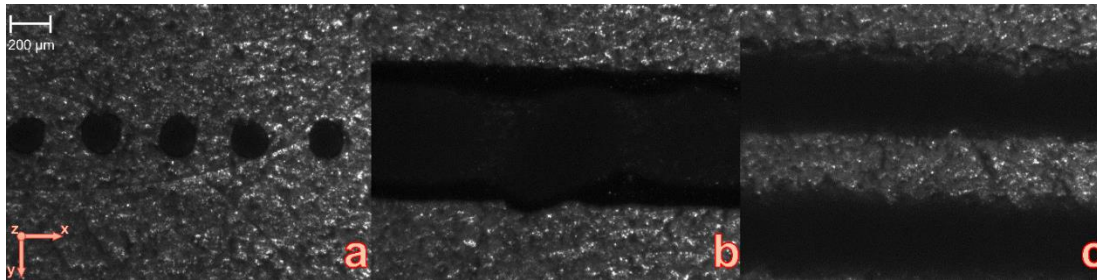


Figure 45 - Anapro DGP-40LT-15C on Mylar film: (a) distinct droplets spaced by 0.3 mm, (b) array four droplet rows thick with droplet spaced by 0.17 mm along x and 0.18 mm along y, (c) parallel arrays two droplet rows thick with droplet spaced by 0.17 mm along x and y directions

#### 3.5.1.4 Anapro silver nanoparticle ink (DGP 40LT-15C) on PolyK ultrathin free-standing PET film

Voltage waveform settings are:

- Rise and fall times fixed to 3  $\mu\text{s}$
- Dwell time of 33  $\mu\text{s}$
- Dwell voltage equal to 38 V

Substrate thickness: 5.5  $\mu\text{m}$ .

Experimental results of this ink deposition test are shown in Figure 46.

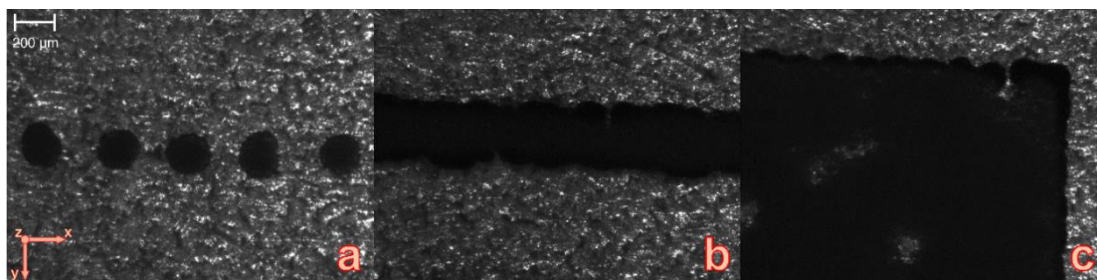


Figure 46 - Anapro DGP-40LT-15C on PET film: (a) distinct droplets spaced by 0.3 mm, (b) array two droplet rows thick with droplet spaced by 0.09 mm along x and 0.11 mm along y, (c) part of a 1mm by 1mm filled square with droplet spaced by 0.17 mm along x and y directions



### 3.5.2 Adverse wetting condition examples

Unfavorable wetting conditions are determined whenever one or more of the following events take place:

- Droplets have a diameter of less than 150  $\mu\text{m}$  after deposition.
- Edges of the printed shape are not well defined.
- The filled area presents lots of holes in the inner regions.

#### 3.5.2.1 Anapro silver nanoparticle ink (DGP 40LT-15C) on PolyK PVDF-MDO film

Voltage waveform settings are:

- Rise and fall times fixed to 3  $\mu\text{s}$
- Dwell time of 33  $\mu\text{s}$
- Dwell voltage equal to 38 V

Substrate thickness: 14  $\mu\text{m}$ .

Experimental results of this ink deposition test are shown in Figure 47.

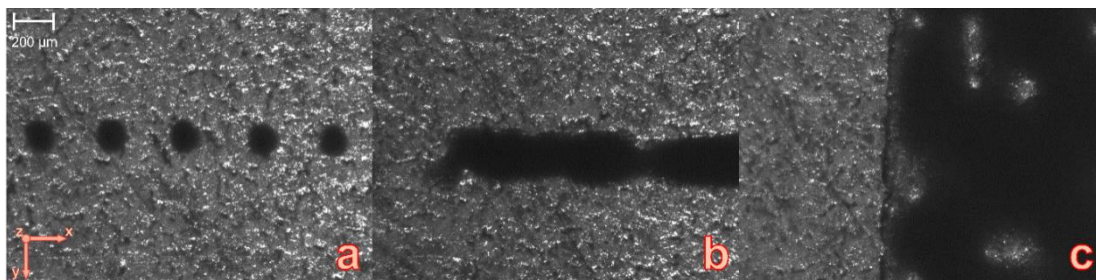


Figure 47 - Anapro DGP-40LT-15C on PVDF-MDO film: (a) distinct droplets spaced by 0.3 mm, (b) array two droplet rows thick with droplets spaced by 0.15 mm along x and y directions, (c) part of a 1mm by 1mm filled square with droplet spaced 0.15 mm along x and y directions

#### 3.5.2.2 Anapro silver nanoparticle ink (DGP 40LT-15C) on PolyK PEN film

Voltage waveform settings are:

- Rise and fall times fixed to 3  $\mu\text{s}$
- Dwell time of 33  $\mu\text{s}$

- Dwell voltage equal to 38 V

Substrate thickness: 8  $\mu\text{m}$ .

Experimental results of this ink deposition test are shown in Figure 48.

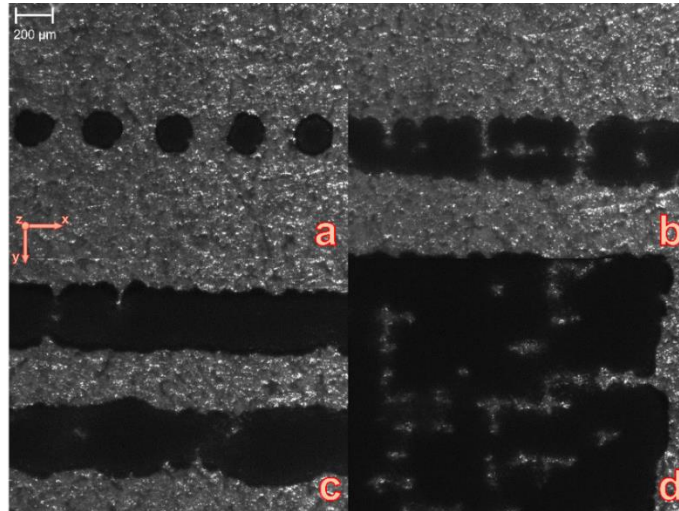


Figure 48 - Anapro DGP-40LT-15C on PEN film: (a) distinct droplets spaced by 0.3 mm, (b) array two droplet rows thick with droplets spaced by 0.19 mm along x and 0.18 mm along y, (c) parallel arrays two droplet rows thick with 0.18 mm of spacing between droplets along x and y directions, (d) part of a 1mm by 1mm filled square with droplets spaced by 0.16 mm along x and y directions

### 3.5.3 Wetting condition improvement via plasma treatment

When deposited droplets have a much lower diameter than the one specified in 3.5.2 , exhibiting light reflection, it is licit to suppose that contact angle value belongs to the “Incomplete wetting” or “Non-wetting” case, as mentioned in Figure 21. In this highly adverse wetting condition, the deposition experiment is replicated, having the substrate surface treated with oxygen plasma for one minute, with a power of 60 W and setting the pressure of the chamber at 0.8 bar.

#### 3.5.3.1 Genes Ink Smart Ink silver nanoparticle ink (CS01130) on Kopafilm BOPP film

Voltage waveform settings are:

- Rise and fall times fixed to 3  $\mu\text{s}$
- Dwell time of 32  $\mu\text{s}$
- Dwell voltage equal to 40 V

Substrate thickness: 5.8  $\mu\text{m}$ .



Plasma-untreated ink deposition test are shown in Figure 49, while deposition test after plasma treatment are in Figure 50.

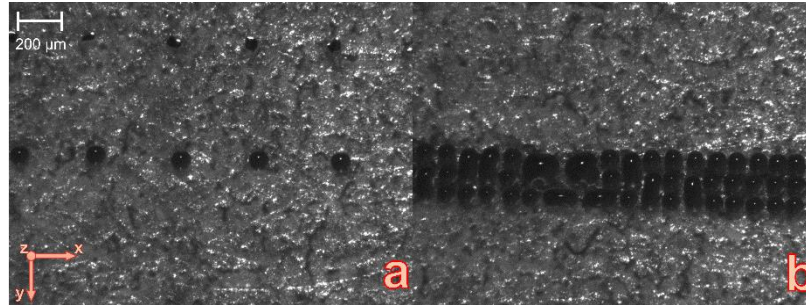


Figure 49 - Genes Ink Smart Ink CS01130 on BOPP film before plasma treatment: (a) distinct droplets spaced by 0.3 mm, (b) array three droplet rows thick with droplets spaced by 0.1 mm along x and y directions

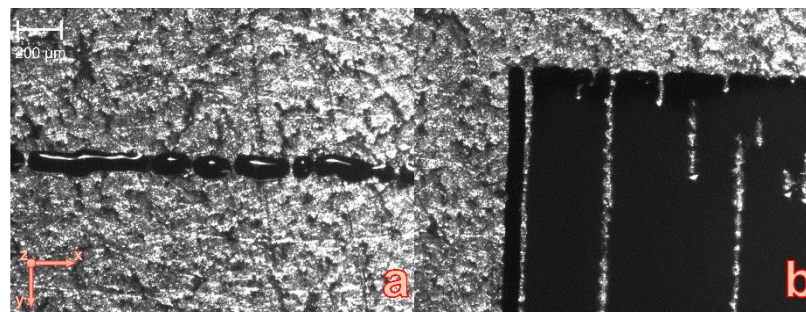


Figure 50 - Genes Ink Smart Ink CS01130 on BOPP film after plasma treatment: (a) line of droplets spaced by 0.1 mm, (b) part of a 1mm by 1mm filled square with droplets spaced by 0.08 mm along x and y directions

### 3.5.3.2 Genes Ink Smart Ink silver nanoparticle ink (CS01130) on Wacker Elastosil film

Voltage waveform settings are:

- Rise and fall times fixed to 3  $\mu$ s
- Dwell time of 32  $\mu$ s
- Dwell voltage equal to 40 V

Substrate thickness: 50  $\mu$ m.

Plasma-untreated ink deposition test are shown in Figure 51, while deposition test after plasma treatment is in Figure 52.

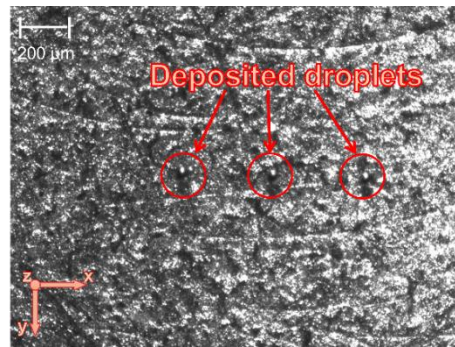


Figure 51 - Genes Ink Smart Ink CS01130 on Wacker Elastosil film before plasma treatment: distinct droplets spaced by 0.3 mm

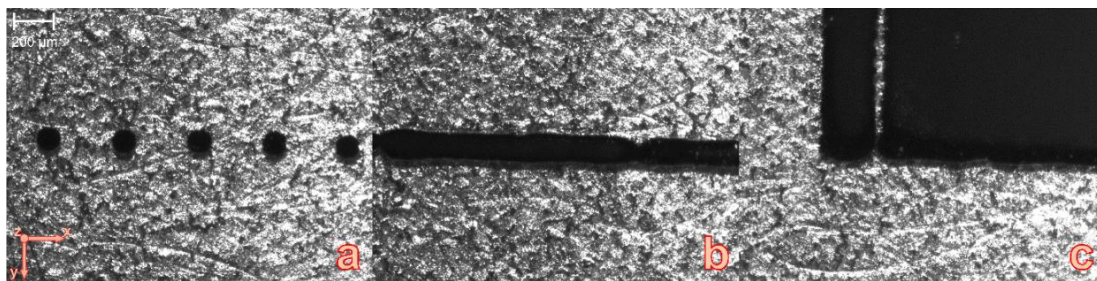


Figure 52 - Genes Ink Smart Ink CS01130 on Wacker Elastosil film after plasma treatment: (a) distinct droplets spaced by 0.3 mm, (b) line of droplets spaced by 0.1 mm, (c) part of a 1mm by 1mm filled square with droplets spaced by 0.1 mm along x and y directions

### 3.5.4 Discussions

Examples reported in this section highlighted how the interaction ink-substrate might dramatically vary when changing printing substrate but jetting the same ink. Moreover, the practical meaning of “good quality” printing or “good wetting condition” was given, as shown in 3.5.1.1, 3.5.1.2, 3.5.1.3, and 3.5.1.4. All these cases allowed straight lines printing having well-defined boundaries with a homogeneous infill, as shown in Figure 43b, Figure 44b, Figure 44c, Figure 45b, Figure 45c, Figure 46b, Figure 46c. These took place when droplet diameter after deposition was around 200 μm, with the considered inks and substrates while using a 50 μm diameter nozzle. On the other hand, in 3.5.2.1, deposited droplets had a 150 μm diameter, as shown in Figure 49a, suggesting an unfavorable wetting condition leading to undesired effects on ink deposition like forming irregular boundaries (Figure 49b) and empty spots in the inner regions (Figure 49c). However, as in 3.5.2.2 Figure 48a, even if the deposited droplets

had a diameter of around 200  $\mu\text{m}$ , deposited ink was not keeping the desired shape, still leading to same undesired effects as shown in Figure 48b and Figure 48c. Deposited droplet diameter indeed represents an approximate index for the optimal wettability assessment. By only checking this index, it is difficult to predict whether an ink-substrate couple is favorable or not for achieving high printing quality. Still, it can provide a straightforward method for identifying extremely adverse wetting conditions. Worst cases of wettability are represented by 3.5.3.1 and 3.5.3.2. Droplet's diameter was below 100  $\mu\text{m}$ , representing Non-Wetting or Incomplete wetting conditions. When printing filled geometries, droplets preferred to isolate instead of wetting the substrate surface, as in Figure 49b. For these cases, BOPP and PDMS surfaces were plasma-treated for one minute, and the deposition experiment was repeated. As shown in Figure 50b, if compared with Figure 49b, ink spreading increased significantly, although empty spots are still present. In the case of a PDMS substrate, plasma treatment has dramatically changed the surface conditions, as can be noted comparing Figure 51 with Figure 52a, where a 40  $\mu\text{m}$  diameter droplet turns into a 150  $\mu\text{m}$  diameter droplet, indicating a significant wetting increase. From Figure 52b Figure 52c can indeed be appreciated how the ink spreading is kept stable while printing a single line or a filled square, presenting well-defined boundaries and a homogeneous infill. Example reported in 3.5.3.2 proved that surface plasma treatment can make usable a substrate that was showing extremely adverse wetting condition.



# **Chapter 4. Assessing the relationships between interdigital geometry quality and inkjet printing parameters**

## **4.1 Introduction**

This chapter proposes a methodology to set a suitable range for relevant printing parameters with the aim of ensuring a good accuracy of the result while printing an interdigitated geometry, considering the DoD inkjet printer described in 3.3

Being the considered experiments affected by several variables, like ink properties or environmental conditions, which are not considered in this context, expecting that this systematic approach will evaluate an optimal printing parameter set is a very ambitious target. However, the outcome of this study still provides useful and validated results that increase the reliability of the printer setting process, giving an additional tool for implementing such manufacturing technology for EADs production in the high-reliability demand fields.

It must be taken into account that outcomes of this procedure are related to the specific ink-substrate couple adopted in this context. However, the methodology proposed can be extended to any other ink or substrate material.

The relevant printing parameter set is identified by the user experience, with the aim of reducing the number of variables affecting the experiments but still considering the factors dominantly affecting the printing process, which were defined as:

- the spacing between subsequent drops deposited on the substrate, along x and y directions;
- the printing speed, that is the travelling speed of the printhead;
- the nozzle temperature, as mentioned in 3.3.3 ;

The mentioned parameters were varied in order to assess the relationship between parameters values and printing accuracy, after a stable droplet formation was achieved, as described in 3.4.1 . Parameters values range was defined by a preliminary empirical approach, allowing a considerable experiments reduction. This preliminary empirical approach is mandatory to avoid testing completely unfeasible parameter values, like too wide spacings or too high printhead speed.

The droplet spacing, as can be trivially understood, directly controls the geometry shape by affecting ink spreading. Too close droplets can cause unwanted ink accumulations, leading to exceedances and uncontrolled formation of irregular boundaries. Conversely, droplet located too far from each other might prevent contiguous line formation, leading to dashed or dotted geometries. However, even if a satisfactory printing result can be achieved by an empirically defined spacing, it is not trivial to find the best suiting spacing configuration for the specific desired geometry, which requires a more systematic method.

The printing speed can cause droplet instabilities or droplet trajectory deviation, especially during reversal of motion of the printhead. Too high speed implies also high accelerations of the printhead during the printing session, increasing inertial forces, machine vibrations and viscous friction caused by the air, which can be very affective on the droplet flight.

The nozzle temperature affects the ink properties, hence the ink behaviour during and after the ejection from the nozzle tip. In general, fluid temperature modulates its viscosity, and after several tests, it was noticed that changing nozzle temperature modifies the printing outcomes.

A geometry consisting of two interlocked comb shapes, commonly known as interdigital geometry, was chosen as a representative example since it requires precise printed lines spaced by a homogeneous gap. Moreover, such geometry is recurring in this thesis due to its common deployment in electro-adhesion applications.

Printed patches were analysed by an image processing algorithm developed in Matlab environment. The algorithm provides measurements of parameters of interest, allowing a statistical study on the whole set of data. The study objective was achieved thanks to a proper experimental campaign, which was developed according to Design of Experiments (DoE).

## 4.2 Geometry design and manufacturing

Two interdigital geometries are printed so that the comb-fingers are interposed one to each other. Figure 53 shows the nominal dimensions of the selected reference geometry, indicating that the printed shape is designed to cover  $148,2 \text{ cm}^2$ , having  $300 \mu\text{m}$  of distance between the thin strips. The distance between two fingers is named hereafter as “gap”, the line describing the path within the fingers is named as “gap length”,  $v_p$  indicates the printing speed.

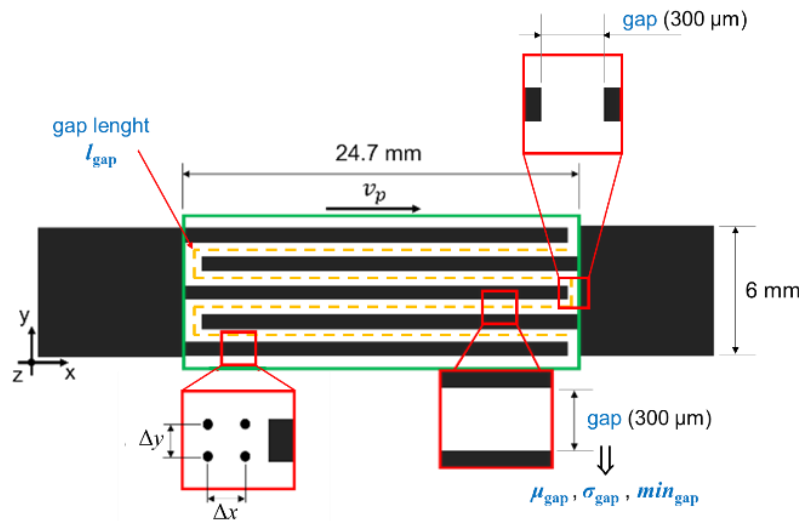


Figure 53 - Interdigital geometry with nominal dimensions and relevant parameters

The MicroFab Jetlab 4xl printer, described in 3.3 , with a  $50 \mu\text{m}$  diameter piezoelectric nozzle is used for the ink deposition (Figure 54a). The interdigital geometry is printed as a combination of several drop arrays, formed by droplet rows and columns. The printing direction corresponds to the main length of the array always referred as the x-direction.

A commercial conductive silver-nanoparticle ink (Smart 'Ink S-CS01130 from Genes 'Ink) is used to print the tested samples due to the high ink stability for droplet formation, good reproducibility of the geometries and its low resistivity (around  $15 \mu\Omega/\text{cm}$ ). The ink is prepared to be printed by filtering it with a  $0,45 \mu\text{m}$  PTFE syringe filter and 5 minutes of ultrasonic bath to dissolve any particle aggregation. Once the geometry is printed, the ink is cured in oven at  $150^\circ\text{C}$  for 40 minutes.

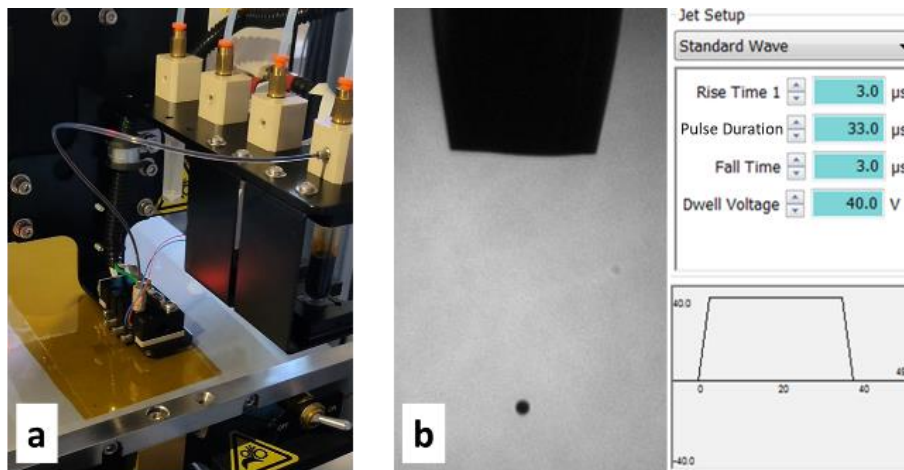


Figure 54 - a) Microfab Jetlab 4xl, b) control panel for droplet formation parameter settings

The printer setup, involving the voltage waveform and the backpressure of printing channel, is adjusted to obtain a stable drop flight [90], [91] and kept constant throughout the entire experimental design. Referring to droplet formation parameters described in 3.2.2, a monopolar trapezoidal wave is used, having rise and fall times fixed to 3 μs, dwell time of 43 μs, and dwell voltage equal to 38 V, as shown in Figure 54b, which also depicts the resulting stable droplet formation. The reservoir pressure is set to -10 Pa, leading to a flat ink meniscus at the nozzle tip.

A polyimide (PI) film 25.4 μm thick is used as substrate. The substrate is industrially produced in rolls by Caplinq (PIT1N/210), and it has been preferred to a custom realization to guarantee the uniformity of the substrate avoiding interference with the ink distribution in the printed pattern.

### 4.3 Experimental procedure

Table 3 summarizes the values range of the design parameters, hereafter denoted as factors, that are:

- Droplet spacing along the printing direction, denoted as  $\Delta x$
- Droplet spacing along the direction orthogonal to the printing direction, denoted as  $\Delta y$
- The printing speed, denoted as  $v_p$
- The printhead nozzle temperature, denoted as  $T_n$



Factors' variability was discretized into "high" and "low" values, based on preliminary experiments and in accordance with machine positioning tolerance (i.e.  $\pm 30 \mu\text{m}$  in the x-y directions). The resulting different experimental conditions are  $2^4 = 16$  and two replicates were carried out for each experimental condition, resulting in 32 runs. Additionally, the central point for droplet spacing and printing speed is added to the experimental process, corresponding to  $v_p = 20 \text{ mm/s}$ ,  $\Delta x = 110 \mu\text{m}$  and  $\Delta y = 140 \mu\text{m}$ . Five replicates were carried out for the central points at each temperature level. Therefore, the whole experimental design included 42 runs, which were completely randomized.

Factor	Symbol	Levels	
		Low	High
x-axis spacing ( $\mu\text{m}$ )	$\Delta x$	80	140
y-axis spacing ( $\mu\text{m}$ )	$\Delta y$	110	170
Printing speed (mm/s)	$v_p$	10	30
Nozzle temperature ( $^\circ\text{C}$ )	$T_n$	35	40

Table 3 - Experimental design summary

Table 4 lists the experiments parameter setup and the corresponding order of execution of tests. As can be noted, there is no correlation between consecutive experiments regarding the factors value variation. All tests were conducted at room temperature and during the same day.

Run Order	$v_p$	$\Delta x$	$\Delta y$	$T_n$	16	20	110	140	35
1	10	80	170	35	17	30	140	110	40
2	30	80	170	35	18	30	140	170	35
3	10	80	170	40	19	10	80	110	40
4	30	140	170	40	20	20	110	140	40
5	10	80	110	35	21	10	140	170	40
6	30	140	170	40	22	20	110	140	35
7	10	140	110	40	23	10	140	170	40
8	20	110	140	35	24	10	140	110	35
9	20	110	140	40	25	30	80	110	35
10	10	140	170	35	26	30	80	170	35
11	30	140	170	35	27	30	80	110	40
12	20	110	140	35	28	30	80	110	35
13	30	80	170	40	29	20	110	140	35
14	10	140	170	35	30	20	110	140	40
15	30	80	170	40	31	20	110	140	40

32	30	80	110	40	38	30	140	110	35
33	10	80	170	40	39	30	140	110	40
34	10	80	170	35	40	10	80	110	40
35	20	110	140	40	41	10	80	110	35
36	30	140	110	35	42	10	140	110	40
37	10	140	110	35					

Table 4 - Complete experimental campaign conducted following the Run Order

The outcomes of this study are defined to provide statistical indices representing the geometry homogeneity and quality. The responses of such factorial experiment were analyzed by means of the Analysis of Variance (ANOVA). The model adopted and the calculation of the responses is discussed in the following section, which provides the acquisition methods and the post processing procedure.

## 4.4 Measurements and analysis

The geometrical parameters to be evaluated (Figure 53), denoted as outcomes, are defined as follows:

- mean value of the gap ( $\mu_{\text{gap}}$ );
- standard deviation of the gap ( $\sigma_{\text{gap}}$ );
- minimum value of the gap ( $\text{min}_{\text{gap}}$ ): this parameter can highlight singularities in the contour lines, such as extra ink deposits, and interconnections between the arrays;
- gap length ( $l_{\text{gap}}$ ): this parameter shows if there are some disconnections in the arrays.

### 4.4.1 Image acquisition and processing

A Zeiss Stereo Discovery V20 optical microscope was used to acquire the printed samples, providing high resolution images having  $3.942 \frac{\mu}{\text{pixels}}$  conversion parameter. An example of an acquired image of a sample is shown in Figure 55.



Figure 55 - Example image of a sample acquired with Zeiss Stereo Discovery V20 optical microscope

MATLAB code was run to extract the geometrical parameters by using image processing algorithms. Classical image process functions acquire features of the printed sample, isolating binarized and labeled blobs. The reference geometry is composed by only two distinct blobs, identified by the two combs, spaced by  $300\ \mu\text{m}$  along the gap length. Images presenting more than two blobs contains isolated or disconnected shapes, which are removed from the analyzed image by comparing the blobs area.

The image is later compared to reference dimensions. The region of the interdigitated strips is analyzed by calculating the Euclidean distance between the two blobs, identifying the combs. Being the reference gap  $300\ \mu\text{m}$ , if the measured distance exceeds a certain threshold (set to  $500\ \mu\text{m}$ ) it will not be considered in the gap calculation. In doing so, strips disconnection from rectangles on the sides or strip interruptions in random spots will not affect the calculation of the gap mean value and standard deviation but will reflect on the calculation of the gap length.

$\mu_{\text{gap}}$ ,  $\sigma_{\text{gap}}$  and  $\min_{\text{gap}}$ , are the mean value, standard deviation, and minimum value of the whole set of distances calculated for each pixel on the shape border for which (*gap distance* < *gap threshold*). The gap length  $l_{\text{gap}}$  corresponds to the number of pixels for which a gap distance is calculated, converted in millimeters. Comparing  $l_{\text{gap}}$  with the reference value of  $110\ \text{mm}$ , it is possible to identify strips disconnections.

The Matlab code additionally calculates the median of the gap, denoted as  $\text{median}_{\text{gap}}$ , and counts the number of empty spots, denoted as  $\#_{\text{internal holes}}$ . These two additional parameters are not used in the DoE process; however, they provide additional indices for quality assessment.

#### 4.4.1.1 Image processing examples

Two explanatory examples are reported hereafter: Figure 56, Figure 57 and

Table 5 shows the measurements outcomes and the processed image corresponding to a case in which the strips were all connected to the rectangles on the sides; Figure 58, Figure 59 and

Table 6 instead, reports an example of disconnected strips, with corresponding geometry measurements performed by Matlab script.



Figure 56 - Original image acquired by Zeiss Stereo Discovery V20 optical microscope of test 21



Figure 57 - Processed image of test number 21, having  $\Delta x = 140 \mu m$   $\Delta y = 170 \mu m$   $v_p = 10 \text{ mm/s}$   $T_n = 35 \text{ }^\circ\text{C}$ , the red cross locates the minimum gap

$min_{gap} (\mu m)$	$\mu_{gap} (\mu m)$	$median_{gap} (\mu m)$	$\sigma_{gap} (\mu m)$	$l_{gap} (mm)$	$\#_{internal \text{ holes}}$
<b>228,6</b>	<b>330,4</b>	<b>327,8</b>	<b>19,5</b>	<b>99,339</b>	<b>459</b>

Table 5 - Measurements performed by the Matlab code for test 21, having  $\Delta x = 140 \mu m$   $\Delta y = 170 \mu m$   $v_p = 10 \text{ mm/s}$   $T_n = 35 \text{ }^\circ\text{C}$

In this example (Table 5, Figure 57) it can be noticed that the gap mean and median indicates a geometry characterized by gap distances close to the nominal value, with a variance below  $20 \mu m$ , suggesting a good printing results. However, the number of internal holes is considerably high, and it is crucial on detecting such printing outcome, characterized by good gap distances but a non-homogeneous infill.



Figure 58 - Original image acquired by Zeiss Stereo Discovery V20 optical microscope of test 14



Figure 59 - Processed image of test number 14, having  $\Delta x = 140 \mu m$   $\Delta y = 170 \mu m$   $v_p = 10 \text{ mm/s}$   $T_n = 40 \text{ }^\circ\text{C}$ , the red cross locates the minimum gap

$min_{gap} (\mu m)$	$\mu_{gap} (\mu m)$	$median_{gap} (\mu m)$	$\sigma_{gap} (\mu m)$	$l_{gap} (mm)$	$\#_{internal\ holes}$
<b>206,3</b>	<b>297,9</b>	<b>274,0</b>	<b>73,1</b>	<b>2,199</b>	<b>505</b>

Table 6 - Measurements performed by the Matlab code for test 14, having  $\Delta x = 140 \mu m$   $\Delta y = 170 \mu m$   $v_p = 10 mm/s$   $T_n = 40 \text{ }^\circ C$

On the other hand, in the example shown in Table 6 and Figure 59, a gap length equal to 2.2 mm indicates the presence of many disconnected strips, since the reference gap length is around 110 mm. Gap mean, median and variance are calculated from the gap distance between the strip tips and the rectangle on the right side.

#### 4.4.2 Design of the Experiment modelling

This paragraph aims to introduce how the design of the experiment was modelled, to better understand how the factors levels, as referred in Table 3, are affecting the observed outcomes. No detailed explanation on the ANOVA method is present since it was not the focus of this work.

The observation of a response in a factorial experimental plan can be described by a model, in particular, a *fixed effect model* was used [92]. Considering a two-factors factorial experiment design, just to make it simpler for a better understanding, and since the discussion can be extended to a four-factor design, which represents our case of study, the observed response of our statistical study  $y_{ijk}$  at the  $i^{\text{th}}$  level of factor A,  $j^{\text{th}}$  level of factor B and at  $k^{\text{th}}$  replication, is defined as follows:

$$y_{ijk} = \mu_{ij} + \epsilon_{ijk} \begin{cases} i = 1,2,3 \dots a \\ j = 1,2,3 \dots b \\ k = 1,2,3 \dots n \end{cases} \quad (21)$$

Where  $a$  is the number of levels for factor A with,  $b$  is the number of levels for factor B,  $n$  is the number of replications,  $\epsilon_{ijk}$  is an aleatory error component while  $\mu_{ij}$  is a deterministic component corresponding to the mean at the specific  $ij$  levels, defined as:

$$\mu_{ij} = \mu + \tau_i + \beta_j + (\tau\beta)_{ij} \quad (22)$$

Where  $\mu$  is the overall mean,  $\tau_i$  is the effect of  $i^{\text{th}}$  level of factor A,  $\beta_j$  is the  $j^{\text{th}}$  effect of factor B and  $(\tau\beta)_{ij}$  is the effect of the interaction between  $\tau_i$  and  $\beta_j$ , with  $\sum_{i=1,a} \tau_i = 0$ ,  $\sum_{j=1,b} \beta_j = 0$ ,  $\sum_{i=1,a} (\tau\beta)_{ij} = 0$ ,  $\sum_{j=1,b} (\tau\beta)_{ij} = 0$ .

We can now introduce the testing hypothesis for each factor and interaction, and they are defined as:

$$\text{For factor A} \rightarrow H_0 : \tau_1 = \tau_2 = \tau_3 = \dots \tau_a = 0$$

$$H_1 : \text{at least one } \tau_i \neq 0$$

$$\text{For factor } B \rightarrow H_0 : \beta_1 = \beta_2 = \beta_3 = \dots \beta_b = 0$$

$$H_1 : \text{at least one } \beta_j \neq 0$$

$$\text{For factors interaction } \rightarrow H_0 : (\tau\beta)_{ij} = 0 \quad \forall i, j$$

$$H_1 : \text{at least one } (\tau\beta)_{ij} \neq 0$$

The formulated hypotheses are tested by using the ANOVA. The resulting test statistic, for which the calculation methodology can be founded in [92], allows to reject the considered null hypothesis  $H_0$ , meaning that the corresponding factor is significant for the statistical study, or to accept  $H_0$ , meaning that there is no affection on the observed outcome by the considered factor.

Extending what just said to four-factors case and considering factors levels listed in

Table 3, the presented model was applied to our case of study, having  $(\Delta x, \Delta y, v_p, T_n)$  as experimental factors and  $(\mu_{\text{gap}}, \sigma_{\text{gap}})$  as observed outcomes.

A confidence level  $\alpha = 5\%$  was selected and p-values of each statistic test was calculated. For  $p - \text{values} < \alpha$ , the corresponding  $H_0$  is rejected, indicating that the considered factor is significant for the statistic. The ANOVA calculation was performed with a statistical software.

## 4.5 Results and discussions

Table 7 summarizes the ANOVA results, showing the statistically significant factors, among the ones listed in Table 3, for the calculation of gap mean value and gap variance. Moreover, the plots in Figure 60, Figure 61, Figure 62, and Figure 63 depict the results related to the mean value and standard deviation of the gap for each factor.

Factors		P-value	
		$\mu_{\text{gap}}$	$\sigma_{\text{gap}}$
Main factors	$\Delta x$	<b>0.000</b>	<b>0.001</b>
	$\Delta y$	<b>0.000</b>	<b>0.000</b>
	$v_p$	0.166	0.243
	$T_n$	<b>0.030</b>	0.199
Interactions	$\Delta x * \Delta y$	<b>0.000</b>	<b>0.043</b>
	$\Delta x * v_p$	0.088	0.405
	$\Delta x * T_n$	<b>0.043</b>	<b>0.003</b>
	$\Delta y * v_p$	0.769	<b>0.021</b>
	$\Delta y * T_n$	0.523	0.353
	$v_p * T_n$	0.721	0.201

Table 7 - ANOVA p-values (bold = significant factor, confidence level  $\alpha = 5\%$ ) for the analysis on the mean value and standard deviation of the gap

Based on the ANOVA results resumed in Table 7, both responses are affected by the drop spacing along the X and the Y axes. As both factors increase, the mean size of the gap shows values that are higher and closer to the nominal value (300  $\mu\text{m}$ ), while the standard deviation decreases (Figure 60, Figure 61).

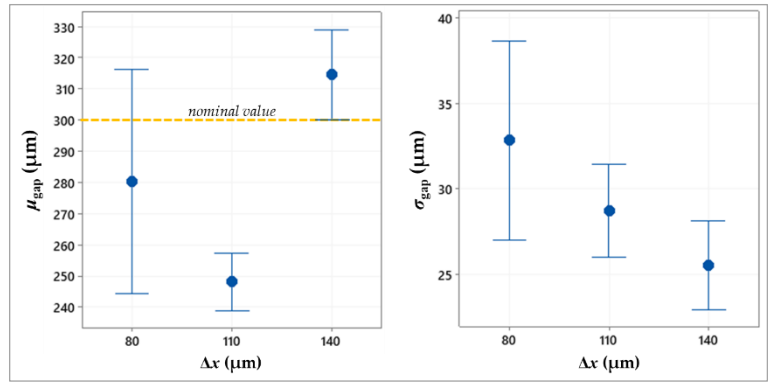


Figure 60 - Interval plot of the mean value and standard deviation of the gap against drop spacing along the x-axis

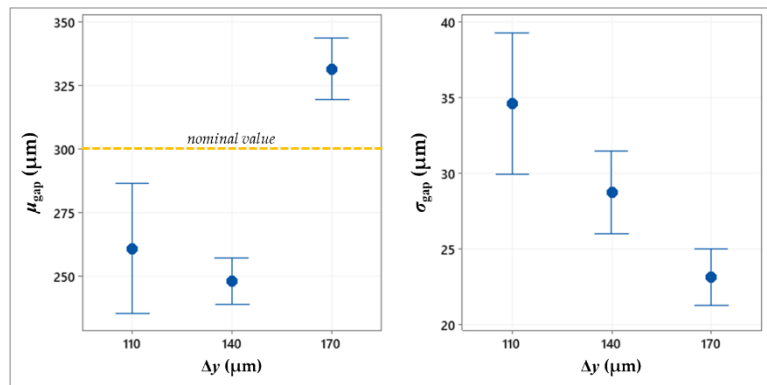


Figure 61- Interval plot of the mean value and standard deviation of the gap against drop spacing along the y-axis

Figure 62 shows the affection of the printing speed on the mean value and the variance of the gap.  $\mu_{\text{gap}}$  resulted close to the reference value for printing speed equal to 10 and 30 mm/s, while at 20 mm/s the gap mean is around 250  $\mu\text{m}$ . The gap variance, instead, is stable around 29  $\mu\text{m}$  for all speed values, but with significant oscillation decrease at 20 mm/s.

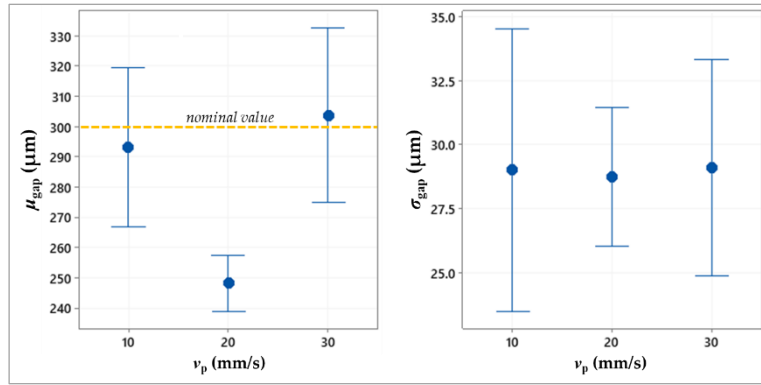


Figure 62 - Interval plot of the mean value and standard deviation of the gap against the printing speed

The nozzle temperature proved to affect the mean size of the gap, whose value decreases as the temperature increase (Figure 63). This is probably caused by the dependence of ink viscosity from the temperature, which results in a higher ink spreading when the temperature increases.

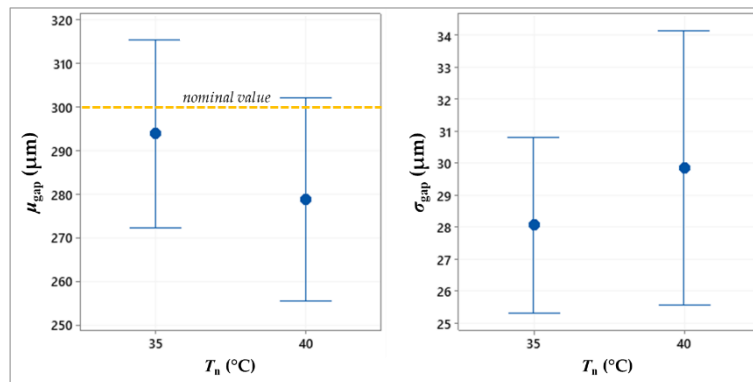


Figure 63 - Interval plot of the mean value and standard deviation of the gap against the nozzle temperature

A higher spacing between the subsequent drops, regardless of the direction, reduces the drop overlapping and, thus, the spreading of excess ink. Therefore, this allows to obtain lines that are less thick and more regular, helping to respect the target size and shape of the gap ( $\sigma_{\text{gap}} = 25.5 \pm 4.9 \mu\text{m}$  at  $\Delta x = 140 \mu\text{m}$  and  $\sigma_{\text{gap}} = 23.2 \pm 3.4 \mu\text{m}$  at  $\Delta y = 170 \mu\text{m}$ , as shown in Figure 60 and Figure 61). Conversely, lower spacing leads to undesired ink exceedances causing non-homogeneous boundaries, with consequent reduction of the gap mean value and increase of the gap standard deviation (e.g. in Figure 64).



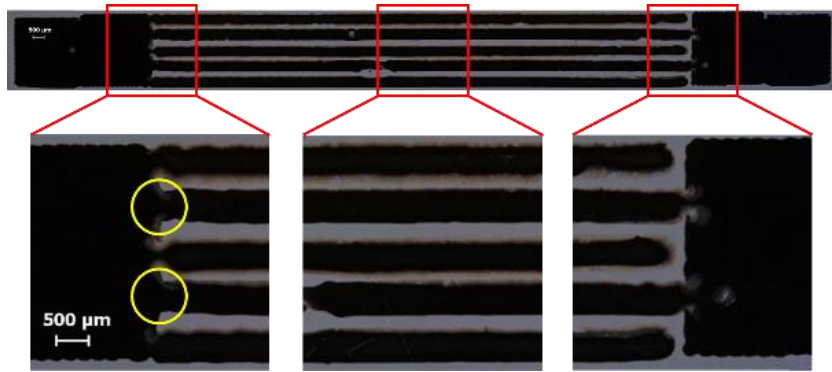


Figure 64 - Example of printed sample with interconnected arrays ( $\Delta x = 80 \mu\text{m}$ ,  $\Delta y = 110 \mu\text{m}$ ,  $v_p = 10 \text{ mm/s}$ ,  $T_n = 40^\circ\text{C}$ )

Figure 65 depicts the experimental results in terms of minimum value of the gap. It should be noticed that the majority of the experimental conditions with  $\Delta x = 80 \mu\text{m}$  resulted in a value of  $min_{gap}$  equal to zero (red diamonds in Figure 65), meaning that the arrays are interconnected, as shown by yellow circles in Figure 64, corrupting the geometry shape. Thus, all the process parameter combinations including  $\Delta x = 80 \mu\text{m}$  are likely to be unsuitable.

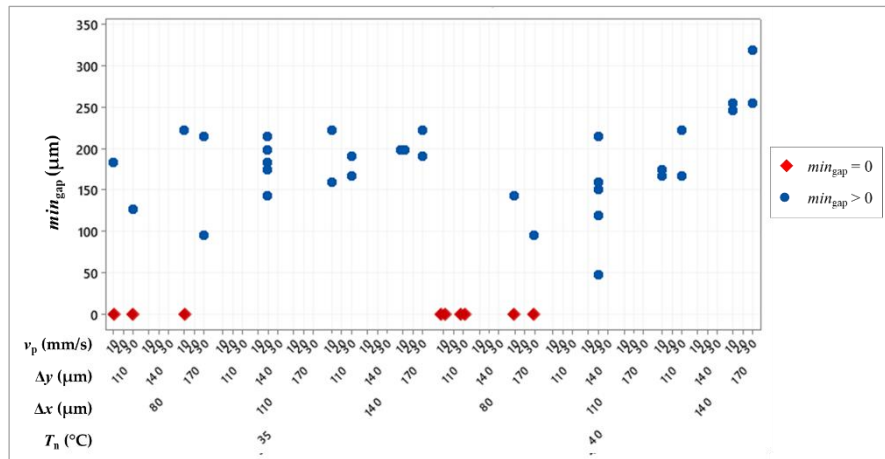


Figure 65 - Individual value plot of the minimum value of the gap

Figure 66 shows the gap length that was measured for the samples that do not present interconnections. A gap length that is much lower than the nominal value (red diamonds in Figure 66) implies that there are disconnections at the beginning of an array (Figure 67a). A gap length that is slightly lower than the nominal value (green squares in Figure 66) means that there is a disconnection at some intermediate point of an array (Figure 67b). The experimental data do not

exhibit clear relationships between the process parameters and the disconnections, which are likely to be caused by random issues, such as dust or ink-substrate anomalous interaction, due to substrate defects or ink aggregates.

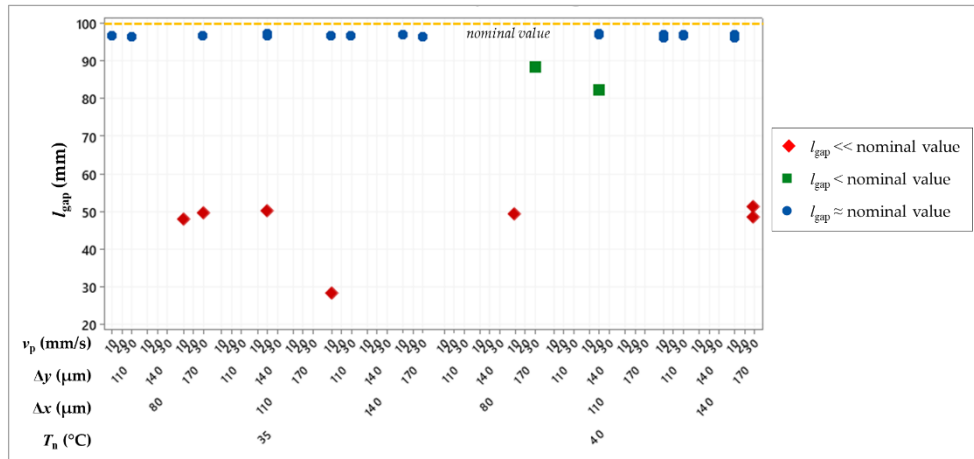


Figure 66 - Individual value plot of gap length

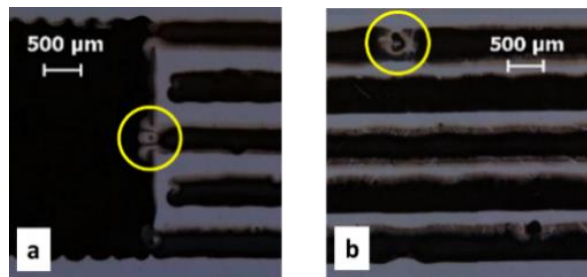


Figure 67 - a) Example of disconnection at the array beginning ( $\Delta x = 140$  mm,  $\Delta y = 170$  mm,  $v_p = 30$  mm/s,  $T_n = 35^\circ\text{C}$ ); b) Example of intermediate disconnection ( $\Delta x = 110$  mm,  $\Delta y = 140$  mm,  $v_p = 20$  mm/s,  $T_n = 40^\circ\text{C}$ )

## 4.6 Conclusions

This study investigated the application of the DoD inkjet printing technology to the manufacturing of a micrometer-scaled representative geometry, i.e. the so-called interdigital geometry consisting of two interlocked comb shapes. A suitable experimental design was studied to assess the influence of the spacing between subsequent drops, the printing speed and the nozzle temperature on the process output, which are defined as the minimum value, the mean value, the standard deviation and the total length of the gap between the two interdigitated shapes, as shown in Figure 53.

Matlab code executing image processing functions aiming to quantitatively assess the geometrical dimensions of the printed shapes revealed as an effective tool. The defined experimental output,  $\mu_{\text{gap}}$ ,  $\sigma_{\text{gap}}$ ,  $min_{\text{gap}}$  and  $l_{\text{gap}}$  are evaluated for each experimental condition, feeding the successive data analysis.

Two levels for the design factors, i.e.  $\Delta x$ ,  $\Delta y$ ,  $v_p$ ,  $T_n$ , were defined according to a preliminary empirical approach. A fixed effect model was used to observe the responses of the designed factorial experimental plan. ANOVA procedure was used to evaluate the statistical relevance on  $\mu_{\text{gap}}$  and  $\sigma_{\text{gap}}$  of the selected factors.

The ANOVA results highlighted that  $\Delta x$ ,  $\Delta y$ ,  $T_n$  are the most relevant factors on gap mean value and standard deviation calculation.

The experimental results showed that the drop spacing along both the x-axis and the y-axis have an influence on the width and the regularity of the gap between the arrays. The increase of these two factors led to a mean value closer to the nominal value and a progressive reduction of the standard deviation, as shown in Figure 60 and Figure 61.

Moreover, the results pointed out that the nozzle temperature affects the gap mean value. It was proved by Figure 63 that the mean size of the gap decreases as  $T_n$  increase, while the gap standard deviation did not exhibit significant variations.

The ANOVA did not highlight the printing speed as significant for the statistic. Figure 62 shown that there are not evident trends relating this factor to the gap mean value and standard deviation. In can be deduced that the tested printing speeds lies in an acceptable speed range, hence not causing high machine vibrations or droplet instability, as mentioned in 4.1 .

The spacing along the printing direction (x-axis) proved to be critical for avoiding interconnections between the arrays, since the majority of samples having  $\Delta x = 80 \mu\text{m}$  resulted in comb interconnections, as shown by the  $min_{\text{gap}}$  in Figure 65. Therefore, such drop spacing along the x direction is excluded for an optimal printing achievement.

No evident correlations between any factor and gap length were founded. Eventually, the process output was also influenced by issues related to substrate damages or dust fibers, as shown in Figure 67. Therefore, performing the experimental campaign in a controlled environment could limit these issues.

This work allowed to create a repeatable methodology for assessing the relationships between geometrical quantities and printing parameters, which can be extended to other ink-substrate couples.

The developed analysis tools could also be used in a quality check procedure for batch produced inkjet printed shapes.

# **Chapter 5. PEEK based EADs: manufacturing and characterization**

## **5.1 Introduction**

After having introduced the technology of ink-jet printing in Chapter 3. , this chapter presents a practical application of such additive manufacturing technique for the preparation of electro adhesive devices.

Hereafter are presented two namely identical EADs designed with coplanar interdigitated inkjet printed electrodes (Figure 68b depicts the top view of the electrode geometry), encapsulated by two dielectric layers, as schematically shown by the device cross section in Figure 68a.

The EADs design is presented first, describing the geometry of the electrodes, the production process, and the deployed materials constituting the devices, along with the assembling of device components. Electrodes are inkjet printed onto a 25  $\mu\text{m}$  PEEK film, acting as “adhering surface”, and a 300  $\mu\text{m}$  blade casted PDMS layer acts as the “backing”, referring to Figure 68a nomenclature.

After specimens’ completion, the adopted manufacturing process was verified by measuring EADs capacitance, assessing the repeatability of the procedure, and the consistency between the two produced specimens.

The experimental set-up is described afterward, representing the first test bench prototype developed in the laboratory. The set-up is used for traction tests evaluating the shear adhesive force exerted by the produced EADs. In particular, the electro-adhesive shear stress (ESS) is evaluated for both samples while adhering to an aluminized Polyimide film from the aluminized side when samples are subjected to a DC voltage signal. This kind of test not only provides a rough idea of the performances of such kind of EADs but also exploit the potentiality of this class of actuators on adhering to electrical conductors.

Finally, the characterization results are described, focused on an early assessment of EADs performance in terms of ESS, response time, and energy/power consumptions during one cycle of operation.

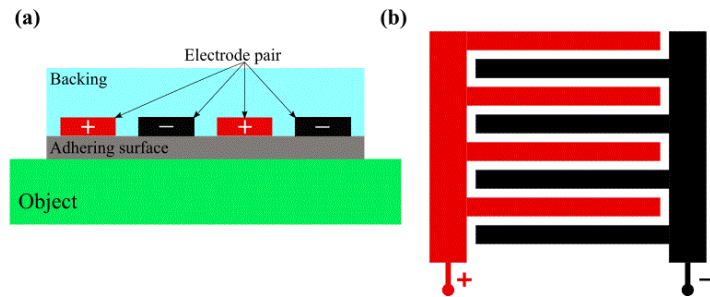


Figure 68 - Schematic of an Electro-adhesive device (EAD) with interdigitated electrode pattern: (a) cross-section and (b) a partial top view.

## 5.2 EAD specimen preparation

This section describes the manufacturing process adopted for the realization of two nominally identical EADs, each featuring an adhering substrate made of a commercial PEEK film, silver electrodes deposited via inkjet printing and a backing insulation layer made of a blade casted silicone elastomer. The manufacturing of the specimens was performed in non-controlled environment.

### 5.2.1 Electrode design

The EAD specimens manufactured and investigated in this work feature interdigitated electrodes. This pattern has been chosen since it should provide relatively better ESS performances compared to other basic geometries [31], [38], [93]. A top-view picture of one of the manufactured EAD specimens showing the printed electrode pattern is reported in Figure 69. Nominal electrode gap and width are respectively chosen as:  $g = 250 \mu\text{m}$  and  $w = 400 \mu\text{m}$ . These values are the minimal that could be manufactured with the employed inkjet printer, silver nanoparticle ink and PEEK substrate. The total pattern occupies an area of  $9.6 \text{ cm}^2$ , with length  $L = 40 \text{ mm}$  and width  $W = 24 \text{ mm}$ .

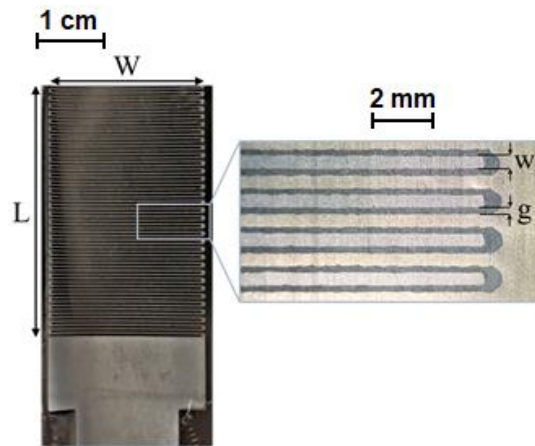


Figure 69 - Top view of the manufactured EAD with a detail of the printed electrodes

### 5.2.2 Electrode patterning

A dielectric film (PEEK, RS Components, product number 764-8719) featuring a nominal thickness of 25  $\mu\text{m}$  is chosen as the substrate for the patterning of the electrode pair due to the ease of availability, a large nominal dielectric strength (190 MV/m) in addition to a high maximum operating temperature (200  $^{\circ}\text{C}$ ) that is compatible with the sintering temperature of the adopted silver nanoparticle ink (120-150  $^{\circ}\text{C}$ ). This PEEK film also performs as the adhering substrate of the EAD which comes into contact with the adhered object.

The drop-on-demand inkjet printer MicroFab Jetlab<sup>®</sup> 4xl equipped with a piezoelectric nozzle of diameter 50  $\mu\text{m}$  (MJ-AT-01) Jetlab<sup>®</sup> 4xl, described in 3.3 , is used for electrode patterning.

The commercial silver nanoparticle ink DGP 40LT-15C by Anapro is chosen as the electrode material. This ink, which has been conceived to be directly ink-jettable without the need of adding solvents, is characterized by good compatibility with plastic film substrates, low resistivity (in the range 11-12  $\mu\Omega\cdot\text{cm}$ ) and intermediate curing temperatures (in the range 120-150  $^{\circ}\text{C}$ ).

The ink is jetted with a monopolar trapezoidal voltage waveform (3.2.2 ) having rise and fall times equal to 3  $\mu\text{s}$ , dwell time of 33  $\mu\text{s}$ , and well voltage equal to 38 V. Some examples of such printing conditions are presented in 3.5.1.2.

Before ink deposition, the PEEK film is cleaned with dry cleanroom paper. Cleaning with solvents is avoided here as it may lead to unstable wetting of the film by the ink droplets, which typically leads to low quality of the print. The PEEK film is then placed onto the printing platen of Jetlab<sup>®</sup> 4xl. The platen is kept at 50  $^{\circ}\text{C}$  for fast evaporation of ink solvents when the droplet reaches the PEEK film. At the completion of the print, the PEEK film is transferred in an oven and cured for 45 minutes at 120  $^{\circ}\text{C}$  to enable the sintering of the silver nanoparticles.

### 5.2.3 Backing layer fabrication

The backing layer is a mandatory component for EADs, which is used to encapsulate the electrode pair and protect it from electrical breakdown. A commercial two-component liquid silicone elastomer (Wacker Silpuran® 6000/05) is chosen as the main material to achieve a flexible EAD. An automatic thin-film deposition system with vacuum bed and micrometer adjustable blade applicator (TQC Sheen AB3655 and VF1823) is used for casting the selected silicone elastomer onto the PEEK film on the side where the electrode pair has been printed. Prior to casting:

- A mixture of Silpuran® 6000/05 components (A and B) is made with the addition of a solvent (Dow DOWSIL™ OS-2), which is done to lower the viscosity of the compound. The mixture has a weight ratio of 5:5:8 (A:B:solvent). In particular, the mixture is homogenized in a planetary-centrifugal mixer (Thinky ARE-250) for 2 minutes at 2000 rpm and then degassed for another 2 minutes at 2000 rpm. The degassing phase is essential to avoid entrapment of air bubbles into the backing layer, which may lead to premature breakdown of the EAD;
- The printed surface of the PEEK film is treated with a primer (Dow DOWSIL™ 1200 OS Primer), which is done to increase the bonding strength between the silicone elastomer layer and the PEEK film. In particular, a thin layer of the primer is manually applied on the electrode area via a clean swab with lint-free foam pad. The primer is then left curing for 15 minutes in free air.

Casting is then performed with the blade adjusted at a height of 700  $\mu\text{m}$  and with the applicator speed set to 1 mm/s. The casted silicone layer is then vulcanized in oven for 30 minutes at 85 °C. The curing temperature is lower than those suggested in the datasheet (160 °C for press-molding and 200 °C for post-curing) to prevent the generation of voids that may be caused by fast solvent evaporation. The finalized backing layer has a thickness of around 290  $\mu\text{m}$ , corresponding to a thickness reduction of around 60% with respect to the original thickness of the blade-casted mixture.

## 5.3 Testing set-up and procedure

This section describes the experimental set-up and procedures that have been used for the electro-mechanical characterization of two nominally identical EADs that have been manufactured according to the process detailed in Section 2. In these tests, an aluminized PI Film (Caplinq PIT1N-ALUM, with 25  $\mu\text{m}$  PI thickness and 0.1  $\mu\text{m}$  sputtered aluminum coating) is used as the adhering material, with the contact between EAD and PI film occurring on the aluminized side.



### 5.3.1 Capacitance measurement

Before measuring ESS performance, the capacitance values of the two specimens are measured with a LCR meter (Rohde & Schwarz HM8118) at 20Hz. The capacitance is evaluated under two different conditions: with the specimen in free air; with the Aluminized PI film residing on top of the specimen under a homogeneous pressure of around 400 Pa, which reproduces the condition during the ESS measurement with no electrical activation.

### 5.3.2 Experimental setup for ESS measurement

A schematic view and the real arrangement of the experimental setup for ESS measurement are depicted respectively in Figure 70 ,and Figure 71. The considered layout attempts to replicate the one suggested in the ISO 8295 standard [22] for the determination of the friction coefficient in plastic thin films. In the set-up, the EAD is kept fixed to the frame with the adhering surface layer facing upwards.

The aluminized PI film is then placed on top of the EAD with a homogeneous pressure of around 400 Pa (generated via a 42 g weight, which works as the sled in ISO 8295 standard). The aluminized PI film is constrained to a moving stage and can be moved parallel and on same level of the mating surfaces. The motion stage is equipped with a loadcell (NS-WL1-10Kg) which allows the acquisition of shear force values.

ESS is then obtained by dividing the measured peak shear force by the total area of the EAD. The EAD is energized by a high voltage power supply (ULTRAVOLT 20HVA24-BPL), which also enables monitoring of the voltage and current delivered to the EAD.

Monitoring and control signals are managed and acquired by a Beckhoff real-time controller (CX5140-0125) with I/O modules (EL3356, for interfacing loadcell; EL3104, for analog input; EL4732, for analog output) under TwinCAT 3 control software environment. The signal sampling rate is chosen as 1 kHz.

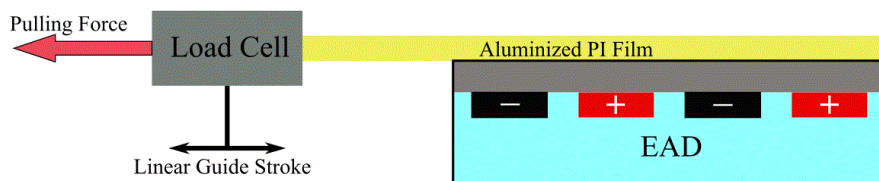


Figure 70 - Schematic of the test arrangement for ESS measurement

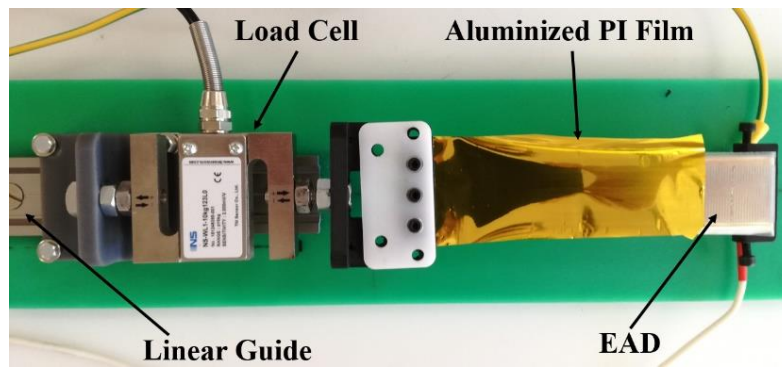


Figure 71 - A real picture showing the top-view of the test arrangement for ESS measurement

### 5.3.3 Testing procedure for ESS measurement

To ensure a dry and grease-free contact between adhered object and device, the EAD adhering surface is cleaned with isopropanol and left dried before each test. The Aluminized PI film is then placed on top of the EAD, with wrinkles removed manually before placing the 42 g weight. Measurement is conducted with the EAD powered under DC step voltage. After electrical activation, the aluminized PI film is pulled away manually through the moving stage and the peak resulting shear force is acquired. Tests are performed for different voltage step amplitudes, increasing from 0 kV to breakdown with 1kV increments. For each voltage level, the trial is replicated three times to examine the repeatability of the measurement. After each trial, the EAD adhering surface is discharged from residual charges using a grounded aluminized PI film.

## 5.4 Experimental results

This section reports the results of capacitance and ESS measurements attained on the two EAD specimens manufactured according to 5.2 and tested with the set-ups described in 5.3 . Experimental data on the time evolution of supplied voltage and current, as well as of applied force during one cycle of EAD activation are also provided to investigate response time and energy/power consumption.

### 5.4.1 EAD capacitance

The capacitances ( $C_p$ ) of the two manufactured EADs measured both in free air and in contact to the aluminized PI film are reported in Table 8. As it can be seen, for the same test cases, the capacitances of the two specimens have approximately same values, which reflects the repeatability of the fabrication process to some extent. The significant increase in capacitance due to the contact with aluminized PI film is foreseeable: the aluminized PI film provides additional free charges to be

attracted around the electrode area. This intrinsic effect provides a self-sensing capability of EADs, which can be exploited to detect the contact of the device with an object to be grasped.

	<i>C<sub>p</sub> in Air</i>	<i>C<sub>p</sub> on Aluminized PI</i>
<i>Sample 1</i>	39 pF	95 pF
<i>Sample 2</i>	41 pF	96 pF

Table 8 - Measured capacitance values of the two tested samples when in free air and in contact with the aluminized PI film

#### 5.4.2 Shear stress measurements on aluminized PI film

The evolution of the measured ESS versus the voltages applied across the EAD electrode pairs is shown in Figure 72, showing the mean value of the ESS obtained by following the procedure described in 5.3.3 for the two nominally identical manufactured EAD specimens. Results highlight the following:

- The maximum achieved ESS on aluminized PI film for the considered PEEK-based EADs manufactured via proposed fabrication process is around 40 kPa;
- Although capacitance characteristics are similar, the shear stress performance of the two EADs are different. In particular, the ESS value of Sample 2 exhibits an early saturation at around 5kV, whereas the EES value of Sample 1 increases with the applied voltage till breakdown occurs. This may be caused by small local imperfections in the printed electrodes, such as the wavy edges with ripple in the range of 10-20 μm shown in Figure 69, whose effects on the global EAD performance becomes apparent only at high fields.
- Irrespective of the dissimilar ESS performance at high field, the break-down occurred at 8 kV for both EAD samples, indicating some potential consistency of the overall manufacturing process.
- The shear stress at 0kV, i.e. the friction stresses, is negligible compared to the ESS measured with applied voltage above 2kV. This means that the measured shear stress is mainly triggered by the applied voltage and due to the electro-adhesive effect;
- Compared to the drastic increase in ESS from 0kV to 2kV, the increase after 2kV till breakdown/saturation is closer to a linear trend rather than to a quadratic relation as one would expect from theory [1], [6], [16], [17].

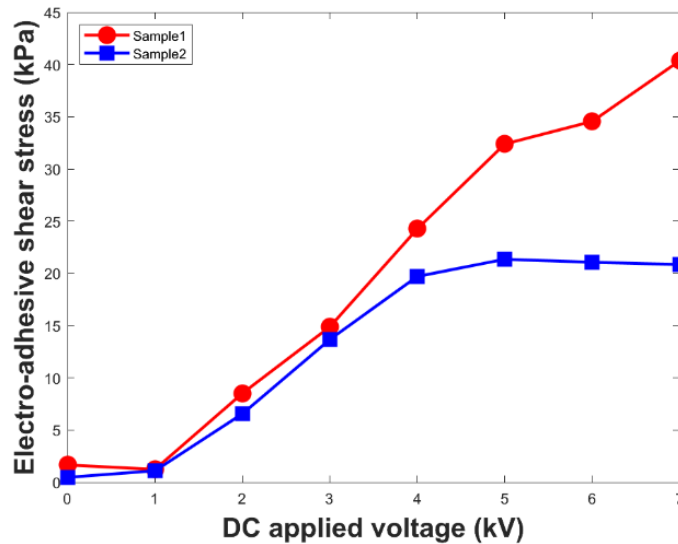


Figure 72 - ESS vs. applied voltage for Sample 1 and Sample 2, tested on aluminized PI film from 0V till specimen breakdown.

### 5.4.3 Inspection on system time response and energy-power consumption

Figure 73 reports the time evolution of the most significant variables measured on one of the manufactured EAD specimens recorded over one cycle of operation (charging, grasping and discharging) during the ESS tests performed with an electrical activation of 7 kV.

In particular: Figure 73a shows the applied voltage and the corresponding current across the EAD; Figure 73b shows the power and energy consumed by the EAD; Figure 73c shows the shear force measured by the load-cell of the set-up pictured in Figure 71.

One cycle of operation of the EAD that is composed by activation-holding-release consumed around 25 mJ. At 1.1 seconds during the charging phase, the current quickly increased till the 50  $\mu$ A saturation of the employed power supply. Hence the supplied power is also capped at 0.35W. A closer inspection at the charging phase (as shown in the zoom area in Figure 73a) reveals that the saturated current lasts for 0.02 seconds and then gradually decreases to nearly zero at 1.3 seconds. This whole process consumes around 17 mJ, which is far larger than what would be needed (around 2 mJ) to ideally charge the EAD based on the capacitance value reported in 5.4.1 .

After full EAD electrification, maintenance of the grasping requires about 1.5 mW to compensate for the current leakage that is due to the finite resistivity of the employed real dielectrics under high electric fields.

The detachment of the aluminized PI film from the EAD, which occurs at around 5.4 seconds, causes a current flow from the EAD to the power supply. The return of energy is likely due to the

sudden decrease in system capacitance, as the detachment between EAD and aluminized PI film introduces an additional intermediate layer.

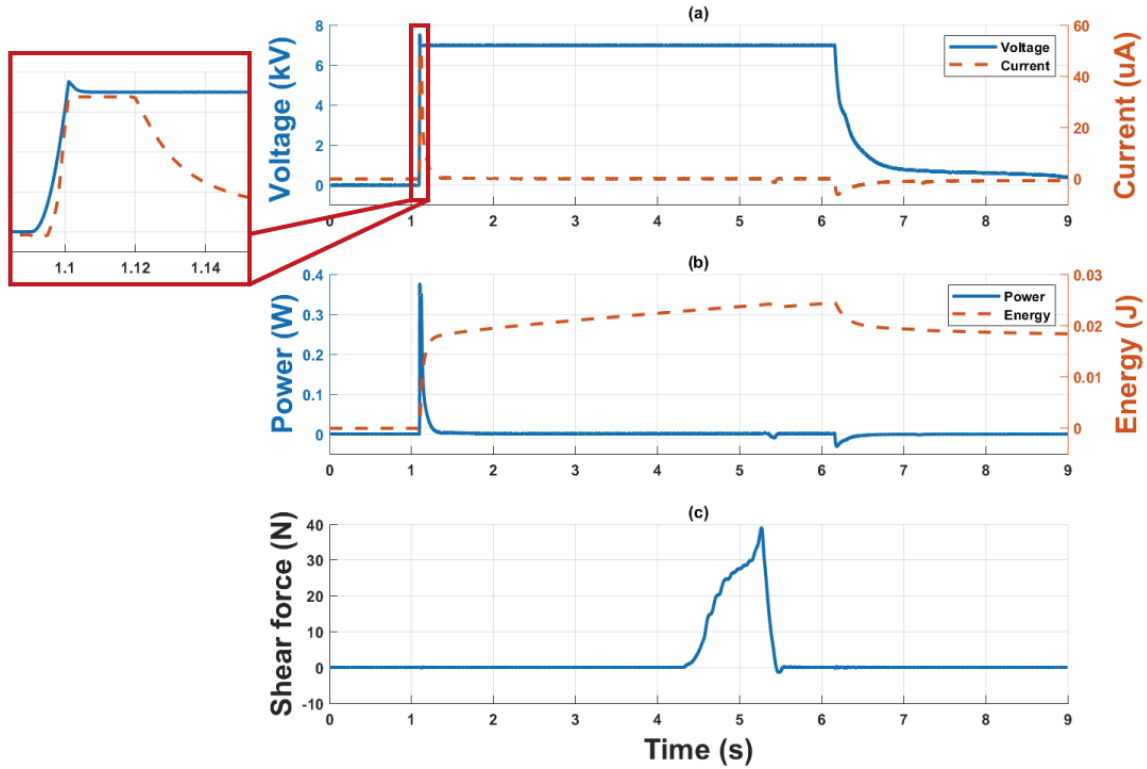


Figure 73 - Electro-mechanical response of one of the manufactured EAD specimens (Sample 1) during one cycle activation at 7kV for the grasping of the 25  $\mu\text{m}$  aluminized PI film. (a) voltage and current evolution, with a zoomed view of the transient; (b) power and energy evolution, estimated based on the voltage and current signals; (c) measured shear force.

## 5.5 Conclusions

This work reports on the fabrication and electro-mechanical testing of a thin and lightweight electro-adhesive gripper made of a commercial PEEK film as the main adhering substrate, inkjet-printed silver interdigitated electrodes and a blade-casted silicone elastomer backing encapsulation layer.

With an active area of  $9.6 \text{ cm}^2$ , a thickness of a  $300 \mu\text{m}$  and a weight of 0.7 g, the considered gripper is capable to generate an adhesion shear stress on an aluminized PI film that increases rather linearly with the device activation voltage, reaching a maximum of up to 40 kPa with an applied voltage of 7 kV.

Measurement of supply current and voltage highlights a fast system response, around 20 milliseconds for full device electrification, and a low energy consumption, around 17 mJ during one cycle of operation that comprises activation, grasp hold and release.

When entering in contact with the aluminized PI film, the gripper experiences a variation in capacitance higher than 150 %, whose measurement can be used to detect the presence of the object to be grasped.

Fabrication of one batch of three electro-adhesive grippers requires around two hours, with an additional 45 minutes for each additional batch up to a maximum of 8 lots. Besides being relatively fast and flexible, both in terms of usable materials and conceivable shapes, which makes it very suitable for the rapid manufacturing of thin-film flexible electro-adhesive grippers, the considered manufacturing process may also be scalable for medium and large production.

Relying on current and voltage measurements provided by the power supply monitoring signals, limits the observation of current and voltage to the nominal values of the power supply, as shown in the zoomed area of Figure 73a. Therefore, for a proper electrical characterization of tested EADs, a dedicated measurements circuitry will be deployed in future characterization works.

The deployed test bench exhibited appropriate characteristics for an early and coarse performance evaluation of EADs. However, being manually actuated and subjected to mechanical plays, a more robust, automated and reliable test bench is required for a more systematic mechanical characterization of the EADs. In next sections, a fully automatized test bench for ESS assessment will be presented, increasing test repeatability, and reducing experimental errors.

# **Chapter 6. PI based EADs: manufacturing, characterization, and application**

## **6.1 Introduction**

Adopting the production process presented and validated in Chapter 5. , this chapter deeply investigates performances of seven namely identical EADs on a variety of adhering materials. A step forward on EAD characterization and performance enhancement is carried out in this work by choosing a Polyimide (PI) film as the adhering surface. Being characterized by higher dielectric strength and dielectric constant compared to PEEK, PI exhibited more promising features in terms of ESS performances on a wider range of adhering materials.

The overall EAD structure resembles to the one proposed in Figure 68, having inkjet printed interdigitated silver electrodes encapsulated by two thin dielectric layers. A schematic of the presented devices, indicating also the deployed materials, is shown in Figure 74, which depicts the device cross section and the electrode partial top-view in Figure 74a and Figure 74b respectively.

Similarly to what was done in 5.3.3 ., an ESS performance evaluation from 0V to 5kV is carried out having specimens adhering to:

- 25  $\mu\text{m}$  PI film;
- 75  $\mu\text{m}$  PI film;
- Aluminized PI Film (with 25 $\mu\text{m}$  PI thickness and 0.1  $\mu\text{m}$  sputtered aluminum coating);
- 130 $\mu\text{m}$  PET film;
- 130 $\mu\text{m}$  Coated PET film;

Additionally, the maximum prehension performances of the developed EADs over the best performing tested materials is performed. ESSs of up to 56.67 kPa and 45.78 kPa are demonstrated respectively for coated polyethylene terephthalate (PET) and aluminized PI substrates,

As it was in Chapter 5. , capacitance consistency, response time analysis, and energy/power consumptions during one cycle of operation complete the characterization procedure.

In the final section, this chapter additionally provides one possible use of the produced EADs in a simple, though very effective and versatile, gripper for the handling of objects with different geometry and of different material.

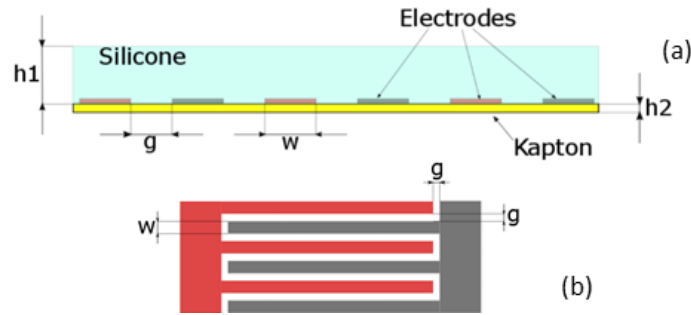


Figure 74 - Electro-Adhesive Device (EAD) cross-section (a) and electrode strip array partial front-view (b)

## 6.2 Design and Fabrication

In this work, EADs are manufactured by patterning the electrode pair via inkjet printing on a pre-fabricated dielectric film, made of Polyimide, and by using blade coating for the deposition of the backing electrode-encapsulation layer, made of PDMS.

The uni-layer design shown in Figure 74 is considered for a first demonstration of the proposed fabrication method and for the evaluation of the prehension performances attained by the manufactured EADs. With little modifications, this method could also be adapted for the fabrication of bi-layer architectures, as well as to realize a micro-structured contact surface.

Due to quick availability, ease of handling, adequate dielectric properties and mechanical flexibility, PI is chosen as the main dielectric layer and silicone elastomer is chosen for the backing. A silver ink for flexible electronics is used for the electrodes.

An exemplary EAD manufactured via the proposed method is shown in Figure 75. According to Figure 74 and Figure 75, the considered EAD geometry is the following: electrode width and gap,  $w = 400 \mu\text{m}$  and  $g = 300 \mu\text{m}$ ; main dielectric thickness,  $h_2 = 25.4 \mu\text{m}$ ; backing thickness,  $h_1 \approx 290 \mu\text{m}$ ; EAD active length and width,  $L = 24 \text{ mm}$  and  $H = 40 \text{ mm}$ ; EAD active area,  $A = L \times H = 9.6 \text{ cm}^2$ . With a thickness of around  $315 \mu\text{m}$  and a weight of  $0.7 \text{ g}$ , the manufactured EAD is very flexible, compact, and lightweight.



Manufacturing of the EAD depicted in Figure 75 requires about 112 minutes for a single device, plus a further 16 minutes per additional unit up to a maximum of 24 units that can be fabricated altogether.

A total of 7 nominally identical EAD specimens have been manufactured via the proposed method, which have then been subjected to testing as reported in 6.3 6.4 6.5 .

Specific details on employed materials and fabrication steps are given in the next subsections.

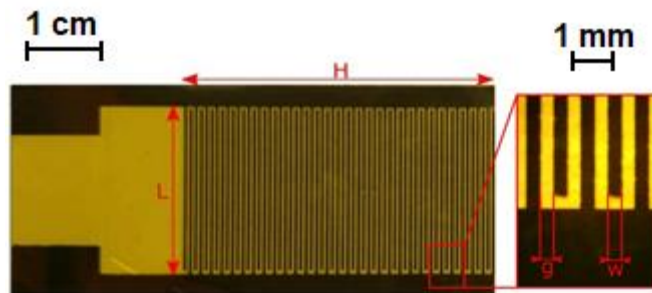


Figure 75 - EAD manufactured via ink-jet printing and blade coating: full device (on the left); detail of the inkjet printed electrode traces (on the right)

### 6.2.1 Main Dielectric Layer

A commercial PI film (Caplinq PIT1N/210) provided in rolls with a thickness of  $25.4 \mu\text{m}$  and a width of 210 mm is chosen as the main dielectric layer and as the printing substrate for electrode patterning. A pre-fabricated film has been preferred to a custom realization to guarantee the uniformity of substrate thickness and material properties, which is fundamental for the achievement of high and reliable performances that are consistent across all the manufactured EAD specimens. In terms of relevant material properties, the considered PI film features: a relative dielectric constant of 3.9; a dielectric strength of 236 MV/m; a volume resistivity of around  $1 \text{ M}\Omega\text{-cm}$ ; a continuous use temperature of up to  $260 \text{ }^\circ\text{C}$ .

### 6.2.2 Electrode Pair Fabrication

A drop-on-demand inkjet printer (MicroFab Jetlab® 4xl) with a  $50 \mu\text{m}$  diameter nozzle, described in 3.3 , is used for electrode pair deposition onto the PI film according to the desired pattern. A stable droplet formation was achieved by a monopolar trapezoidal voltage waveform. Machine settings and waveform parameters are reported in 3.5.1 and 3.5.1.1.

A commercial ink (Anapro DGP 40LT-15C), made with silver nanoparticles dispersed in a triethylene glycol monoethyl ether solvent, is used as electrode material due to its good compatibility

with plastic film substrates, low volume resistivity (around  $12 \mu\Omega\cdot\text{cm}$ ) and relatively low curing temperature (in the range  $120 \text{ }^\circ\text{C}$  and  $150 \text{ }^\circ\text{C}$ ).

The inner side of PI film roll is chosen as the printed surface. Prior to ink deposition, the PI film is cleaned with dry cleanroom paper to remove dust fibers. To reduce the mobility of dispensed ink droplets, thus to decrease the risks of defects in electrode pattern that may give rise to short circuits, the printing platen is kept at  $50 \text{ }^\circ\text{C}$  to facilitate solvent evaporation right after the droplets reach the PI film. Printing of the considered pattern takes about 16 minutes. Once printing is finished, the PI film is transferred in an oven, where it resides for about 45 minutes at  $120 \text{ }^\circ\text{C}$  to enable the sintering of the silver nanoparticles.

### **6.2.3 Backing Encapsulation Layer Fabrication**

An automatic thin-film deposition system with vacuum bed and micrometer adjustable blade applicator (TQC Sheen AB3655 and VF1823) is used for the casting of the backing encapsulation layer over the PI film on the side where the electrode pattern has been printed. This process has been selected due to its simplicity, speed and reliability.

A commercial two-component liquid silicone elastomer (Wacker Silpuran<sup>®</sup> 6000/05) is chosen as the main material.

A mixture of the two parts of the silicone elastomer (part A and part B) and a silicone solvent (Dow DOWSIL<sup>™</sup> OS-2) with a weight ratio of 5:5:8 is firstly prepared. The solution is homogenized in a planetary-centrifugal mixer (Thinky ARE-250) for 2 minutes at 2000 rpm and then defoamed for another 2 minutes at 2000 rpm. The defoaming step is fundamental to remove entrapped air bubbles in the mixture which could cause premature dielectric breakdown of the encapsulation layer and, thus, reduced the prehension performances of the manufactured EADs. Prior to solution deposition, the electroded PI film surface is treated with a primer (Dow DOWSIL<sup>™</sup> 1200 OS Primer) in order to improve both the quality and speed of adhesion between PI and silicone elastomer. Treatment is performed by manually applying a thin layer of primer through a clean stick with lint-free foam pad and then leaving it cured in air. This step requires about 15 minutes. Solution deposition is made with the automatic applicator with a blade height adjusted to  $700 \mu\text{m}$  to obtain a silicone layer of around  $290 \mu\text{m} \pm 10 \mu\text{m}$ , as a thickness reduction of around 60% occurs after solvent evaporation that is done in ambient conditions. Deposition with the automatic applicator requires about 2 minutes. As a last step, vulcanization of the deposited silicone elastomer is performed in an oven for 30 minutes at  $85 \text{ }^\circ\text{C}$ .

## 6.3 Experimental setup and test procedure

Quantitative validation of the manufactured EAD specimens is accomplished in terms of the ESS developed over different adhering objects at different levels of electric potential difference (voltage) applied to the electrode pair.

In order to assess the EAD performance in a reliable and replicable manner, the following commercial thin films, with controlled material properties and geometry, have been considered as adhering object/substrate samples:

- 25  $\mu\text{m}$  PI film (Caplinq PIT1N, inner side of roll);
- 75  $\mu\text{m}$  PI film (Caplinq PIT3N, inner side of roll);
- Aluminized PI Film (Caplinq PIT1N-ALUM, with 25 $\mu\text{m}$  PI thickness and 0.1  $\mu\text{m}$  sputtered aluminum coating, aluminum side);
- PET film (JetStar Standard Inkjet Film, with a thickness of 130 $\mu\text{m}$ , non-coated side);
- Coated PET film (JetStar Standard Inkjet Film, with a thickness of 130 $\mu\text{m}$ , coated side).

Beside evaluating the ESS-voltage relationships, the electrical properties and the time response of an EAD during an operation cycle are also investigated to provide an indication of the self-sensing capabilities of the device as well as its operational energy requirements.

### 6.3.1 Experimental Setup for ESS Measurement

Figure 76 and Figure 77 respectively show the schematic and real arrangement of the experimental setup conceived for ASS measurement.

In the setup, which resembles the apparatus described in the ISO 8295 standard [22] for the determination of the friction coefficient for plastic film and sheeting, the mating surfaces of EAD specimen and material sample are placed together in plane contact and under uniform contact pressure. The EAD specimen is kept fixed on a horizontal plane, whereas the material sample is attached to a sled that is constrained to move in the horizontal direction by a linear guide and equipped with a loadcell (NS-WL1-10kg) to enable measurement of the tangential force exchanged between the mating surfaces. Electrical activation of the EAD is performed with a high voltage supply (ULTRAVOLT® 40A24 or 20HVA24-bp1), which also enables to measure voltage and current across the EAD specimen. Control and data acquisition are performed at a sampling frequency of 1 kHz by a Beckhoff real-time controller (CX5140-0125 with I/O modules EL3356, EL3104, EL4732) under TwinCAT 3 environment.

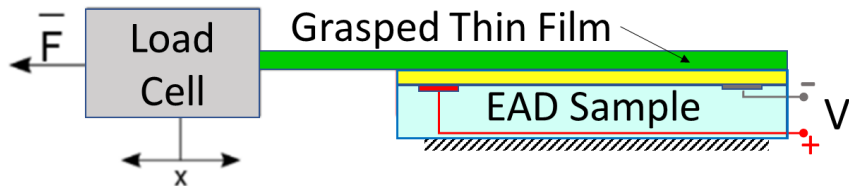


Figure 76 - Schematic of the test-bench employed for ASS measurement

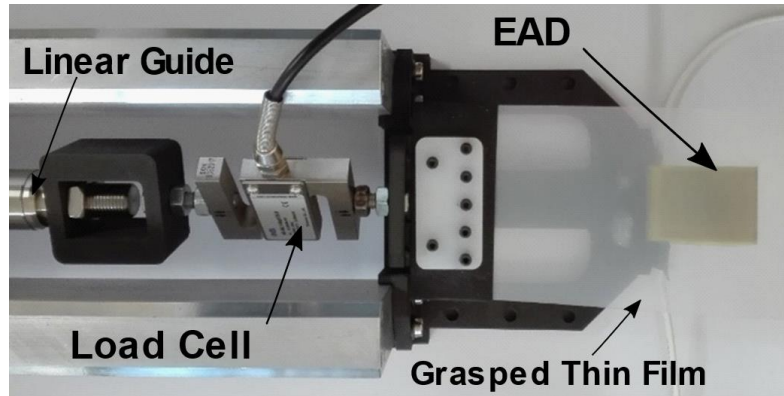


Figure 77 - Picture of the test-bench employed for ASS measurement

### 6.3.2 Testing procedure

Before executing ESS experiments, capacitance measurement of each of the seven EAD specimens is performed at 20 Hz with a LCR meter (Rohde & Schwarz HM8118). Besides providing an indication of the energy required for EAD operation, the variation in capacitance across different EAD specimens can be used to quantify the consistency of the procedure proposed here for their manufacturing.

For ESS measurement, first the material sample under test is manually placed over the EAD specimen. Second, to reduce the variability introduced by the human operator (in particular, the motion and force applied during mating surface alignment), a pre-load of 1 kg is applied above the testing area before electrical activation. After charging the EAD specimen to a desired voltage level, the pre-load is removed and a weight of 42 g is left on top of the testing area to provide a minimum normal contact pressure comparable to that suggested in the ISO 8295 standard [22]. Then, the thin film sample is pulled through the linear guide away from EAD specimen and the exchange shear force is recorded till slipping occurs. For each EAD specimen and material sample listed in 6.3 , tests are performed with DC voltage levels increasing from 0 kV to 5 kV with 1 kV step. Before testing a new EAD specimen or material sample, the contact surface is cleaned with propanol in order to remove dust and grease and then dried with cleanroom paper. After the discharging phase of each

test, any residual surface charge is removed from the mating surfaces of both EAD specimen and film sample with a grounded aluminized PI film.

To explore the performance limits of the manufactured EADs, additional ESS tests have also been conducted on two EAD specimens, one over the coated PET sample and one over the aluminized PI sample, with non-constant increasing voltage steps, gradually reducing after 5kV, till electrical breakdown of the EAD specimen.

Each ESS test is replicated three times, providing dataset able to validate experimental replicability.

## 6.4 Results

This section reports the results of the experiments conducted on the manufactured EAD specimens, following the testing procedure reported in 6.3.2 , and using the test bench described 6.3.1 .

### 6.4.1 EAD Capacitance

Table 9 shows the results of the capacitance measurements performed on seven nominally identical manufactured EAD specimens under the following conditions: exposed to free air, in contact to the coated PET sample, in contact to the aluminized PI sample.

The limited value of the standard deviation (SD), especially for the free-air case, indicates that the proposed fabrication procedure can be considered repeatable. The relative increase in the SD value when the EAD is in contact with an adhering object may be due to entrapped air between the mating surfaces, as this influences the effective capacitance of the system made by EAD specimen and film sample.

The significant increase in the mean value of capacitance when the EAD is in contact to an adhering substrate (a 2.4 increase for coated PET and a 3.6 increase for aluminized PI with respect to the free-air case) indicates that the EAD features an intrinsic self-sensing ability that can be exploited to detect contact with a neighbor object.

EAD CAPACITANCE			
	<i>in Free Air</i>	<i>on Coated PET</i>	<i>on Aluminized PI</i>
MEAN (PF)	28.8	70.7	105.67
SD (PF)	1.04	5.54	7.37
SD/MEAN (%)	3.61	7.83	6.97

Table 9 - Measured Capacitance Of The Manufactured EAD Specimens: Mean And Standard Deviation (SD) Values Evaluated For Neven Nominally Identical EAD Specimens.

## 6.4.2 Electro-adhesive Shear Stress (ESS)

Figure 78 summarizes the measured ESS results obtained on the seven manufactured EAD specimens, over the five different adhering film samples, for different EAD activation voltages. The error bars are the standard deviation of the measured ESS among different EAD specimens. Results highlight a significant increase in ESS with applied voltage, with the increase being more than linear and depending on substrate material and thickness.

For all activation levels, the highest ESS values are obtained for coated PET and aluminized PI. The thin PI film seems to adhere better than its thicker counterpart. The ESS values reported here are among the highest attained in the literature; in particular: one order of magnitude better than those recorded for existing EADs with a similar PI main dielectric layer [23], [37], [39], [40]; comparable to those recorded for existing EADs with a silicone elastomer main dielectric layer [8], [36], which is known to have a higher interfacial friction (and adhesion at no voltage) than PI on the considered film samples. Figure 78b highlights the low pressure generated by the pure friction component, which empathizes the adhesive effect due to electro adhesion, rather than to the pure friction force.

To assess maximum ESS performance, additional tests on coated PET and aluminized PI samples have been conducted with the activation voltage increasing from 1 kV till EAD rupture due to dielectric breakdown, which occurred in the backing silicone layer respectively at 8.3 kV and 7.6 kV. Results are reported in Figure 79, which shows a saturation of the measured ESS for both the adhering substrates. Measured peak ESS values are 45.78 kPa at 6 kV for Aluminized PI and 56.67 kPa at 7 kV for coated PET, which are very promising values, especially considering that the recorded saturation may leave space for improvement.

A closer examination on the considered EAD specimens indeed revealed that some electrode traces have been burnt away for activation voltages higher than 6 kV. Although these burnt-away electrodes did not short-circuit the EAD specimen before its global breakdown, they might have compromised its prehension performance, as represented by the plateau.

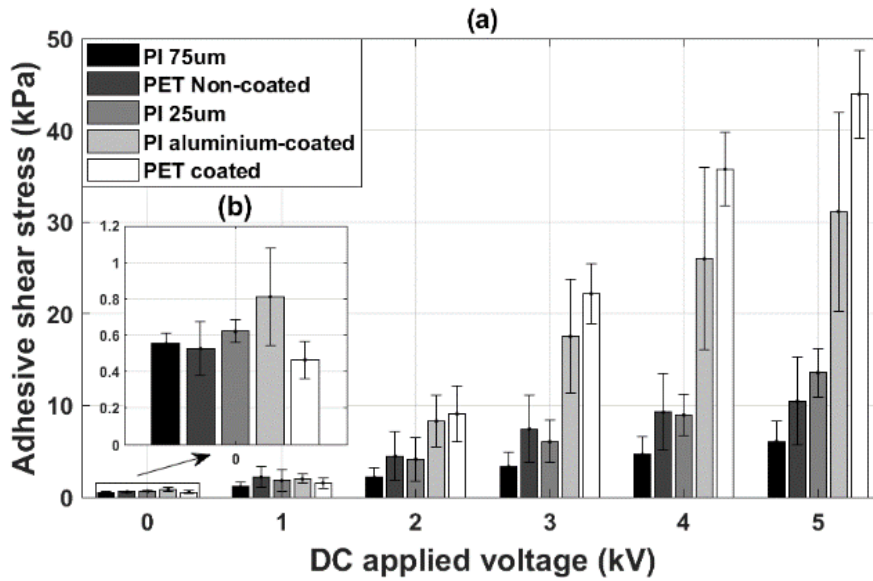


Figure 78 - Measured adhesion shear stress (ASS): mean (column) and standard deviation (error bar) values evaluated for seven nominally identical manufactured EAD specimens. (a) ASS vs EAD activation voltage for different film samples. (b) zoom for the case with no voltage applied

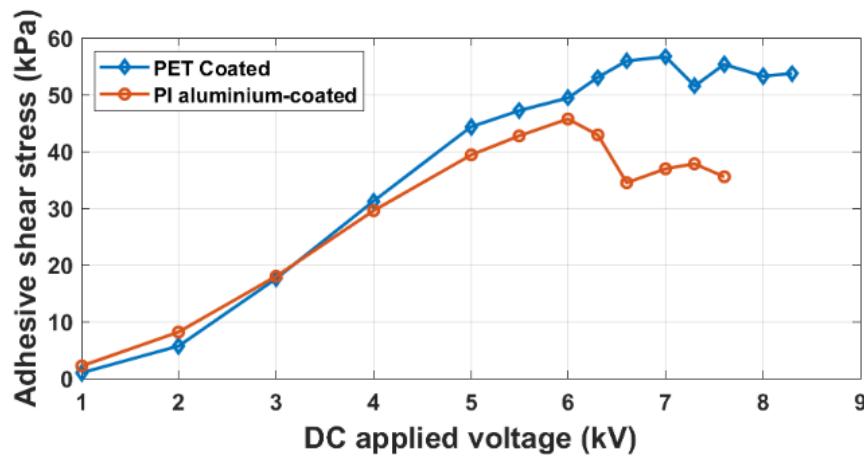


Figure 79 - Adhesion shear stress (ASS) vs applied voltage for coated PET and aluminized PI till EAD specimen breakdown

### 6.4.3 Energy and Power Consumptions

Figure 80 reports the full status of one of the manufactured EAD specimens over one cycle of operation during the ESS tests when grasping the aluminized PI substrate at 5kV. In particular: Figure 80a shows the evolution of the voltage applied between the EAD electrodes and the current flowing through them; Figure 80b shows the power and energy supplied to the EAD; Figure 80c shows the shear force measured by the loadcell when the EAD is pulled away from the tested substrate (which is done around 4 seconds after the electrical activation) in the setup of Figure 76 and Figure 77.

As the employed power supply (Ultravolt 20HVA24-bp1) has a rated current of 50  $\mu$ A, the current immediately saturates during charging, which occurs at 0.4s; this also limits the maximum power absorbed by the EAD specimen below 0.27 W. Despite the initial electrical activation of the EAD requires about 11 ms and 1.3 mJ, which are consistent with the capacitance values reported in Table 9, a significant amount of current needs to be supplied for about 0.3 s and with an energy expenditure of about 20 mJ for proper material electrification (namely, for the current to settle after the asymptotic decay shown in Figure 80a due to dielectric absorption and sweep of mobile ions to the electrodes). After full EAD electrification, maintenance of the grasping requires about 1 mW to compensate for the current leakage that is due to the finite resistivity of the employed real dielectrics. Although barely visible, the loss of grasp that occurs around 4.7 s causes a current flow from the EAD to the power supply with a little return of energy.

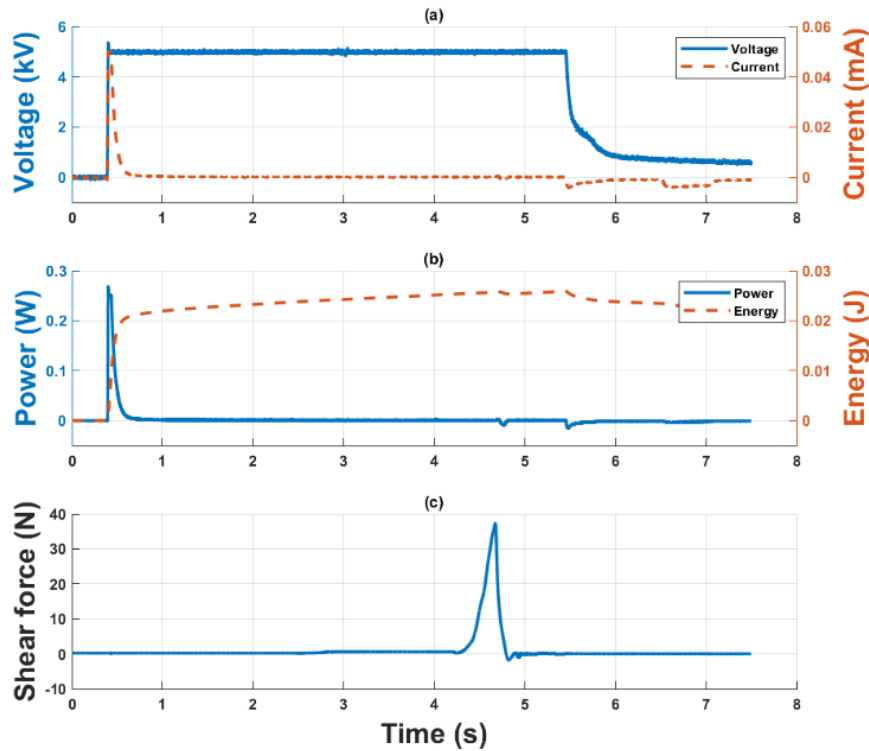


Figure 80 - Status of EAD during one cycle of charging and discharging: (a) voltage and current history from power supply monitoring signals; (b) estimated power and energy history; (c) force history from loadcell signal.

## 6.5 Gripper Application

To validate the manufactured EAD specimens in the manipulation of practical objects, a simple gripper made with two opposite hanging EADs has been realized.



Gripper embodiment along with demonstration of its ability in the grasping of a glass bottle is demonstrated in Figure 81. In particular, Figure 81b-e show the capability of the manufactured flexible EADs to automatically close around the object to be grasped (in this case a glass bottle) upon electrical activation by using the same electrostatic attraction pressure that generates the retention action. In fact, if the EAD and the object touch in some location (as shown in Figure 81b and Figure 81c), electrical activation provides a zipping action that makes the EAD flex and lay down on the object surface (as shown in Figure 81d and Figure 81e) so as to maximize the combined EAD-object capacitance.

Figure 82 demonstrate instead the ability of the same gripper in the handling of different objects; in particular: a glass bottle filled with water having a weight of 500 g (Figure 82a and Figure 82b); a hollow carbon fiber tube having a weight of 159 g (Figure 82c); a cardboard box with a weight of 41 g (Figure 82d); a box with a thin PP envelop with a weight of 211 g (Figure 82e); a PP bottle partially filled with propanol having a weight of 52 g (Figure 82f).

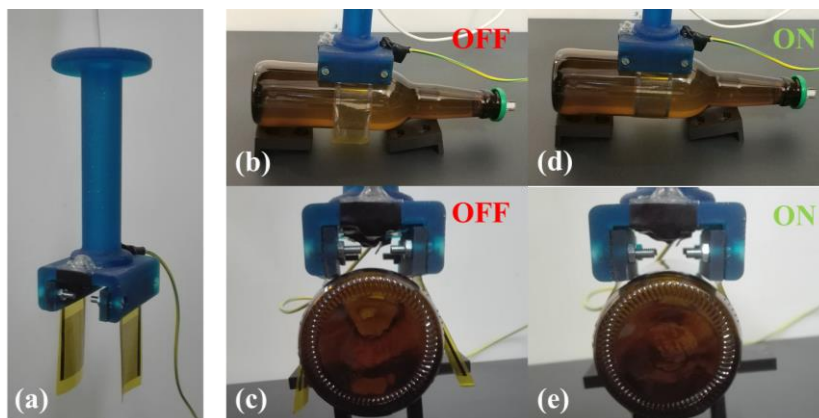


Figure 81 - Simple robotic gripper made with two opposite hanging EADs and its use for the grasping of a glass bottle: (a) gripper embodiment; (b) gripper open under no voltage, lateral view; (c) gripper open under no voltage, axial view; (d) gripper closed after electrical activation, lateral view; (e) gripper closed after electrical activation, axial view.

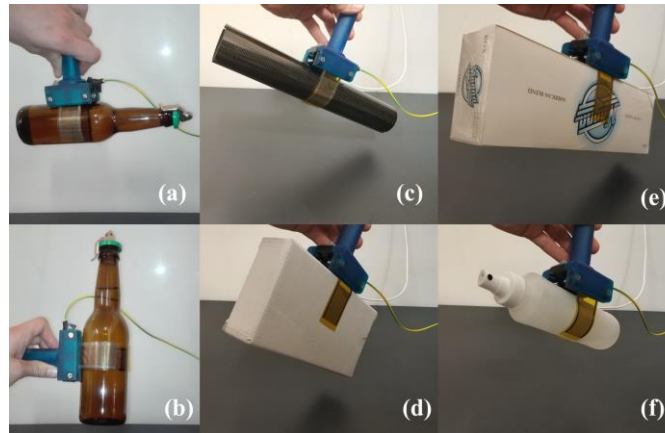


Figure 82 - Simple robotic gripper made with two opposite hanging EADs while handling different objects: (a) a water-filled glass bottle lying horizontal; (b) a water-filled glass bottle lying vertical; (c) a carbon fiber tube; (d) a cardboard box; (e) a box with PP envelop; (f) a propanol-filled plastic bottle

## 6.6 Conclusions

In this work, a procedure based on inkjet printing and blade coating has been proposed for the fabrication of 315  $\mu\text{m}$  thick electro-adhesive devices (EADs) having a polyimide main dielectric layer, silver interdigitated electrodes and silicone elastomer backing.

Requiring about 112 minutes for the production of a single EAD with an active area of 9.6  $\text{cm}^2$ , plus a further 16 minutes per additional device up to a maximum of 24 units, the proposed procedure is suitable for the rapid prototyping and on-demand manufacturing of thin-film flexible EADs, and even scalable for large production.

Seven nominally identical EAD specimens have been manufactured with the proposed procedure and then subjected to electrical and mechanical testing.

Capacitance measurements showed a small relative standard deviation, indicating that the proposed fabrication procedure can be considered very reliable, and a significant dependence on the adhering substrate material, evidencing the inherent ability of EADs in sensing the presence of an adjacent object.

Tangential force tests demonstrated the capability of the manufactured EAD specimens to adhere well to different substrates, though with performances depending on object material and thickness. In particular, the following maximum adhesion shear stresses have been recorded for the EADs operated with an activation voltage of 5kV:

- 48.68 kPa on coated polyethylene terephthalate film;
- 41.99 kPa on an aluminized polyimide film;
- 16.21 kPa on a 25  $\mu\text{m}$  polyimide film;

- 15.24 kPa on a non-coated polyethylene terephthalate film;
- 8.31 kPa on a 75  $\mu\text{m}$  polyimide film.

Moreover, peak shear stresses of 56.67 kPa and 45.78 kPa have been achieved for coated polyethylene terephthalate film at 8.3 kV and aluminized polyimide film at 7.6 kV. These values are among the highest reported in the literature for similar EAD and adhering substrate materials. For all tested substrates, adhesion shear stress increased with EAD activation voltage, without globally following the theoretical quadratic law, and showed a significant saturation for activation voltages higher than 6 kV.

Electrical measurement during EAD operation with a 50  $\mu\text{A}$  limited power supply highlighted fast response time, 11 ms for initial activation and 0.3 s for full electrification, and small energy consumption, from 1.3 mJ for initial activation to 20 mJ for full electrification with a subsequent power consumption of about 1 mW for long-term grasp holding.

To validate the practical effectiveness of the proposed rapid fabrication approach and of the manufactured specimens, a simple gripper with a parallel pair of free hanging EADs has been constructed and successfully tested for the grabbing and handling of a variety of objects, including: a glass bottle completely filled with water, a hollow carbon fiber tube, a cardboard box, a box with thin polypropylene envelope and a polypropylene bottle partially filled with propanol.

Beside the capability of lifting and tilting the objects, these tests also demonstrated the efficacy of the electrostatic attraction principle in actuating the flexible EADs within a limited range to make them approach the object and optimally conform to its surface prior to grasping.

Chapter 5. , as well as Chapter 6. , mainly focused on the ESS performances and on EADs practical applications, thus providing only a coarse electrical characterization. Indeed, the deployed test bench still lacks dedicated current and voltage measurements circuitries. As mentioned in 5.4.3, the delivered current was limited to the rated current of the power supply, preventing the evaluation of the actual current needs of these devices during operation. Dedicated circuitry evaluating the flowing current from the EAD to the ground path, along with voltage measurement external unit, will be introduced in Chapter 6, where more formal device characterization is performed, from both the mechanical and the electrical point of view.

As mentioned in 6.4.2 , a performance degradation appeared after EADs exhibited electrical discharge burning the electrodes from 6kV, but not permanently shortcutting the device. Such a phenomenon implies that the interface between the two dielectric layers represents the weakest part of the device when applying a high voltage across the electrodes. Thus, it suggests that an improvement of maximum achievable ESS or of device dielectric strength, i.e. the maximum

applied voltage to the EAD, might be exploited by enhancing the adhesion between the two dielectric layers. A focus on these aspects is presented in Chapter 7, which proposes a manufacturing optimization aiming to increase EAD performance from both mechanical and electrical points of view.

The dielectric strength of EADs is as indicative as crucial on assessing the performance of these electromechanical devices. Although this aspect of EAD performance was never formally considered in Chapter 5. and Chapter 6., being the breakdown voltage evaluated while doing ESS test, applying a DC step voltage signal to the specimens, in Chapter 7. a systematic approach, inspired to the standard [24], will be added to the characterization procedure.

# **Chapter 7. PI based EADs:**

## **Manufacturing optimization and performance improvement**

### **7.1 Introduction**

Chapter 6. introduced a promising EAD composition able to reach ESS results among the highest in the literature [8], [23], [32], [36], [37], [39], [40]. It must be considered that the obtained results are not only influenced by the deployed materials but also by the manufacturing process adopted. Therefore, an investigation on possible manufacturing optimizations might be the key for further performance improvements of such EADs. This chapter proposes a characterization study performed on EADs having constitutive materials corresponding to the ones adopted in Chapter 6. but classified in six different manufacturing procedures, differing by adding intermediate production steps to the process proposed in Chapter 6.

Produced EADs groups feature inkjet printed comb-like interdigitated electrodes onto a Polyimide (PI) film, and a blade-casted PDMS backing layer, and they differ by surface treatments combinations applied on the PI main dielectric layer, hosting the electrode couple, before completing the EAD assembling with the backing layer.

Introduced surface treatments aim to increase the adhesion between the two dielectric layers embedding the electrode couple, and they consist of:

- Silicone primer application, which was actually also present in the manufacturing process adopted in Chapter 5.
- Low-pressure oxygen plasma exposure

As emerged in 6.4.2 and discussed in 6.6 , the interface between the main dielectric layer and the backing layer represents the most critical region of such EADs when a high voltage is applied. Indeed,

EADs exhibited electrode burn-away caused by corona discharge in the interface region of the two dielectric layers before electrical breakdown occurrence, causing an ESS performance degradation.

The enhancement of the adhesion between the two dielectric layers might not only increase the dielectric strength of produced EADs, enlarging the applicable voltage range, but possibly, it increases the ESS performance.

An experimental campaign is conducted using an ad-hoc designed test bench, allowing capacitance measurements and capable of performing shear force and breakdown tests. The test bench is fully automated and consists of a screw-driven linear guide actuated by a DC motor controlled by an IPC, which monitors and commands all the meaningful electrical signals. The complete setup arrangement will be detailly described in the next sections.

Capacitance mean values and standard deviation for all the six manufacturing process are reported, determining the manufacturing repeatability.

Following the standard for the determination of the friction coefficient for plastic films and sheeting [22], ESS assessment from 0 to 3 kV of applied DC voltage compares the adhesive performance among the six manufacturing procedures while grasping a PET film, i.e. the best performing materials as concluded in Chapter 6.

Breakdown voltage evaluation provides the effectiveness of the manufacturing procedures on the dielectric strength of the devices. The dielectric strength of the specimens is identified following the standard norms for the electrical breakdown analysis of dielectric systems [24].

Moreover, an analysis of the energy and power consumptions of the tested specimens is performed, eventually highlighting differences among the different manufacturing processes. The consumptions are analyzed during one cycle of operation at each voltage level, during ESS tests execution.

As a result, the best performing production process is defined, which resulted as the procedure having the main dielectric layer exposed to oxygen plasma firstly and then covered with a silicone primer layer, before PDMS casting procedure.

To further compare the reference manufacturing process described in Chapter 6. and in [32] with the evinced best-performing process, an up-to-breakdown ESS test is conducted, highlighting the ESS performance improvement achieved.

To confirm and validate the repeatability of the best manufacturing process, as well as the ESS-Device area independency, a scalability analysis is conducted, comparing ESS performance of EADs having three different sizes: 144 mm<sup>2</sup>, 480 mm<sup>2</sup>, and 960 mm<sup>2</sup>.

## 7.2 Design and manufacturing

This section outlines the design and the manufacturing procedures of the produced EADs. The device architecture, together with all the technological processes adopted for device components fabrication, is described. A classification of six different manufacturing procedures identified by distinct combinations of consecutive surface treatments will be presented afterward. Finally, an explanatory specimen manufactured with the mentioned procedure is shown.

### 7.2.1 Design and materials

The EADs proposed in this work are composed of the main dielectric layer, acting also as adhering surface, the electrode pair, featuring an interdigitated geometry, and the backing encapsulation layer, insulating the device preventing electrical breakdown keeping device flexibility. In the following section, each of the constitutive components and the EAD design will be detailly described.

#### 7.2.1.1 EAD design

Figure 83 depicts a schematic top-view and a cross-section of the proposed EAD, indicating all the design parameters:  $g$  is the gap distance between the electrode strips;  $w$  is the strips width;  $N_{\text{pos}}$  and  $N_{\text{neg}}$  are the numbers of strips for the positive and negative electrodes;  $L$  and  $H$  are the lengths and the height of the area containing the interdigitated geometry and determines the size of the specimens;  $t_{\text{ml}}$  is the thickness of the main dielectric layer;  $t_{\text{bl}}$  is the thickness of the backing layer.

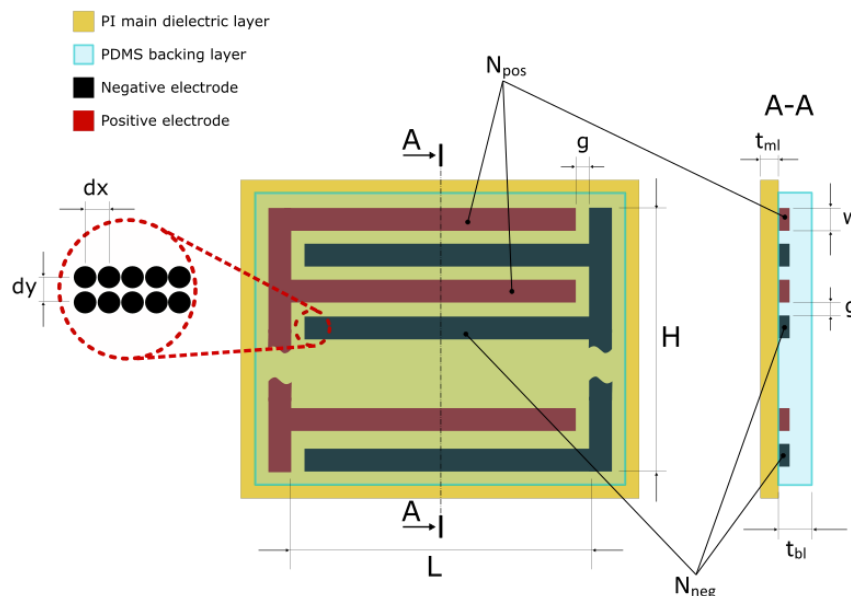


Figure 83 - Schematic of the EAD design with significant geometrical parameters

### **7.2.1.2 The main dielectric layer**

As the main dielectric layer, an industrial Polyimide (PI) film provided from Caplinq® (PIT1N/210) is deployed. The following electro-mechanical properties made this material suitable for this purpose:

- Nominal thickness of 25.4  $\mu\text{m}$ ; favorable for high polarization of the material at moderate applied voltage values, allowing a thin, flexible, and lightweight device production.
- Dielectric strength of 236 MV/m and dielectric constant of 3.9; relatively high values if compared to commercially available thin films, making PI resisting to high electric fields exhibiting high polarizability, leading to a high surface charge distribution that is at the base for EA force generation
- Volume resistivity of 1  $\text{M}\Omega\cdot\text{cm}$ ; indicating good dielectric properties
- Continuous use temperature of 260  $^{\circ}\text{C}$ ; making it possible to adopt thermal treatments without altering film mechanical properties
- Tensile strength greater than 135 MPa; making this material very resistant to traction, giving mechanical support during EA tangential force characterization

Moreover, being provided in rolls extruded with consolidated industrial processes, this film has a controlled thickness and low surface roughness. Therefore, this PI film results as a good candidate as the printing substrate for electrode patterning, allowing high-definition geometries printing.

### **7.2.1.3 The electrode pair**

A comb-like shape of two interdigitated electrodes constitutes the electrode pair. This geometry pattern is inkjet printed onto the main dielectric layer described in 7.2.1.2 using Jetlab® 4xl drop-on-demand (DoD) inkjet printer (3.3 ), equipped with a piezoelectric nozzle (MJ-AT-01) having a diameter of 50  $\mu\text{m}$ . Printhead height was fixed such that the distance between the platen and the nozzle tip was 1.5 mm.

DGP 40LT-15C silver nanoparticle ink, provided by Anapro, is a plastic-film-compatible conductive ink used in this work for electrode patterning. It is characterized by a low resistivity (in the range 11-12  $\mu\Omega\cdot\text{cm}$ ) and curing temperature (in the range 120-150  $^{\circ}\text{C}$ ) feasible with other deployed material operating temperatures.

A single pulse trapezoidal voltage waveform having rise and fall times equal to 3  $\mu\text{s}$ , a pulse width of 33  $\mu\text{s}$ , and pulse amplitude equal to 38 V, jets the ink from the nozzle orifice (3.2.2 , 3.5.1.1). The ink inside the printing channel is at a pressure of -12 mmHg to compensate for gravity, preventing ink from flowing out from the nozzle uncontrollably. The platen temperature was 50  $^{\circ}\text{C}$  to accelerate solvent evaporation, increasing ink stability on the substrate. The nozzle temperature was set to 35



°C to have further control on the printing procedure. The printing speed was 10 mm/s while jetting droplets spaced by 0.17 mm along printing direction and by 0.20 mm along the orthogonal direction to the printing one, denoted as  $dx$  and  $dy$  respectively in the Figure 83. This droplet spacing setting resulted optimal for this ink-substrate couple since printed geometries exhibited homogeneous infill and straight and well-defined boundaries.

After printing, the PI film with deposited ink is transferred in the oven and cured for 45 minutes at 120 °C to enable the sintering of the silver nanoparticles.

#### **7.2.1.4 The backing insulation layer**

Insulating the electrode couple and keeping the lightweight and flexible design, a blade-casted PDMS thin layer is adopted as the backing layer.

Part A and part B of liquid silicone rubber Silpuran® 6000/05 are mixed with DOWSIL™ OS-2 silicone solvent with a weight ratio of 5:5:8, respectively. The compound is homogenized in a planetary-centrifugal mixer (Thinky ARE-250) for 2 minutes at 2000 rpm and then degassed for 2 minutes at 2000 rpm. The air-bubble-free mixture was blade-cast using an automatic film caster (TQC Sheen AB3655) equipped with an adjustable blade (VF1823), set to 400 µm, and moving at 1mm/s. The whole procedure is performed in a laminar flow hood having 50% humidity and 26°C of temperature in the chamber, where samples rest for two hours after the casting. Sample resting avoids air bubble formation caused by fast solvent evaporation occurring when placing specimens in the oven right after casting. After two hours of resting, the PI film, having insulated electrodes, is placed in the oven at 120 °C for 20 minutes for vulcanization. The resulting layer exhibits a volume reduction of around 50%, featuring 200 µm thickness.

### **7.2.2 Manufacturing steps**

The manufacturing steps for producing EAD specimens based on the materials and production processes defined in 7.2.1 are six, and they are shown in the Figure 84.

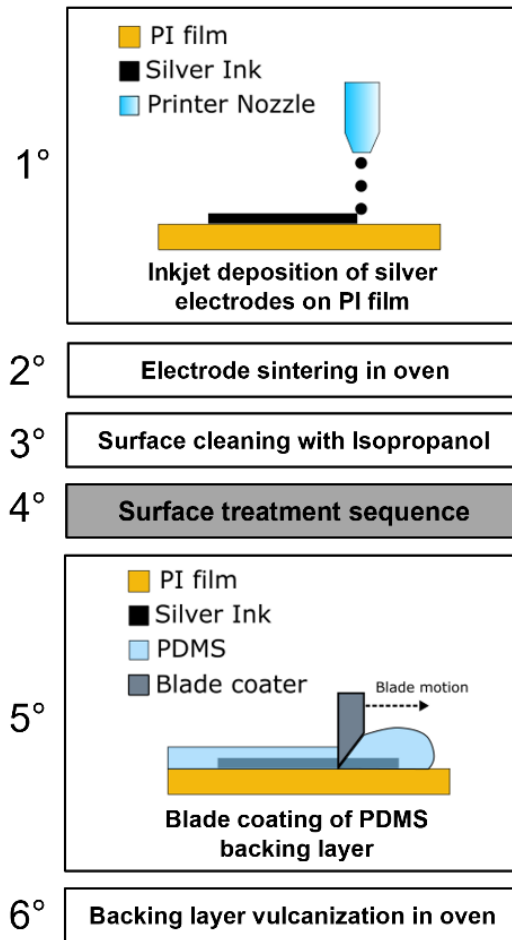


Figure 84 - Manufacturing step constituting the production process adopted

The fourth manufacturing step indicated as “surface treatment sequence” contains six distinct combinations of surface treatments, identifying six manufacturing procedures.

Surface treatments are performed on the PI surface with the printed electrodes before coating the device with the backing PDMS layer. Considered surface treatments are the following:

**Silicone primer application** (DOWSIL™ 1200 OS): it delivers active ingredients on the surface when applied as a thin uniform layer. Active ingredients react with polymeric chains of heat cure silicones, enhancing bonding/adhesion to many metals, ceramics, glass, wood, masonry, and structural plastics. Primer is applied onto the surface with a fiberless cloth and left resting for ten minutes. The process is performed in a laminar flow hood that keeps the chamber at 50% humidity and 26°C.

**Plasma treatment:** it modifies surface chemistry, adding polar functional groups, improving chemical and physical interactions, and increasing the surface energy of polymers [94]. Diener ATTO

low pressure plasma system is used to perform oxygen plasma exposure of samples for one minute, with a power of 60 W, and setting the chamber pressure at 0.8 bar. These machine settings were optimal for surface activation without material etching, which takes place at higher power, or with longer exposure time, or at lower chamber pressure. Any of these factors led to non-conductive electrodes due to silver removal.

Table 10 shows how these two surface treatments are combined so that they identify six different manufacturing procedures.

**M0:** No treatments were applied to enhance the comparison with all the surface-treated cases.

**M1:** Procedure presented in [32] and used as a landmark for the manufacturing optimization process carried out in this context.

**M2:** Plasma treatment is applied to PI film to propose a greener primer-free manufacturing procedure focused on the effect of plasma on adhesion improvement between PI and PDMS layer.

**M3:** Plasma treatment is applied on a primer-covered PI surface. This procedure aims to highlight any enhancement of the primer effect on the casted PDMS compound caused by the plasma surface activation.

**M4:** PI surface is exposed to plasma treatment before primer application. In this case, the plasma treatment is supposed to enhance the primer effect on the PI film.

**M5:** Combines M3 and M4 for a manufacturing procedure that theoretically enhances the interaction between the PI film and the primer with the first plasma treatment while maximizing the adhesion with casted PDMS, treating with plasma the primer layer.

A manufacturing procedure having a first primer application followed by plasma treatment and a second primer application is not performed. Treating the primer-covered surface with plasma could increase adhesion with casted PDMS, as it is supposed for M3. However, if plasma treatment is followed by another primer application, the latter would cover the plasma effect to the successive PDMS casting phase. In that case, the plasma would affect only the surface between the two primer layers, which is not of interest.

Furthermore, consecutive repetitions of the same treatment were not considered since multiple plasma treatments of the PI surface would etch silver electrodes, making them not conductive. Multiple primer applications, instead, would not be more effective if compared to one single application.

Surface treatment sequence			
Manufacturing ID (M#)	1° Treatment	2° Treatment	3° Treatment
M0	✗	✗	✗
M1	Primer	✗	✗
M2	Plasma	✗	✗
M3	Primer	Plasma	✗
M4	Plasma	Primer	✗
M5	Plasma	Primer	Plasma

Table 10 - Definition of the six manufacturing procedures identified by surface treatment sequences

### 7.2.3 EAD presentation

A demonstrative EAD fabricated with the proposed method is shown in Figure 85, having the following nominal dimensions:  $g = 300 \mu\text{m}$ ,  $w = 400 \mu\text{m}$ ,  $N_{\text{pos}} = 4$ ,  $N_{\text{neg}} = 5$ ,  $L = 24 \text{ mm}$ ,  $H = 6 \text{ mm}$ ,  $t_{\text{dl}} = 200 \mu\text{m}$  and  $t_{\text{ml}} = 25.4 \mu\text{m}$ , as referred to geometrical parameters in the Figure 83.

A detail of the printed interdigitated geometry showing the tip of an electrode strip, acquired with Jetlab® 4xl optical system, as well as electrode strips and gap dimensions acquired by the Dino-Lite USB microscope, demonstrates the geometry consistency with the nominal values of the geometrical parameters, being the dimension error within the machine accuracy tolerance.

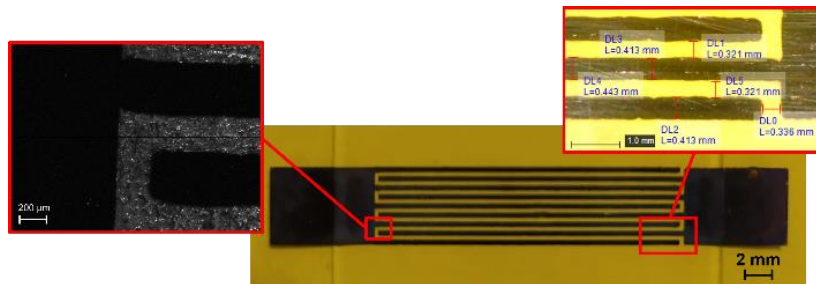


Figure 85 - Example of a produced sample showing an electrode detail acquired by Jetlab® 4xl optical system (left), and geometry measurements acquired with Dino Lite USB Microscope (right)

## 7.3 EAD testing

Produced EADs have been tested for performance assessment among the six different manufacturing procedures. The experimental setup used for testing is described hereafter. The testing methodology for ESS measurement and breakdown voltage assessment is later described. The performance evaluation is carried out considering several factors: the breakdown voltage, the ESS, and the device consumptions. The performance optimum is set in agreement with the best

compromise between these indices, leading to a wide workable voltage range during the EADs applications while exerting an ESS as high as possible.

### 7.3.1 Test bench description

The test bench used in this work consists of a fixed stage, where the specimen is blocked and powered, and a linear guide, driven by a DC motor, hosting the load cell and the grasped PET film. The real test bench is depicted in Figure 86a, while Figure 86b shows the CAD assembly. In the setup, the EAD sample is sandwiched between two PMMA plates used as sample holders, leaving the adhering surface free and assuring a correct position of the specimen with respect to the moving part of the bench. Furthermore, the top holder plate covering the EAD is equipped with copper strips for the electrical connection of the specimen HV and GND electrodes. The testing PET substrate is aligned with the medium plane of the EAD specimen and load cell (NS-WL1-10 kg), whose height is adjusted by a vertical rail. An IGUS linear guide controlled by a DC motor (FAULHABER Series 2342 CR) forces the paper sheet to move on the plane of the EAD adhering surface. The testing setup replicates the ISO 8295 standard requirements [22] to determine the friction coefficient of the main dielectric layer over the PET substrate.

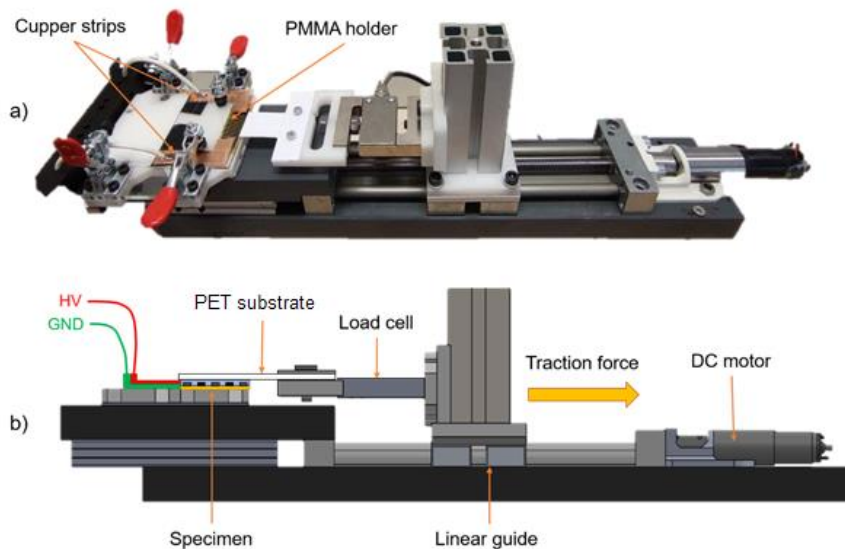


Figure 86 - (a) real arrangement of the mechanical part of the experimental setup. (b) CAD side-view of the test bench

Commanding and measurements signals are managed by CX5140-0125 Beckhoff IPC equipped with I/O modules (EL3356, for interfacing loadcell; EL3104, for analog inputs; EL4732, for analog

outputs, EL2004 for digital outputs) at a sampling frequency of 2kHz. Beckhoff IPC also pilots an Arduino Uno which drives the DC motor.

Two high voltage (HV) power supplies are deployed and toggled by a controlled relay:

- HV1: Ultravolt 10HVA24 is used for ESS tests due to its high precision and fast dynamic response output voltage, enabling bipolar AC and DC HV signal generation with a maximum amplitude of  $\pm 10$  kV.
- HV2: Ultravolt 40A12-P4-E is used for breakdown tests instead, capable of unipolar 40 kV DC HV signal generation.

Both power supplies provide monitoring signals for voltage and currents at the output side. However, external circuitry for current and voltage measurements at the specimen side are deployed to detect directly voltage applied to the EAD and the current flowing in and out the specimen.

A voltage divider (VD), described in Figure 87, is connected in parallel to the EAD, providing a buffered voltage monitoring signal isolated from the high voltage side.

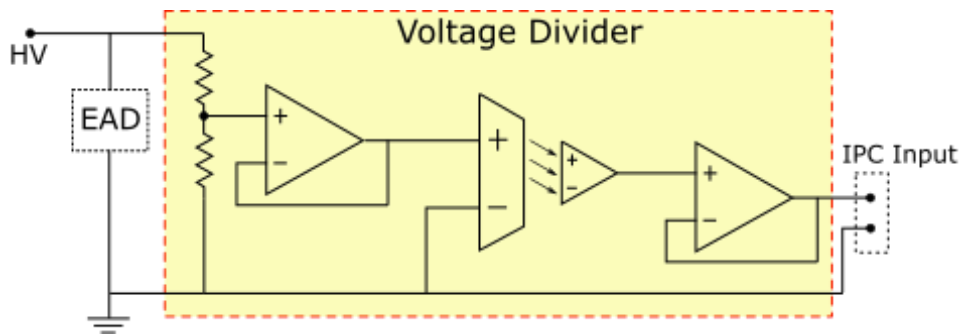


Figure 87 - Electrical scheme of the voltage divider interfacing with the IPC input module EL3104

In series with the EAD is connected a current monitor (CM). This circuitry is based on an inverting amplifier, whose output signal was also buffered, as shown in Figure 88.

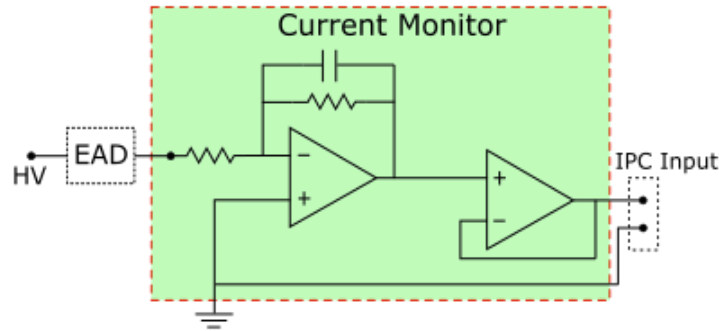


Figure 88 - Electrical scheme of the current monitor interfacing with the IPC input module EL3104

Signal buffering aims to increase the input impedance of the measuring unit, preventing current flow inside the control unit. These dedicated measuring circuitries are powered by two 12 Volts batteries to eliminate grid noise in the monitoring signals.

The mechanical part of the experimental setup interfaces with the electrical circuitry as shown in the Figure 89.

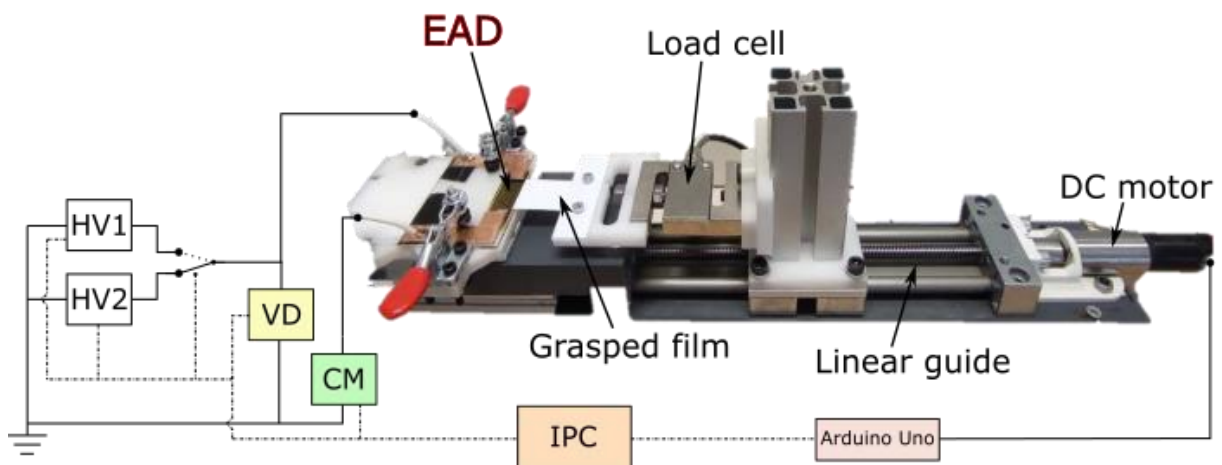


Figure 89 - Schematic of the interconnection between the electrical and the mechanical part of the test bench

### 7.3.2 Experimental procedure for ESS measurement

In agreement with ISO 8295 standard [22], ESS was measured as it is for the determination of the friction coefficient for plastic films.

The EAD is positioned and blocked on the fixed stage while the grasped film is connected to the force sensor mounted on the motorized linear guide.

The grasped film is a 130  $\mu\text{m}$  thick PET substrate provided by JetStar Standard Inkjet Film. The choice of this material is motivated by results reported in our past work [32], where it appeared as the

best performing material during ESS tests performed on EADs having the same constitutive materials deployed in this study.

The specimen is placed in contact with the PET film from the PI surface side, under a homogeneous pressure of 600 Pa generated by a reference load, as suggested by [22].

Subsequently, a DC high voltage signal is applied to the EAD from the power supply and, after two seconds, the grasped film is pulled away from the motor while recording the tangential force.

This procedure is repeated three times for each voltage step amplitude, providing a consistent data set for an ESS results statistical analysis.

Step voltage polarity switches from positive to negative between consecutive tests. This technique avoids depolarization effects that lead to an electric field saturation with consequent force reduction [26].

The ESS value is calculated as the measured peak take-off force divided by the tested specimen area. The latter is obtained as the multiplication between L and H, as indicated in 7.2.1.1.

When performing ESS test, a controller constantly checks whenever the current exceeds the 80% of the maximum measurable current of 100  $\mu$ A. If this happen, the experiment is stopped, and the specimen is considered as electrically broken. This control layer allows to determine the safe EAD operation, without considering ESS data after electrical discharges that burns the electrode strips without permanently shortcutting the device, differently to what was done in 6.4.2 .

### **7.3.3 Experimental procedure for breakdown assessment**

Breakdown voltage assessment follows the standard ASTM D149 [24], which specifies the test methodology for the dielectric strength of solid electrical insulating materials at commercial power frequencies.

Specimens' breakdown must occur within 10 - 20 seconds after the test begin while subjected to a ramp voltage signal, as suggested by the so-called Short-time test method.

Preliminary trial tests based on breakdown results reported in Chapter 6. lead to 1kV/s ramp slope.

EAD specimens, placed on the fixed stage of the test bench having the PI surface facing upward, were energized with a ramp voltage signal until electrical breakdown occurred. The current monitor continuously measures the absorbed current. When it exceeds 80% of the maximum measurable current of 100  $\mu$ A, the test is stopped.

The breakdown voltage corresponds to the applied voltage at the time the test was interrupted.



## **7.4 Experimental results and discussions**

This section contains the results obtained by the experimental campaign described in 7.3 . The first step of the characterization process consists of a reference geometry assessment. In particular, the size of the reference geometry is defined based on breakdown results obtained by different size EADs, always featuring interdigitated electrodes, and manufactured according to M1 process. This preliminary step was mandatory for reducing material wastes since the successive breakdown characterization tests are destructive. The defined reference geometry is assessed in order to maintain the consistency of the obtained results, allowing to extend all the considerations to bigger size equally produced EADs.

Successively, the capacitance, the ESS performance, the breakdown voltages, and the electrical consumptions are compared among the six manufacturing procedures for EADs featuring the reference size. According to the obtained results, the best performing manufacturing process is defined and further compared with the reference one (M1) in terms of ESS, with an up-to-breakdown ESS testing method.

Finally, a scalability analysis comparing ESS on three different sizes EADs manufactured with the process evinced by the previous characterization phase is present.

### **7.4.1 Electrode geometry assessment**

Breakdown tests were performed on EADs having  $N_{\text{pos}}$  equal to 1, 2, 3, 4, 6, and 12, while the parameter  $N_{\text{neg}}$  was set equal to  $(N_{\text{pos}}+1)$ , aiming to assess a reference electrode geometry.

Following the breakdown test procedure described in 7.3.3 and manufactured with the process M1 presented in 2.2, seven EADs for each  $N_{\text{pos}}$  value were produced and tested.

As can be seen from the Figure 90, for  $N_{\text{pos}}$  equal to 1, 2, and 3, the breakdown voltage mean value increases, rising from 8.8 kV to 9.5 kV, while the standard deviation is in the order of 700-600 Volts. For  $N_{\text{pos}}$  equal to 4 and 6, the mean value stabilizes around 8.5 kV, and the standard deviation goes below 500 Volts. For  $N_{\text{pos}}$  equal to 12, the mean value increases to 9 kV while the standard deviation is 510 V.

The reference geometry is picked fulfilling the following requirements:

- Minimize the size of the reference EAD.
- Breakdown voltage standard deviation is as low as possible.

Under these assumptions, and supposing that the mean value of the breakdown voltage maintains stability for values of  $N_{\text{pos}}$  in the 6÷12 interval and above 12, the reference EAD electrode geometry is picked with  $N_{\text{pos}} = 4$ , corresponding to the one depicted in Figure 85.

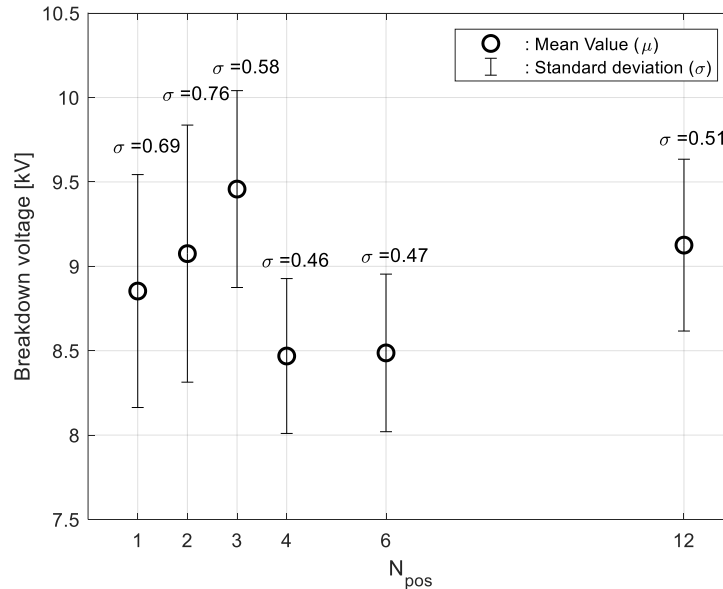


Figure 90 - Breakdown voltage results obtained by reference geometries differing by the number of electrode strips connected to the high voltage

### 7.4.2 EAD capacitance results

The capacitance of ten samples produced for each of the six different manufacturing processes described in 7.2.2 , featuring the reference geometry defined in 7.4.1 , was measured at 20 Hz with an LCR meter (Rohde & Schwarz HM8118), while the specimen was kept on the fixed stage of the test bench described in 7.3.1 , having the PI adhering surface facing upward left free in the air.

Obtained capacitance measurements are listed in the Table 11, which reports the mean values and standard deviations.

The complete absence of surface treatments leads to capacitance standard deviation increment for the M0 manufacturing procedure. Probably, this is caused by uncontrolled adherence between the PI and PDMS layers.

Besides, M2, M4, and M5 exhibited high capacitance standard deviations compared to M1 and M3. In this case, the cause can be the direct plasma exposure of the electrodes, which is the common factor of these manufacturing procedures, possibly leading to random electrode etching.

Globally, all the manufacturing procedures led to specimens having a capacitance in the 5÷6 pF range, indicating that the applied surface treatments mainly affect capacitance oscillation but not the

average value, which is dominantly dependent on EAD geometry and constitutive materials, which are the same for all the manufactures.

	$\mu_c$ (pF)	$\sigma_c$ (pF)
<b>M0</b>	6,72	1,76
<b>M1</b>	5,72	0,48
<b>M2</b>	6,27	1,27
<b>M3</b>	6,26	0,5
<b>M4</b>	5,38	0,85
<b>M5</b>	5,83	0,97

Table 11 - Capacitance mean value and standard deviation calculated by the measured capacitance on all samples belonging to the six different manufacturing procedures

### 7.4.3 ESS performance among manufacturing procedures

Following the testing procedure described in 7.3.2 , featuring the reference geometry defined in 7.4.1 , ten specimens were produced and tested for each manufacturing procedure, under a DC step voltage signal ranging from 0 to 3 kV, with 1 kV of voltage increment. Obtained results are shown in the Figure 91, which reports ESS performance among different manufacturing while grasping a 130  $\mu\text{m}$  thick PET film. The error bars represent the standard deviation, while the displayed number corresponds to the average of the measured ESS values. The ESS standard deviation increased as the applied voltage increase for all the batches, while ESS results for all the manufacturing procedures can be summarized as follows:

**M0** exhibited the lowest ESS results, being the mean adhesive pressure equal to 6.05 kPa when the M0-specimens were powered at 3 kV.

**M1** results are consistent with what was reported in Chapter 6. since ESS mean values almost reached 19 kPa at 3 kV. The ESS-Voltage characteristic revealed a quadratic-like trend.

**M2** and **M3** disclosed similar ESS results, exhibiting an explicit a clearer quadratic relation between ESS and the applied voltage, reaching around 27 kPa at 3 kV.

**M4** revealed the highest ESS results, achieving 40.14 kPa at 3 kV, representing a doubled ESS performance increase comparing to M1.

**M5** did not show significant performance improvement, having a less evident ESS-Voltage quadratic relation and an ESS plateau appeared from 2 kV to 3 kV.

**ESS results for different manufacturing procedures**

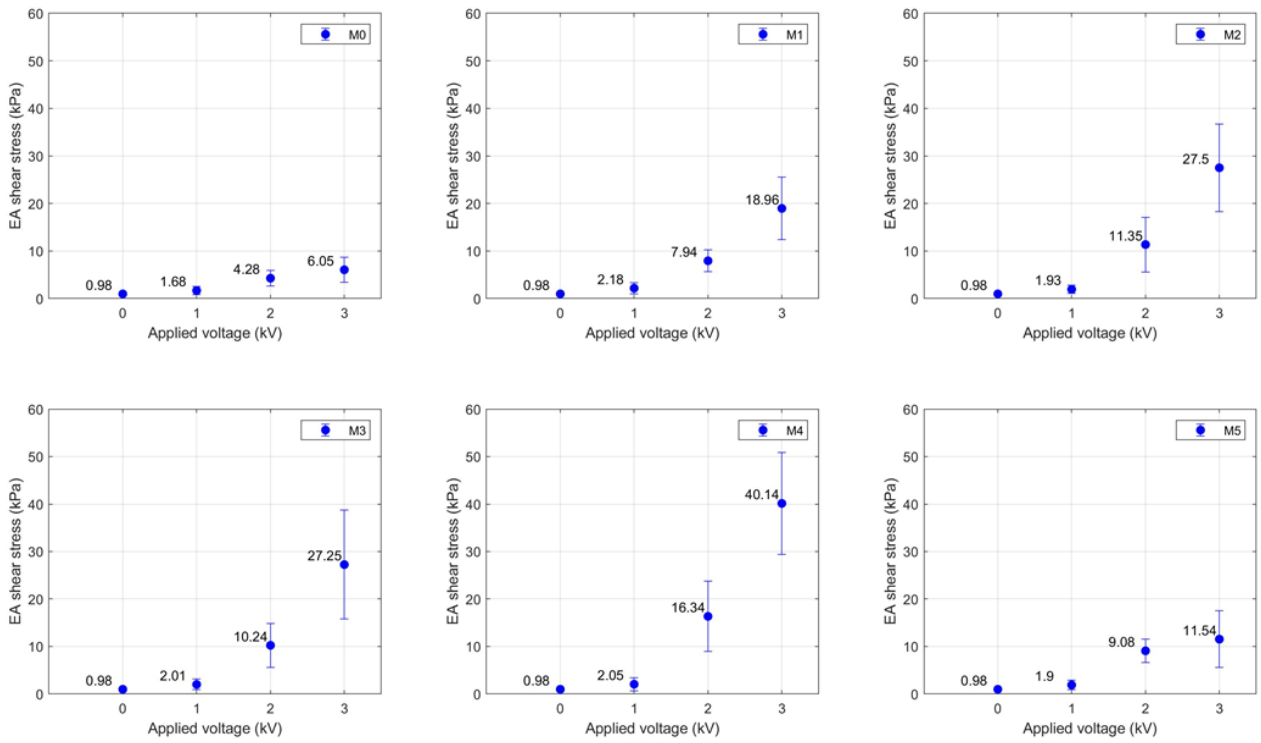


Figure 91 - ESS results obtained at 0 kV, 1kV, 2kV, and 3kV for all the six different manufacturing procedures

**7.4.4 Energy and Power consumptions**

Thanks to the measurement circuitries described in 7.3.1 , current and voltage signals have been used for calculating the power and energy consumed during ESS tests reported in 7.4.3 . The time duration for each ESS test was 5.5 seconds. The Table 12 summarizes for each voltage values the mean value of the energy consumed during ESS tests, referred to as one cycle of activation, and the absorbed power for charging EADs, calculated as the multiplication by the applied voltage and the peak charging current. The consumed energy showed no significant variation among all the manufacturing procedures since the capacitance difference among manufactures was in the order of one pico-farad. Moreover, charging power values demonstrates a very high ESS-Power ratio, indicating EADs as an energetically efficient class of actuators.

	One-Cycle Energy consumed (mJ)			Charging power absorbed (mW)		
	1 kV	2 kV	3 kV	1 kV	2 kV	3 kV
M0	0,022	0,111	0,243	1,326	4,601	8,511
M1	0,029	0,132	0,317	1,818	7,016	15,034
M2	0,021	0,112	0,270	1,489	4,979	10,050
M3	0,021	0,119	0,268	1,444	4,692	8,980
M4	0,019	0,112	0,267	1,384	4,485	8,889
M5	0,020	0,111	0,256	1,517	4,671	9,463

Table 12 - Mean value calculated from the energy consumed and the power absorbed by all samples, during on test, belonging to the six different manufacturing procedures

### 7.4.5 Breakdown voltages among manufacturing procedures

Following the testing procedure described in 7.3.3 , all the sixty produced samples featuring the geometry shown in 7.2.3 were tested for breakdown voltage assessment.

Obtained results are reported in Figure 92, which depicts the mean values ( $\mu$  and blue circles) and the standard deviations ( $\sigma$  and error bars) of the breakdown voltages for all the six manufacturing procedures.

Comparing M0 and M1, it can be asserted that a primer application almost half the oscillations of the breakdown voltages but does not bring significant dielectric strength increase of EADs.

Despite an increase of the breakdown voltage mean value of up to 11 kV, M2 EADs exhibited a larger standard deviation of around 1.5 kV, probably caused by electrode random etching due t plasma exposure, as mentioned in 7.4.2 . The same effect takes place for M4 and M5 EADs, which have electrodes directly exposed to plasma treatment, showing a standard deviation of 0.88 kV and 1.17 kV respectively.

M3 specimens demonstrated that a plasma treatment after a primer application increments of almost 1 kV the mean breakdown voltage of the EADs, keeping a low standard deviation of 0.58 kV.

Globally, plasma exposure of EADs demonstrates to increase the breakdown voltage of the specimens of at least 1 kV, following the procedure described in 7.2.2 . Moreover, silicone primer application combined with plasma treatment increased EADs dielectric strength (at least 1 kV more in the mean of the breakdown voltages comparing to M1) keeping a reasonably low standard deviation, independently from the order followed when applying such treatments.

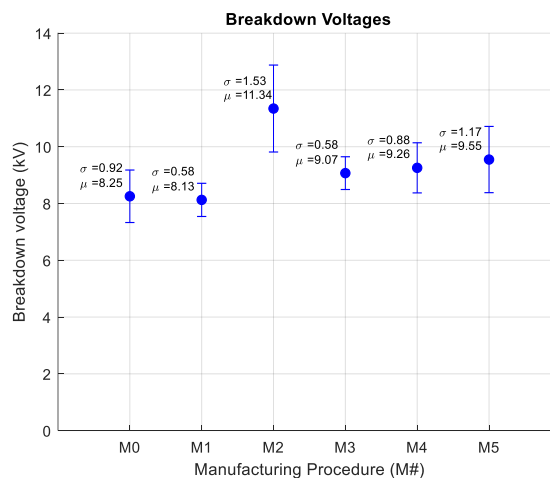


Figure 92 - Breakdown voltages mean values and standard deviations obtained by the six manufacturing procedures

### 7.4.6 ESS comparison between M4 and M1

Considering the results reported in sections 7.4.2 ,7.4.3 ,7.4.4 , and 7.4.5 , the manufacturing process denoted as M4 was considered as the best performing, which demonstrated:

- Mean Capacitance equal to 5,38 pF
- Mean ESS at 3 kV equal to 40,14 kPa
- Mean breakdown voltage of 9,26 kV.

To further explore the capability of such manufacture and to enhance the comparison with the reference manufacturing M1, additional ESS tests were conducted on EADs featuring the reference geometry defined in 7.4.1 and following the 7.3.2 procedure.

Figure 93 reports ESS results of five M1 and M4 specimens when tested under DC voltage having amplitude rising from 0 kV to 3 kV with 0.5 kV increment, and from 3 kV till the electrical breakdown with 0.3 kV increment.

M4 samples are all located in the upper part of the ESS-Voltage plane. As it was in 7.4.3 , ESS results spread more as the voltage increases. Moreover, the ESS characteristic follows a quadratic relation with the applied voltage until 3 - 4 kV while the trends follow a linear growth above 3 kV till the electrical breakdown occurrence.

The maximum ESS achieved is around 110 kPa for M4 samples at 6.2 kV, while M1 samples reached almost 80 kPa at 6.4 kV. Samples exhibiting higher ESS results resulted with earlier electrical breakdown for both manufacturing procedure.

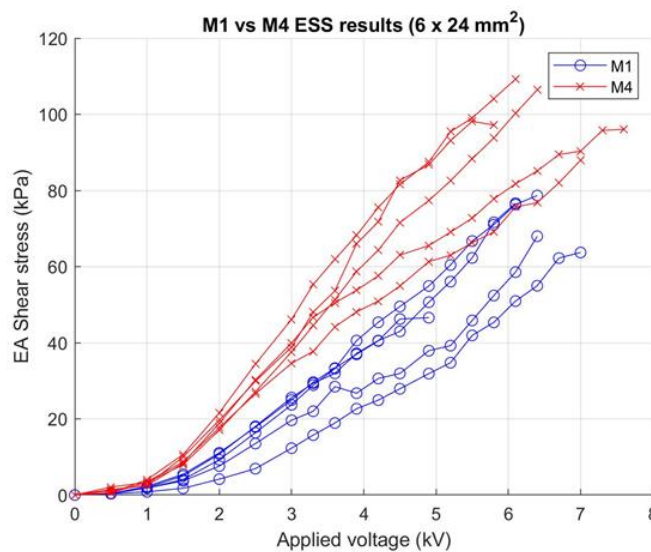


Figure 93 - ESS results comparisons between M1 and M4 samples with applied voltage rising till breakdown occurrence

### 7.4.7 EAD scalability analysis for M4 specimens

As a final validation of the manufacturing process M4, a scalability analysis was conducted. ESS tests, following the procedure described in 7.3.2 , were performed on three different sizes of EAD. The different sizes are identified as “small”, corresponding to the reference geometry defined in 7.4.1 , “medium”, and “large”, having areas of 144 mm<sup>2</sup>, 480 mm<sup>2</sup>, and 960 mm<sup>2</sup> respectively, as shown in Figure 94.

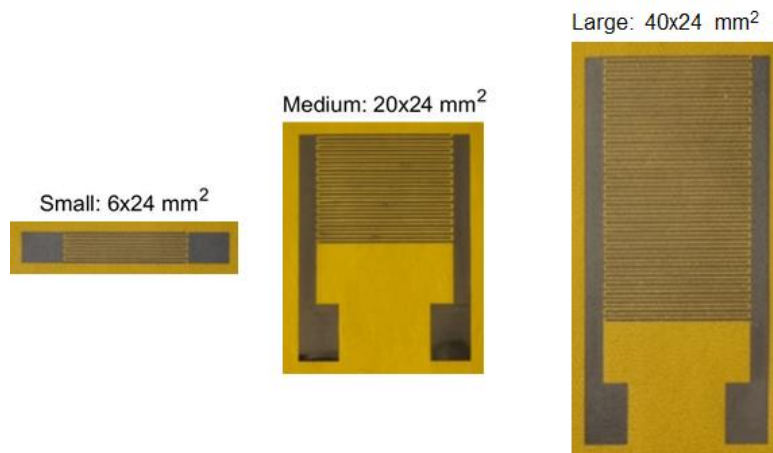


Figure 94 - Three different sized of the produced EADs tested for the scalability analysis

Four samples of each dimension have been produced and tested, following the procedure described in 7.3.2 . Specimens were subjected to DC step voltage signal having 0.5 kV increment from 0 to 3 kV and increasing by 0.3 kV from 3 kV till breakdown occurrence.

Figure 95 reports obtained results, showing the average ESS calculated from the tests performed on each sample size category, from 0 V to 5.7 kV, which corresponds to the highest applied voltage where all samples survived. As it was in 7.4.3 and 7.4.6 , ESS-Voltage characteristic exhibits a quadratic trend up to 3 – 4 kV then turning into a linear growth. Maximum mean ESS achieved at 5.7 kV is 111.11 kPa for large EADs, 86.79 kPa for medium and 82.35 kPa for the small ones.

Despite the surprising similarity between medium and small EADs ESS results, the large EAD exhibited a faster growth of the ESS-Voltage characteristic, demonstrating a dependency of the ESS on the patch size. However, the cause of this ESS-Area dependency might be the arrangement of the testing setup. These results indeed suggest that the non-idealities of the contact are strongly affecting the adhesive force, and they scale down as the patch size increase. This might indicate that small and medium patches are capable of better ESS performances with a "more ideal" contact with the PET

film. Nevertheless, the mean ESS of large EADs almost matches the maximum ESS achieved by small specimens (110 kPa at 6,2 kV), as shown in 7.4.6 and Figure 93, indicating that the independence of the ESS by the device area can still be proven.

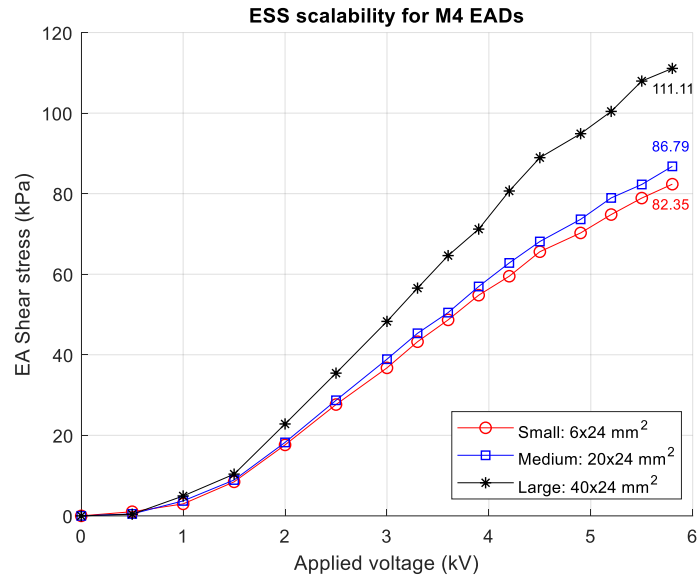


Figure 95 - ESS results comparisons of the three different size EADs for the scalability analysis

## 7.5 Conclusions

This chapter compared the performances of six different manufacturing procedures obtained by a reference manufacturing process, corresponding to the one adopted in Chapter 6.

Manufacturing differentiation consists of the application of two surface treatments: a silicone primer application and oxygen plasma exposure. Both treatments are applied onto the PI surface hosting the electrode before the backing PDMS casting.

A reference geometry was determined first in 7.4.1 by breakdown tests performed on EADs having different sizes, varying only one dimension of the specimens (the height). The aim was to define a representative geometry of the EADs which:

- Allows to extend all the considerations to specimens having different sizes, featuring the same electrode geometry parameters (gap and width) and constitutive materials.
- Limits the material wastes as much as possible since the device characterization campaign comprehends destructive breakdown tests.

Ten samples featuring the defined reference geometry have been produced for all six manufacturing processes.



In 7.4.2 , manufacturing procedures have been validated and compared through the capacitance measurements of the produced samples.

An ESS assessment experimental campaign was conducted on all the specimens belonging to the six manufacturing clusters, applying voltages from 0 kV to 3 kV (7.4.3 ).

The energy and the power consumptions at each voltage level have been evaluated during the ESS tests execution, as reported in 7.4.4 .

Breakdown tests on all the produced samples concluded the first part of the experimental characterization process, as mentioned in 7.4.5 .

The obtained results have been compared to determine the best-performing manufacturing procedure. The manufacturing process denoted with M4, consisting of electrode plasma exposure followed by primer application before the PDMS backing layer casting, exhibited the most promising performance:

- A mean ESS of 40,14 kPa at 3 kV
- A mean breakdown voltage of 9,26 kV
- An average capacitance of 5.38 pF
- Only 0,26 mJ consumed during one ESS test at 3 kV lasted 5.5 seconds
- And only 8,88 mW absorbed for charging EADs when applying 3 kV

Further investigations on the performances of M4-produced samples were conducted. Five more specimens following M1 and M4 processes were produced and tested for additional comparisons.

In 7.4.6 , up-to-breakdown ESS tests highlighted the achieved ESS improvements: M4 specimens always feature a faster ESS rising rate with the applied voltage, reaching up to 100 kPa at 6.2 kV versus the 80 kPa achieved at 6.4 kV by an M1 sample.

It is not surprising that EADs electrical rupture took place at voltages lower than the ones obtained in 7.4.5 . While performing ESS tests, whose results are reported in 7.4.6 and in 7.4.7 , the voltage signal corresponds to a step having a rising rate equal to:

$$\text{Slope} = \frac{\text{Step Amplitude}}{\text{Time step}} = \frac{\text{Step Amplitude}}{0.5 \text{ ms}}$$

Representing a much higher electrical stress if compared to the one generated by the breakdown test described in 7.3.3 , which applies a ramp having only  $\frac{1 \text{ kV}}{1 \text{ s}}$  of slope. Moreover, the mechanical stress EADs are subjected to during ESS traction test might also influence the contact surface between the PI and the PDMS layers, with consequent possible modification of the EAD dielectric strength.

Moreover, differently from what reported in 6.4.2 , the dedicated circuitry for current and voltage measurements described in 7.3.1 allowed to consider any partial discharge of the device as an electrical rupture, hence causing the test ending. Therefore, reported results in 7.4.6 and 7.4.7 are more conservative than what reported in 6.4.2 , representing the EAD performance with a higher safety margin.

Finally, in 7.4.7 , a scalability study was performed, confronting the ESS performances of M4-samples featuring three different sizes. EADs having 144 mm<sup>2</sup>, 480 mm<sup>2</sup>, and 960 mm<sup>2</sup> of prehension area have been produced varying the parameter H, referring to Figure 83. Obtained results demonstrated a good similarity on the ESS characteristic curves between “small” and “medium” EAD sizes. However, “large” EADs ESS resulted higher than the others, suggesting that non-idealities of the contact surface mainly affect smaller size specimens. The following solutions might be adopted to overcome this issue:

- Substituting the testing 130 um PET film with a thinner one, increasing film compliancy and therefore the effective contact area with the EAD.
- Deploying a more precise, though more expensive, production process to manufacture the backing silicone layer, producing more uniform, better thickness-controlled thin films. This solution will lead to a flatter EAD adhering surface since specimens lie on the fixed stage of the test bench with the PDMS side adhered to it. Therefore, any PDMS surface asperities will reflect on the PI adhering surface facing upwards on the other side.

In conclusion, the proposed study revealed an optimized manufacturing process leading to a considerable performance increment regarding the ESS and breakdown voltage, which consists of the most relevant indices for performance evaluation of EADs. In particular, the achievements of M4-samples comparing to M1-samples can be summarized as follows:

- A factor of two of ESS performance increment in the 0-3 kV range.
- A maximum ESS of 111 kPa at 5.7 kV versus the 50 kPa at 6 kV obtained in Chapter 6. from 960 mm<sup>2</sup> EADs.
- An increment of 1.1 kV on the average breakdown voltage.

## Chapter 8. Conclusions

This thesis proposed a methodology for the manufacturing and the experimental characterization of thin and lightweight EADs having inkjet-printed comb-shaped electrodes, deployable for gripping or braking applications. Chapter 1. and Chapter 2. introduced the EA phenomenon and highlighted the importance of an experimental approach for the characterization of the devices. The EAD testing for data collection is helpful for the attainable performance assessment, helps to define the most suitable design and manufacturing procedure, and contributes to empirical models' definition.

Chapter 3 presented the Inkjet printing technology, explaining all the critical issues and main benefits. A detailed description of the deployed printer, a Microfab Jetlab® 4xl, provided all the insights for machine operation. Several examples of printing experiments showed favorable and unfavorable printing conditions with different ink and substrates.

Chapter 4. formally defined a procedure based on DOE and ANOVA for assessing the relationship between the quality of the printed electrode geometry and the most relevant DoD inkjet printing parameters, which resulted in the droplets spacing and the printing temperature. Although a punctual optimum on the parameter set was not defined, the proposed procedure identified parameters ranges of values leading to a proper interdigitated comb-shaped geometry printing. Moreover, the proposed methodology represents a formal procedure for inkjet parameter settings, extendable to other ink-printing substrate couples.

Chapter 5. proposed EADs having a PEEK film as adhering layer and electrode printing substrate. Produced devices were subjected to an ESS performance assessment while grasping an aluminum foil, energy and power consumption analysis, and system time responses investigation. Manufactured EADs featured an active area of  $9.6 \text{ cm}^2$ , a thickness of  $300 \text{ }\mu\text{m}$ , and a weight of  $0.7 \text{ g}$ , and they were able to exert an ESS of  $40 \text{ kPa}$  with an applied voltage of  $7 \text{ kV}$ . Measurement of supply current and voltage highlights a fast system response, around 20 milliseconds for full device electrification, and low energy consumption,  $17 \text{ mJ}$  during one cycle of operation that comprises activation, grasp hold, and release.

Inspired to what was done in Chapter 5, Chapter 6 proposed EADs manufactured with the same procedure but replacing the PEEK main dielectric layer with a PI film of the same thickness, though

characterized by better electrical features (i.e. dielectric constant and dielectric strength). The ESS, the electrical consumptions, and the system time responses were still considered as the most relevant performance indices. The ESS experimental campaign was conducted on a wider set of adhering materials, comprehending electrical conductors and insulators. Peak shear stresses of 56.67 kPa and 45.78 kPa have been achieved by PI-based EADs on coated PET film at 8.3 kV and aluminized PI film at 7.6 kV. 20 mJ for full electrification with a subsequent power consumption of about 1 mW for long-term grasp holding were required during the ESS test, with a time response of around 20 ms. Moreover, a proof-of-concept gripper was realized using two PI-based EADs. The gripper exhibited high versatility, with successful gripping on many objects of different shapes and materials, approaching and releasing the object with no additional actuation needs.

Chapter 7. carried on the PI-based EAD characterization process, refining the manufacturing procedure for a performance enhancement, and performing a characterization procedure including the device dielectric strength assessment. In particular, six different variations of the manufacturing procedure proposed in Chapter 6. were identified by introducing additional surface treatments in the workflow (i.e. low-pressure oxygen plasma treatment, silicone primer application). The six different EAD groups have been compared in terms of ESS performances, breakdown voltages, capacitances, and consumptions. The best-performing manufacturing process resulted as the one having the PI surface treated with plasma subsequently covered with the silicone primer, prior PDMS backing casting phase. EADs produced with such manufacturing were tested for maximum achievable ESS evaluation, which resulted in 100 kPa at 6.2 kV while grasping a PET film. Moreover, scalability analysis was conducted comparing EADs of three different sizes. Results highlighted a performance increment as the patch size increased, probably caused by the higher susceptibility of the ESS on air gaps as the EAD size decreases.

---

# References

- [1] G. J. Monkman, “An Analysis of Astrictive Prehension,” *Int. J. Rob. Res.*, vol. 16, no. 1, pp. 1–10, Feb. 1997, doi: 10.1177/027836499701600101.
- [2] J. Berengueres, K. Tadakuma, T. Kamoi, and R. Kratz, “Compliant distributed magnetic adhesion device for wall climbing,” *Proc. - IEEE Int. Conf. Robot. Autom.*, no. April, pp. 1256–1261, 2007, doi: 10.1109/ROBOT.2007.363157.
- [3] S. Seriani, L. Scalera, M. Caruso, A. Gasparetto, and P. Gallina, “Upside-down robots: Modeling and experimental validation of magnetic-adhesion mobile systems,” *Robotics*, vol. 8, no. 2, pp. 1–20, 2019, doi: 10.3390/robotics8020041.
- [4] R. P. Krape, “Application Study of Electroadhesive Devices,” *NASA Contract. Rep. NASA CR-1211*, pp. 1–10, 1968, [Online]. Available: <https://core.ac.uk/reader/85243250>.
- [5] M. M. Tazetdinov, “Electric fixture arrangements,” *Mach. ToolsRussian*, vol. 3, pp. 33–34, 1969.
- [6] P. M. Taylor, G. J. Monkman, and G. J. F. Farnworth, “Principles of electroadhesion in clothing robotics,” *Int. J. Cloth. Sci. Technol.*, vol. 1, no. 3, pp. 14–20, 1989, doi: 10.1108/eb002951.
- [7] G. Monkman, “Electroadhesive microgrippers,” *Ind. Rob.*, vol. 30, no. 4, pp. 326–330, 2003, doi: 10.1108/01439910310479595.
- [8] J. Shintake, S. Rosset, B. Schubert, D. Floreano, and H. Shea, “Versatile Soft Grippers with Intrinsic Electroadhesion Based on Multifunctional Polymer Actuators,” *Adv. Mater.*, vol. 28, no. 2, pp. 231–238, 2016, doi: 10.1002/adma.201504264.
- [9] C. Xiang, J. Guo, and J. Rossiter, “ContinuumEA: A soft continuum electroadhesive manipulator,” *2018 IEEE Int. Conf. Robot. Biomimetics, ROBIO 2018*, pp. 2473–2478, 2018, doi: 10.1109/ROBIO.2018.8664717.
- [10] O. Zedadra *et al.*, “Inkjet printing of conductive inks with high lateral resolution on omniphobic ‘rF paper’ for paper-based electronics and MEMS,” *Smart Mater. Struct.*, vol. 28, no. 2, pp. 1–6, 2018, doi: 10.1016/j.matdes.2015.09.162.
- [11] J. Guo, K. Elgeneidy, C. Xiang, N. Lohse, L. Justham, and J. Rossiter, “Soft pneumatic grippers embedded with stretchable electroadhesion,” *Smart Mater. Struct.*, vol. 27, no. 5, 2018, doi: 10.1088/1361-665X/aab579.
- [12] G. Gu, J. Zou, R. Zhao, X. Zhao, and X. Zhu, “Soft wall-climbing robots,” vol. 2874, no. December, pp. 1–13, 2018.
- [13] S. D. De Rivaz, B. Goldberg, N. Doshi, K. Jayaram, J. Zhou, and R. J. Wood, “Inverted and vertical climbing of a quadrupedal microrobot using electroadhesion,” *Sci. Robot.*, vol. 3, no. 25, 2018, doi: 10.1126/scirobotics.aau3038.
- [14] K. H. Koh, M. Sreekumar, and S. G. Ponnambalam, “Hybrid electrostatic and elastomer adhesion mechanism for wall climbing robot,” *Mechatronics*, vol. 35, pp. 122–135, 2016, doi: 10.1016/j.mechatronics.2016.02.001.
- [15] H. Prahlad, R. Pelrine, S. Stanford, J. Marlow, and R. Kornbluh, “Electroadhesive robots - Wall climbing robots enabled by a novel, robust, and electrically controllable adhesion technology,” *Proc. - IEEE Int. Conf. Robot. Autom.*, pp. 3028–3033, 2008, doi:

- 10.1109/ROBOT.2008.4543670.
- [16] C. Cao, X. Sun, Y. Fang, Q. H. Qin, A. Yu, and X. Q. Feng, "Theoretical model and design of electroadhesive pad with interdigitated electrodes," *Mater. Des.*, vol. 89, pp. 485–491, 2016, doi: 10.1016/j.matdes.2015.09.162.
- [17] K. H. Koh, M. Sreekumar, and S. G. Ponnambalam, "Experimental investigation of the effect of the driving voltage of an electroadhesion actuator," *Materials (Basel)*, vol. 7, no. 7, pp. 4963–4981, 2014, doi: 10.3390/ma7074963.
- [18] C. Cao, X. Sun, Y. Fang, Q. H. Qin, A. Yu, and X. Q. Feng, "Theoretical model and design of electroadhesive pad with interdigitated electrodes," *Mater. Des.*, vol. 89, no. JANUARY, pp. 485–491, 2016, doi: 10.1016/j.matdes.2015.09.162.
- [19] R. Chen, R. Liu, and H. Shen, "Modeling and analysis of electric field and electrostatic adhesion force generated by interdigital electrodes for wall climbing robots," *IEEE Int. Conf. Intell. Robot. Syst.*, pp. 2327–2332, 2013, doi: 10.1109/IROS.2013.6696682.
- [20] K. Choi *et al.*, "Quantitative Electrode Design Modeling of an Electroadhesive Lifting Device Based on the Localized Charge Distribution and Interfacial Polarization of Different Objects," *ACS Omega*, vol. 4, no. 5, pp. 7994–8000, 2019, doi: 10.1021/acsomega.9b00071.
- [21] J. Guo, J. Leng, and J. Rossiter, "Electroadhesion Technologies for Robotics: A Comprehensive Review," *IEEE Trans. Robot.*, vol. 36, no. 2, pp. 313–327, 2020, doi: 10.1109/TRO.2019.2956869.
- [22] "Plastics - Film and sheeting - Determination of the coefficients of friction BS EN ISO 8295," 2004.
- [23] G. Gu, J. Zou, R. Zhao, X. Zhao, and X. Zhu, "Soft wall-climbing robots," *Sci. Robot.*, vol. 3, no. 25, 2018, doi: 10.1126/scirobotics.aat2874.
- [24] T. Com-, I. Liquids, and U. Disk, "Standard Test Method for Dielectric Breakdown Voltage and Dielectric Strength of Solid Electrical Insulating Materials Under Direct-Voltage," *Astm*, vol. 97, no. Reapproved 2004, pp. 1–6, 2012, doi: 10.1520/D0149-09R13.2.
- [25] D. J. Griffiths and C. Inglefield, *Introduction to Electrodynamics*, vol. 73, no. 6. 2005.
- [26] R. Chen *et al.*, "Time-dependent electroadhesive force degradation," *Smart Mater. Struct.*, vol. 29, no. 5, 2020, doi: 10.1088/1361-665X/ab79b5.
- [27] S. M. J. Mahmoudzadeh Akherat, M. A. Karimi, V. Alizadehyazdi, S. Asalzadeh, and M. Spenko, "A tunable dielectric to improve electrostatic adhesion in electrostatic/microstructured adhesives," *J. Electrostat.*, vol. 97, no. July 2018, pp. 58–70, 2019, doi: 10.1016/j.elstat.2018.12.001.
- [28] J. Guo, T. Hovell, T. Bamber, J. Petzing, and L. Justham, "Symmetrical electroadhesives independent of different interfacial surface conditions," *Appl. Phys. Lett.*, vol. 111, no. 22, 2017, doi: 10.1063/1.5000715.
- [29] D. Ruffatto, A. Parness, and M. Spenko, "Improving controllable adhesion on both rough and smooth surfaces with a hybrid electrostatic/gecko-like adhesive," *J. R. Soc. Interface*, vol. 11, no. 93, 2014, doi: 10.1098/rsif.2013.1089.
- [30] J. Guo, T. Bamber, J. Petzing, L. Justham, and M. Jackson, "Experimental study of relationship between interfacial electroadhesive force and applied voltage for different substrate materials," *Appl. Phys. Lett.*, vol. 110, no. 5, pp. 1–6, 2017, doi: 10.1063/1.4975602.
- [31] J. Guo, T. Bamber, T. Hovell, M. Chamberlain, L. Justham, and M. Jackson, "Geometric

- Optimisation of Electroadhesive Actuators Based on 3D Electrostatic Simulation and its Experimental Verification,” *IFAC-PapersOnLine*, vol. 49, no. 21, pp. 309–315, 2016, doi: 10.1016/j.ifacol.2016.10.574.
- [32] N. Berdozzi *et al.*, “Rapid Fabrication of Electro-Adhesive Devices with Inkjet Printed Electrodes,” *IEEE Robot. Autom. Lett.*, vol. 5, no. 2, pp. 2770–2776, 2020, doi: 10.1109/LRA.2020.2972838.
- [33] N. Berdozzi *et al.*, “Inkjet printed thin-film electro-adhesive device: manufacturing and characterization,” p. 64, 2020, doi: 10.1117/12.2558761.
- [34] M. Caselli *et al.*, “Experimental characterization of a multilayer silicone-based electroactive patch for gripper applications,” p. 61, 2021, doi: 10.1117/12.2582950.
- [35] J. Shintake, V. Cacucciolo, D. Floreano, and H. Shea, “Soft Robotic Grippers,” *Adv. Mater.*, vol. 30, no. 29, 2018, doi: 10.1002/adma.201707035.
- [36] D. Ruffatto, J. Shah, and M. Spenko, “Increasing the adhesion force of electrostatic adhesives using optimized electrode geometry and a novel manufacturing process,” *J. Electrostat.*, vol. 72, no. 2, pp. 147–155, 2014, doi: 10.1016/j.elstat.2014.01.001.
- [37] L. Savioli, G. Sguotti, A. Francesconi, F. Branz, J. Krahn, and C. Menon, “Morphing electroadhesive interface to manipulate uncooperative objects,” *Sensors Smart Struct. Technol. Civil, Mech. Aerosp. Syst. 2014*, vol. 9061, p. 906129, 2014, doi: 10.1117/12.2045065.
- [38] J. P. Díaz Téllez, J. Krahn, and C. Menon, “Characterization of electro-adhesives for robotic applications,” *2011 IEEE Int. Conf. Robot. Biomimetics, ROBIO 2011*, pp. 1867–1872, 2011, doi: 10.1109/ROBIO.2011.6181562.
- [39] M. Ritter and D. Barnhart, “Geometry characterization of electroadhesion samples for spacecraft docking application,” *IEEE Aerosp. Conf. Proc.*, pp. 1–8, 2017, doi: 10.1109/AERO.2017.7943683.
- [40] M. Dadkhah, D. Ruffatto, Z. Zhao, and M. Spenko, “Increasing adhesion via a new electrode design and improved manufacturing in electrostatic/microstructured adhesives,” *J. Electrostat.*, vol. 91, no. March 2017, pp. 48–55, 2018, doi: 10.1016/j.elstat.2017.12.005.
- [41] J. M. Krahn, A. G. Pattantyus-Abraham, and C. Menon, “Polymeric electro-dry-adhesives for use on conducting surfaces,” *Proc. Inst. Mech. Eng. Part L J. Mater. Des. Appl.*, vol. 228, no. 2, pp. 109–114, 2014, doi: 10.1177/1464420713509376.
- [42] Z. Zhang, J. A. Chestney, and M. Sarhadi, “Characterizing an electrostatic gripping device for the automated handling of non-rigid materials,” *Proc. Inst. Mech. Eng. Part B J. Eng. Manuf.*, vol. 215, no. 1, pp. 21–34, 2001, doi: 10.1243/0954405011515109.
- [43] J. Guo, C. Xiang, and J. Rossiter, “A soft and shape-adaptive electroadhesive composite gripper with proprioceptive and exteroceptive capabilities,” *Mater. Des.*, vol. 156, pp. 586–587, 2018, doi: 10.1016/j.matdes.2018.07.027.
- [44] G. J. Monkman, “Compliant robotic devices, and electroadhesion,” *Robotica*, vol. 10, no. 2, pp. 183–185, 1992, doi: 10.1017/S0263574700007608.
- [45] “Grabit Inc.” <https://grabitinc.com/%0A>.
- [46] J. Mici, J. W. Ko, J. West, J. Jaquith, and H. Lipson, “Parallel electrostatic grippers for layered assembly,” *Addit. Manuf.*, vol. 27, no. January, pp. 451–460, 2019, doi: 10.1016/j.addma.2019.03.032.
- [47] M. Dadkhah, Z. Zhao, N. Wettels, and M. Spenko, “A self-aligning gripper using an electrostatic/gecko-like adhesive,” *IEEE Int. Conf. Intell. Robot. Syst.*, vol. 2016-Novem, pp.

- 1006–1011, 2016, doi: 10.1109/IROS.2016.7759172.
- [48] C. Brecher, “Handling of preforms and prepregs for mass production of composites.”
- [49] E. W. Schaler, D. Ruffatto, P. Glick, V. White, and A. Parness, “An electrostatic gripper for flexible objects,” *IEEE Int. Conf. Intell. Robot. Syst.*, vol. 2017-Septe, pp. 1172–1179, 2017, doi: 10.1109/IROS.2017.8202289.
- [50] M. Ayyildiz, M. Scaraggi, O. Sirin, C. Basdogan, and B. N. J. Persson, “Contact mechanics between the human finger and a touchscreen under electroadhesion,” *Proc. Natl. Acad. Sci. U. S. A.*, vol. 115, no. 50, pp. 12668–12673, 2018, doi: 10.1073/pnas.1811750115.
- [51] J. Mullenbach, M. Peshkin, and J. Edward Colgate, “EShiver: Lateral Force Feedback on Fingertips through Oscillatory Motion of an Electroadhesive Surface,” *IEEE Trans. Haptics*, vol. 10, no. 3, pp. 358–370, 2017, doi: 10.1109/TOH.2016.2630057.
- [52] A. Yamamoto, S. Nagasawa, H. Yamamoto, and T. Higuchi, “Electrostatic tactile display with thin film slider and its application to tactile telepresentation systems,” *IEEE Trans. Vis. Comput. Graph.*, vol. 12, no. 2, pp. 168–177, 2006, doi: 10.1109/TVCG.2006.28.
- [53] K. Zhang and S. Follmer, “Electrostatic adhesive brakes for high spatial resolution refreshable 2.5D tactile shape displays,” *IEEE Haptics Symp. HAPTICS*, vol. 2018-March, pp. 319–326, 2018, doi: 10.1109/HAPTICS.2018.8357195.
- [54] H. Wang, A. Yamamoto, and T. Higuchi, “A crawler climbing robot integrating electroadhesion and electrostatic actuation,” *Int. J. Adv. Robot. Syst.*, vol. 11, pp. 1–11, 2014, doi: 10.5772/59118.
- [55] T. N. and T. H. A. Yamamoto, “Wall Climbing Mechanisms Using Electrostatic Attraction Generated by Flexible Electrodes,” *Int. Symp. Micro-NanoMechatronics Hum. Sci.*, pp. 389–394, 2007, doi: 10.1109/MHS.2007.4420886.
- [56] J. Cao *et al.*, “Untethered soft robot capable of stable locomotion using soft electrostatic actuators,” *Extrem. Mech. Lett.*, vol. 21, pp. 9–16, 2018, doi: 10.1016/j.eml.2018.02.004.
- [57] B. C. Leung, N. R. Goeser, L. A. Miller, and S. Gonzalez, “Validation of electroadhesion as a docking method for spacecraft and satellite servicing,” *IEEE Aerosp. Conf. Proc.*, vol. 2015-June, 2015, doi: 10.1109/AERO.2015.7119283.
- [58] W. Saravia and B. Udrea, “Highly compliant active clinging mechanism,” *IEEE Aerosp. Conf. Proc.*, vol. 2016-June, 2016, doi: 10.1109/AERO.2016.7500742.
- [59] H. Jiang *et al.*, “A robotic device using gecko-inspired adhesives can grasp and manipulate large objects in microgravity,” *Sci. Robot.*, vol. 2, no. 7, pp. 1–12, 2017, doi: 10.1126/scirobotics.aan4545.
- [60] T. Pereira, J. V. Kennedy, and J. Potgieter, “A comparison of traditional manufacturing vs additive manufacturing, the best method for the job,” *Procedia Manuf.*, vol. 30, pp. 11–18, 2019, doi: 10.1016/j.promfg.2019.02.003.
- [61] Hue P. Le, “Progress and Trends in Ink-jet Printing Technology,” *J. Imaging Sci. Technol.*, vol. 42, no. 1, pp. 49–62, 1998.
- [62] D. Wallace, “Ink-jet as a MEMS manufacturing tool,” *Int. Conf. Integr. Commer. Micro Nanosyst.*, vol. 42657, pp. 1–8, 2007.
- [63] G. K. Lau and M. Shrestha, “Ink-jet printing of micro-electro-mechanical systems (MEMS),” *Micromachines*, vol. 8, no. 6, 2017, doi: 10.3390/mi8060194.
- [64] A. S. A. Shama, “Study of Microfluidic Mixing and Droplet Generation for 3D Printing of Nuclear Fuels,” 2017.



- 
- [65] J. Li, F. Rossignol, and J. Macdonald, "Inkjet printing for biosensor fabrication: Combining chemistry and technology for advanced manufacturing," *Lab Chip*, vol. 15, no. 12, pp. 2538–2558, 2015, doi: 10.1039/c5lc00235d.
- [66] F. C. Krebs, "Fabrication and processing of polymer solar cells: A review of printing and coating techniques," *Sol. Energy Mater. Sol. Cells*, vol. 93, no. 4, pp. 394–412, 2009, doi: 10.1016/j.solmat.2008.10.004.
- [67] S. Schlatter, S. Rosset, and H. Shea, "Inkjet printing of carbon black electrodes for dielectric elastomer actuators," *Electroact. Polym. Actuators Devices 2017*, vol. 10163, p. 1016311, 2017, doi: 10.1117/12.2258615.
- [68] F. Zhang *et al.*, "Inkjet printing of polyimide insulators for the 3D printing of dielectric materials for microelectronic applications," *J. Appl. Polym. Sci.*, vol. 133, no. 18, pp. 1–11, 2016, doi: 10.1002/app.43361.
- [69] L. J. Matienzo *et al.*, "Surface plasma treatment of polyimide film for cu metallization," *J. Adhes. Sci. Technol.*, vol. 14, no. 1, pp. 3384–3388, 2005, doi: 10.1163/156856196X00490.
- [70] S. Bhattacharya, A. Datta, J. M. Berg, and S. Gangopadhyay, "Studies on surface wettability of poly(dimethyl) siloxane (PDMS) and glass under oxygen-plasma treatment and correlation with bond strength," *J. Microelectromechanical Syst.*, vol. 14, no. 3, pp. 590–597, 2005, doi: 10.1109/JMEMS.2005.844746.
- [71] Y. Moriguchi *et al.*, "Impact of non-thermal plasma surface modification on porous calcium hydroxyapatite ceramics for bone regeneration," *PLoS One*, vol. 13, no. 3, pp. 1–18, 2018, doi: 10.1371/journal.pone.0194303.
- [72] A. D. Katnani, A. Knoll, and M. A. Mycek, "Effects of environment and heat treatment on an oxygen plasma-treated polyimide surface and its adhesion to a chromium overcoat," *J. Adhes. Sci. Technol.*, vol. 3, no. 1, pp. 441–453, 1989, doi: 10.1163/156856189X00326.
- [73] N. Inagaki, S. Tasaka, and K. Hibi, "Surface modification of Kapton film by plasma treatments," *J. Polym. Sci. Part A Polym. Chem.*, vol. 30, no. 7, pp. 1425–1431, 1992, doi: 10.1002/pola.1992.080300722.
- [74] G. Giridhar, R. K. N. R. Manepalli, and G. Apparao, *Contact Angle Measurement Techniques for Nanomaterials*, vol. 3. Elsevier Inc., 2017.
- [75] M. A. Quetzeri-Santiago, J. R. Castrejón-Pita, and A. A. Castrejón-Pita, "On the analysis of the contact angle for impacting droplets using a polynomial fitting approach," *Exp. Fluids*, vol. 61, no. 6, pp. 1–13, 2020, doi: 10.1007/s00348-020-02971-1.
- [76] N. Blaž, M. Kisić, Č. Žlebič, A. Marić, and L. Živanov, "Capacitance variation of inkjet printed interdigital capacitor by structure bending," *Proc. Int. Spring Semin. Electron. Technol.*, vol. 2016-Septe, pp. 506–509, 2016, doi: 10.1109/ISSE.2016.7563250.
- [77] M. Gierczak, P. Markowski, Z. Zaluk, A. Dziedzic, and P. Jankowski-Miśkiewicz, "Ink-jet printed conductive films - Geometrical and electrical characterization," *Proc. Int. Spring Semin. Electron. Technol.*, vol. 2016-Septe, pp. 392–397, 2016, doi: 10.1109/ISSE.2016.7563227.
- [78] J. E. Fromm, "Numerical Calculation of the Fluid Dynamics of Drop-on-Demand Jets," *IBM J. Res. Dev.*, vol. 28, no. 3, pp. 322–333, 1984, doi: 10.1147/rd.283.0322.
- [79] K. A. M. Seerden, N. Reis, J. R. G. Evans, P. S. Grant, J. W. Halloran, and B. Derby, "Ink-Jet Printing of Wax-Based Alumina Suspensions," *J. Am. Ceram. Soc.*, vol. 84, no. 11, pp. 2514–2520, 2001, doi: 10.1111/j.1151-2916.2001.tb01045.x.
- [80] E. Kim and J. Baek, "Numerical study on the effects of non-dimensional parameters on drop-

- on-demand droplet formation dynamics and printability range in the up-scaled model,” *Phys. Fluids*, vol. 24, no. 8, 2012, doi: 10.1063/1.4742913.
- [81] D. Jang, D. Kim, and J. Moon, “Influence of fluid physical properties on ink-jet printability,” *Langmuir*, vol. 25, no. 5, pp. 2629–2635, 2009, doi: 10.1021/la900059m.
- [82] B. Derby and N. Reis, “Inkjet Printing of Highly Loaded Particulate Suspensions,” *MRS Bull.*, vol. 28, no. 11, pp. 815–818, 2003, doi: 10.1557/mrs2003.230.
- [83] Y. F. Liu, M. H. Tsai, Y. F. Pai, and W. S. Hwang, “Control of droplet formation by operating waveform for inks with various viscosities in piezoelectric inkjet printing,” *Appl. Phys. A Mater. Sci. Process.*, vol. 111, no. 2, pp. 509–516, 2013, doi: 10.1007/s00339-013-7569-7.
- [84] N. Reis, C. Ainsley, and B. Derby, “Ink-jet delivery of particle suspensions by piezoelectric droplet ejectors,” *J. Appl. Phys.*, vol. 97, no. 9, pp. 8–14, 2005, doi: 10.1063/1.1888026.
- [85] P. W. Effects and P. A. Effects, “MicroFab Technote 99-03 Drive Waveform Effects on Ink-Jet Device Performance,” *Pulse*, pp. 1–4, 1999.
- [86] H. Y. Gan, X. Shan, T. Eriksson, B. K. Lok, and Y. C. Lam, “Reduction of droplet volume by controlling actuating waveforms in inkjet printing for micro-pattern formation,” *J. Micromechanics Microengineering*, vol. 19, no. 5, 2009, doi: 10.1088/0960-1317/19/5/055010.
- [87] A. U. Chen and O. A. Basaran, “A new method for significantly reducing drop radius without reducing nozzle radius in drop-on-demand drop production,” *Phys. Fluids*, vol. 14, no. 1, 2002, doi: 10.1063/1.1427441.
- [88] S. D. Hoath, “A simple model for DoD Inkjet frequency response,” *Int. Conf. Digit. Print. Technol.*, vol. 2015-Janua, no. 1, pp. 8–12, 2015.
- [89] R. Li, N. Ashgriz, and S. Chandra, “Droplet generation from pulsed micro-jets,” *Exp. Therm. Fluid Sci.*, vol. 32, no. 8, pp. 1679–1686, 2008, doi: 10.1016/j.expthermflusci.2008.06.002.
- [90] S. D. Hoath, W. K. Hsiao, S. Jung, G. D. Martin, and I. M. Hutchings, “Dependence of drop speed on nozzle diameter, viscosity and drive amplitude in drop-on-demand ink-jet printing,” *Int. Conf. Digit. Print. Technol.*, pp. 62–65, 2011.
- [91] H. Dong, W. W. Carr, and J. F. Morris, “An experimental study of drop-on-demand drop formation,” *Phys. Fluids*, vol. 18, no. 7, 2006, doi: 10.1063/1.2217929.
- [92] B. A. Kipfer, *Design and Analysis of experiments*. 2021.
- [93] D. Ruffatto, J. Shah, and M. Spenko, “Optimization and experimental validation of electrostatic adhesive geometry,” *IEEE Aerosp. Conf. Proc.*, 2013, doi: 10.1109/AERO.2013.6496943.
- [94] E. M. Liston, “Plasma treatment for improved bonding: A review,” *J. Adhes.*, vol. 30, no. 1–4, pp. 199–218, 1989, doi: 10.1080/00218468908048206.